High-sensitivity Full-field Quantitative Phase Imaging Based on Wavelength Shifting Interferometry

Shichao Chen

Dissertation submitted to the faculty of the Virginia Polytechnic Institute and State University in partial fulfillment of the requirements for the degree of

Doctor of Philosophy
In
Electrical Engineering

Yizheng Zhu, Chair

Anbo Wang

Wei Zhou

Jia-Bin Huang

Kiho Lee

July 31, 2019
Blacksburg, VA

Keywords: wavelength shifting interferometry, quantitative phase imaging, sensitivity analysis

High-sensitivity Full-field Quantitative Phase Imaging Based on Wavelength Shifting Interferometry

Shichao Chen

ABSTRACT

Quantitative phase imaging (QPI) is a category of imaging techniques that can retrieve the phase information of the sample quantitatively. QPI features label-free contrast and non-contact detection. It has thus gained rapidly growing attention in biomedical imaging. Capable of resolving biological specimens at tissue or cell level, QPI has become a powerful tool to reveal the structural, mechanical, physiological and spectroscopic properties. Over the past two decades, QPI has seen a broad spectrum of evolving implementations. However, only a few have seen successful commercialization. The challenges are manifold. A major problem for many QPI techniques is the necessity of a custom-made system which is hard to interface with existing commercial microscopes. For this type of QPI techniques, the cost is high and the integration of different imaging modes requires nontrivial hardware modifications. Another limiting factor is insufficient sensitivity. In QPI, sensitivity characterizes the system repeatability and determines the quantification resolution of the system. With more emerging applications in cell imaging, the requirement for sensitivity also becomes more stringent.

In this work, a category of highly sensitive full-field QPI techniques based on wavelength shifting interferometry (WSI) is proposed. On one hand, the full-field implementations, compared to point-scanning, spectral domain QPI techniques, require no mechanical scanning to form a phase image. On the other, WSI has the advantage of preserving the integrity of the interferometer and compatibility with multi-modal imaging requirement. Therefore, the techniques proposed here have the potential to be readily integrated into the ubiquitous lab microscopes and equip them with quantitative imaging functionality. In WSI, the shifts in wavelength can be applied in fine steps, termed swept source digital holographic phase microscopy (SS-DHPM), or a multi-wavelength-band manner, termed low coherence wavelength shifting interferometry (LC-WSI). SS-DHPM brings in an additional capability to perform spectroscopy, whilst the LC-WSI achieves a faster imaging rate which has been demonstrated with live sperm cell imaging. In an attempt to integrate WSI with the existing commercial microscope, we also discuss the possibility of demodulation for low-cost sources and common path implementation.

Besides experimentally demonstrating the high sensitivity (limited by only shot noise) with the proposed techniques, a novel sensitivity evaluation framework is also introduced for the first time in QPI. This framework examines the Cramér-Rao bound (CRB), algorithmic sensitivity and experimental sensitivity, and facilitates the diagnosis of algorithm efficiency and system efficiency. The framework can be applied not only to the WSI techniques we proposed, but also to a broad range of QPI techniques. Several popular phase shifting interferometry techniques as well as off-axis interferometry is studied. The comparisons between them are shown to provide insights into algorithm optimization and energy efficiency of sensitivity.

High-sensitivity Full-field Quantitative Phase Imaging Based on Wavelength Shifting Interferometry

Shichao Chen

GENERAL AUDIENCE ABSTRACT

The most common imaging systems nowadays capture the image of an object with the irradiance perceived by the camera. Based on the intensity contrast, morphological features, such as edges, humps, and grooves, can be inferred to qualitatively characterize the object. Nevertheless, in scientific measurements and research applications, a quantitative characterization of the object is desired. Quantitative phase imaging (QPI) is such a category of imaging techniques that can retrieve the phase information of the sample by properly design the irradiance capturing scheme and post-process the data, converting them to quantitative metrics such as surface height, material density and so on. The imaging process of QPI will neither harm the sample nor leave exogenous residuals. As a result, it has thus gained rapidly growing attention in biomedical imaging. Over the past two decades, QPI has seen a broad spectrum of evolving implementations, but only a few have seen successful commercialization. The challenges are manifold whilst one stands out - that they have expensive optical setups that are often incompatible with existing commercial microscope platforms. The setups are also very complicated such that without professionals having solid optics background, it is difficult to operate the system to perform imaging applications. Another limiting factor is the insufficient understanding of sensitivity. In QPI, sensitivity characterizes the system repeatability and determines its quantification resolution. With more emerging applications in cell imaging, the requirement for sensitivity also becomes more stringent.

In this work, a category of highly sensitive full-field QPI techniques based on wavelength shifting interferometry (WSI) is proposed. WSI images the full-field of the sample simultaneously, unlike some other techniques requiring scanning one probe point across the sample. It also has the advantage of preserving the integrity of the interferometer, which is the key structure to enable highly sensitive measurement for QPI methods. Therefore, the techniques proposed here have the potential to be readily integrated into the ubiquitous lab microscopes and equip them with quantitative imaging functionality. Differed by implementations, two WSI techniques have been proposed, termed swept source digital holographic phase microscopy (SS-DHPM), and low coherence wavelength shifting interferometry (LC-WSI), respectively. SS-DHPM brings in an additional capability to perform spectroscopy, whilst the LC-WSI achieves a faster imaging rate which has been demonstrated with live sperm cell imaging. In an attempt to integrate WSI with the existing commercial microscope, we also discuss the possibility of demodulation for low-cost sources and common path implementation.

Besides experimentally demonstrating the high sensitivity with the proposed techniques, a novel sensitivity evaluation framework is also introduced for the first time in QPI. This framework not only examines the realistic sensitivity obtained in experiments, but also compares it to the theoretical values. The framework can be widely applied to a broad range of QPI techniques, providing insights into algorithm optimization and energy efficiency of sensitivity.

Acknowledgement

Quantitative phase imaging was a brand new area when I started my doctorate at Virginia Tech. It has been a long journey and I have seen myself learning and evolving by putting in a lot of hard work and thoughts. I would like to thank all who share with me this journey, contribute their efforts, and make it a joyful one.

I would express my sincere gratitude to my advisor, Dr. Yizheng Zhu, for introducing me to this area and being my mentor all along. Your passion and pursuit for perfection cultivate my high standards for experiments and make me confident about the data I acquired and the conclusions I draw. You are the one who teaches me to always look at the bright side while maintaining critical thinking so that I can keep improving. I am grateful to be one of your earliest students because starting from scratch makes it a hard-earned but very rewarding life lesson. It also means more exposure to diverse and unknown areas. All those work not documented in this dissertation, including non-uniform FFT, phase unwrapping, line-scan holography, cell electroporation, and the textile defect detection project we have spent more than a year on, truly benefit my project planning and implementation abilities. It was an honor to work with you for the past six productive years, and I hope our collaboration in research can be continued.

I want to say thank you to all my committee members, Dr. Anbo Wang, Dr. Wei Zhou, Dr. Jiabin Huang, and Dr. Kiho Lee. Your insightful comments and suggestions give me a deeper understanding of the work I have been doing as well as inspirations for new research directions more than you can imagine. I greatly enjoy the discussions with you and learn from your expertise. I want to thank Dr. Ting-Chung Poon and Dr. Cheng Ma for providing me guidance and revising the manuscript word by word when I conducted sensitivity studies in digital holography. I also want to say thank you to Dr. Ahmad Safaai-Jazi for his constructional comments when I explore laser speckle imaging in the course project. Thanks also go to Dr. Yuhao Zhang for his suggestions in phase plate fabrication and Dr. Donald Leber for his facility support in the MicrON lab.

I highly appreciate those who have helped me in my career planning, including Dr. Jaime De La Ree, Dr. Kent Murphy, Dr. Rona Zhou, Dr. Florian Fournier, Dr. Jannick P. Rolland, Dr. William J. Cassarly, Dr. Groot Gregory, Jeff Faust, Larry Brown, Gary McComas, Larry Nickell, Dr. Yibo Zhang, and Dr. Justin Lee etc. Your encouragement and generous help make me better prepared for my upcoming career path.

I also want to say thanks to all my wonderful lab members and colleagues I've been working with: Dr. Chengshuai Li, Jacob Black, Joseph Thomas, Shuo Yang, Jiaji He, Ziang Feng, Guannan Shi, Zhixing He, Ruibo Shang, Dr. Bo Dong, Dr. Bo Liu, Dr. Lingmei Ma, Dr. Di Hu, Dr. Chennan Hu, Dr. Li Yu, Dr. Guigui Wan, Dr. Yuanyuan Guo, Dr. Junghyun Ryu, Dr. Daniel Sweeney, Ruohan Zhou, Justin Desai, Shubham Dawda, Sizhe Guo, Dr. Fang Liu, Dr. Xiaona Li, Dr. Zhihao Yu, Yunwei Ma, Yunzhi Wang, etc. It is my pleasure to work with you and learn from your professionalism and your passion for research.

Last but not least, I want to say thank you to my dear parents, my sister, and my fiancee. I'll not be here without your unconditional support.

Table of Contents

List of Figures

List of Tables

Chapter 1 Introduction

1.1 Quantitative Phase Imaging and Its Applications

Quantitative phase imaging (QPI) has received tremendous attention over the past two decades. Unlike traditional imaging approaches such as Zernike phase contrast [1] and Nomarski differential interference contrast [2], QPI, as its name implies, is capable of quantifying the intrinsic phase distribution of a sample under investigation. Generally, in QPI systems, the illumination fields from the sources will interact with the sample due to absorption and scattering. The interaction will not only induce attenuation in the field magnitude but also a phase delay which contains the subtle structural information of the sample. This information can be retrieved from the intensity signals received by the detectors through dedicated algorithms and further converted to optical pathlength (OPL) information.

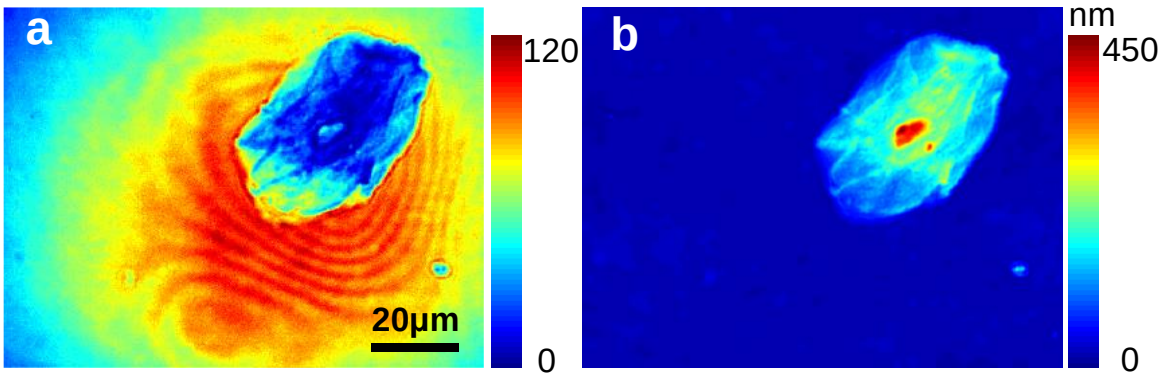

Fig. 1-1 Bright field vs. QPI on a human cheek cell sample. (a) The nucleus in the bright field intensity image exhibits low contrast to the cytoplasm. (b) QPI image shows clear intracellular structures with much higher contrast for the nucleus.

Imaging requires contrast to reveal information. Bright-field imaging, which relies on intensity contrast, normally encounters challenges with many biological specimens and other similar transparent objects, because they do not exhibit significant light absorption or scattering, especially in the visible spectral region [3]. To enhance the imaging contrast, chemical and fluorescent dyes are commonly used to label the cells [4,5]. However, these exogenous agents usually cause several consequences. Firstly, they may be toxic and cause damage to the specimen. Secondly, it is time-consuming to perform the staining procedure before each experiment, and the fluorophores can lose their ability to fluoresce due to photo-bleaching. And lastly, the data depend on staining strength or color correction, which may cause the images cannot be compared quantitatively across

instruments and laboratory locations. As a result, they are generally not suitable for quantitative analysis. On the contrary, QPI relies on label-free optical phase contrast and is therefore free from these consequences. Although currently difficult to provide the level of chemical specificity as fluorescent microscopy does, QPI can offer complementary information regarding the morphological, optical, and mechanical properties of a sample.

Sensitivity is a critical index to demonstrate the stability of a system and the resolution of its measurements. In QPI, sensitivity is often calculated as the temporal standard deviation of OPL. Nowadays, with the advances in highly stable light sources, detectors as well as phase shifting devices, interferometric based QPI techniques can reach deep sub-nanometer level sensitivity values [6-9].

The capabilities of quantitative measurement, label-free operation, and nanoscale sensitivity make QPI popular in bio-imaging, especially on the microscopic scale. It is capable of revealing structural [7, 10-13], mechanical [14-16], refractive [17-20], physiological [21] and spectroscopic [22,23] properties of living cells and tissues. It can also be used in live cell particle tracking [24] and cell electro-motility studies [25]. Although QPI is competent in imaging different types of cells and tissues, red blood cells (RBCs) are undoubtedly special targets that have been heavily studied. RBC is an ideal phase object because it lacks nuclei and other internal structures. As a result, the phase change directly reflects the cell thickness and the refractive index distribution, which is affected by the hemoglobin concentration. By scanning the sample or the beam in depth direction, topography is achieved with the 3D phase distribution. Morphological properties such as cell volume and surface area can be readily obtained with nanometer accuracy in terms of OPL. By studying these parameters, abnormalities in RBC morphology can be determined. Such cellular level diagnosis provides an early-stage warning for a number of pathologies [26]. Macrocytic anemia, spherocytosis (spherical cells) can indicate hemolytic anemia, and anisocytosis (unequal size distribution) can indicate thalassemia major (Fig. 1-2) [27]. There are other diseases that would cause cell morphology changes, such as sickle cell anemia and malaria. QPI not only suits the demanding requirements of biological imaging but also can be used extensively in other investigation areas. These areas include semiconductor etching process monitoring, digital projection photochemical etching, and semiconductor wafer defect detection [28].

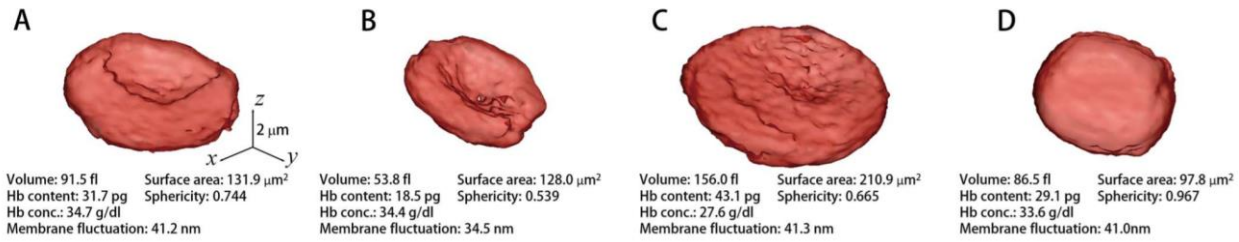

Fig. 1-2 QPI used in blood testing. Refractive index as a function of spatial coordinates can be obtained and differentiate RBCs taken from (a) healthy patients, those with (b) iron deficiency anemia (IDA) (c) reticulocytosis and (d) hereditary spherocytosis (HS) [27]. Reprinted by permission from Springer Nature.

A wide variety of novel QPI techniques have been proposed driven by the applications. Classifications of these techniques are usually based upon their optical geometries. Yet there exist diverse standards to differentiate one technique from another, and conversion from one class to the other can be performed with slight modification. Three common classification approaches are listed:

- Scanning vs. full-field based techniques.

  In scanning based implementations, a single phase image is acquired by raster 2D scan of a single spot or 1D scan of a focusing line [7, 29-33]. The image is stitched by the results of point detection device (i.e. photodiode) or line detection device (i.e. line-scan camera). The benefit of this implementation is flexible scanning range (field of view) and step (resolution). In full-field based implementations, pixels in the field of view are synchronized and the image is acquired by a 2D detection device, such as CCD and CMOS camera. Compared to scanning based implementations, full-field QPI can be made low-cost, simple in setup and alignment, potential in faster speed, and easy access to a commercial benchtop microscope.
- Interferometric vs. non-interferometric.

  When referring to QPI, we typically assume interferometric setups since their high phase stabilities have been well established. However, there is also an emerging branch of non-interferometric QPI techniques, such as those based on transport-of-intensity equation (TIE) [34], Fourier ptychography [35,36], etc.
- Transmission mode vs. reflection mode.

The transmission mode is more preferable in bio-imaging applications since a large portion of the energy is passed through the sample and efficiently collected, and the front scattering light is much stronger than the backward scattering portion. Hence the illumination power can be lowered to avoid damaging the specimen. Meanwhile, for image-plane interferometric based QPI, the specimen requires no special preparation to ensure the sample is close to the strong reflection reference surface, making it convenient for live cell imaging. On the other hand, reflection mode (epi-configuration, illumination and detection on the same side) is mostly used in surface topography and it requires samples with strong reflections.

With system modifications, QPI techniques can also be converted to retrieve 3D tomography information. Examples can be found for white-light diffraction tomography [37] and tomographic phase microscopy (TPM) [38]. They are both 3D versions of spatial light interference microscopy (SLIM) [6], although the former adopts z-axis scanning the focal plane whilst the latter tilts the angle of illumination and generate projections in analogy to computed tomography (CT) which uses X-rays. Differed from CT, light waves used in TPM is noninvasive and the contrast is encoded in the variations of refractive index. Similar conversion from 2D to 3D can also be seen in common-path diffraction optical tomography [12], which evolves as a 3D version of the diffraction phase microscopy [11] with a set of different angles to obtain tomographic information, and in digital holographic based tomography [19], which fixes the illumination but rotates the sample in a 2D off-axis digital holography setup.

1.2 Challenges & Motivation

Despite widespread applications and a diverse spectrum of capabilities, not a lot of QPI techniques have seen successful commercialization [6,39,40]. The challenges are manifold. Firstly, most techniques require custom-made systems, some of which are built with geometries hard to access existing commercial microscopes – a universal platform where multi-modal imaging has been successfully demonstrated. After all, phase contrast is only one of the several modalities of imaging contrasts. Other imaging modes based on intensity, DIC, birefringence, and fluorescence, when combined with phase, can provide a more comprehensive investigation of the specimen: DIC can provide optical sectioning capability and is useful in tomography; birefringence can reveal anisotropic optical properties; fluorescence can still be significant where specific labeling is a must.

Secondly, the challenge exhibits in achieving high sensitivity so that signals will not be buried under the phase noise. Finally, there are other factors such as cost, resolution, acquisition rate, and system size. They are fairly common in a broad range of phasor measurement system [41,42] and will all affect successful commercialization of QPI techniques.

In an effort to overcome these challenges, this work is aimed at proposing a category of QPI techniques that have the potential to be compatible with existing microscopes, convenient for multi-mode imaging, and also can provide highly sensitive quantitative phase measurements. The optical geometries, whose categorizations have been shown in the previous section, can be very sensitive to system capabilities. For example, the scanning based QPI will find it sophisticated to introduce the scanning parts (i.e. a galvanometer) in the optical path of the microscope and to synchronize both illumination and imaging; the interferometric based QPI can retrieve phase with high sensitivity; reflection mode will have limited applications in bio-imaging applications. Therefore, preference and focus of this work will be towards full-field QPI and interferometric configurations with transmission mode imaging. Finally, and somewhat baffling, although the sensitivity limit has been empirically pushed towards the sub-nanometer level, no evaluation framework has yet been proposed for sensitivity itself. Experimental results across different QPI techniques and different laboratories cannot be compared in a fair manner because of different hardware settings, and cannot even be compared to their own theoretical bounds since no practical approximations can link the experiment with theory. These problems will be addressed with an in-depth discussion of the sensitivity evaluation in this work.

1.3 Research Overview

In Chapter 2, full-field QPI techniques are reviewed and their principles are introduced as background information. In Chapter 3, two swept source based wavelength shifting interferometry techniques have been proposed, with one features high coherence illumination and dense spectral sampling and the other utilizes low coherence illumination with multi-shot acquisitions. LEDs with unevenly spaced wavelengths and irregular spectral shape can replace the laser sources and bring down the cost. In order to access commercial microscopes, a common path implementation with WSI is also discussed. Chapter 4 mainly discusses the sensitivity and its evaluation framework, which is significant in QPI technique developments, selections, and optimizations. A brief summary is given at the end.

References

[1] F. Zernike, "Phase contrast, a new method for the microscopic observation of transparent objects part II." Physica **9**, 974–986 (1942).

[2] G. Nomarski, “Differential microinterferometer with polarized waves”, Journal de Physique et Le Radium **16**, 9S–11S (1955).

[3] G. Popescu, Quantitative Phase Imaging of Cells and Tissues (McGraw-Hill, 2011).

[4] J. S. Ploem, “The use of a vertical illuminator with interchangeable dichroic mirrors for fluorescence microscopy with incident light,” Zeitschrift Fur Wissenschaftliche Mikroskopie Und Fur Mikroskopische Technik, **68**, 129-142 (1967).

[5] D. L. Taylor, and Y. L. Wang, Fluorescence Microscopy of Living Cells in Culture, Part B: Quantitative Fluorescence Microscopy-Imaging and Spectroscopy (Vol. 30) (Academic Press, 1989).

[6] Z. Wang, L. Millet, M. Mir, H. Ding, S. Unarunotai, J. Rogers, M. U. Gillette, and G. Popescu, "Spatial light interference microscopy (SLIM)," Optics Express **19**, 1016-1026 (2011).

[7] R. Shang, S. Chen, C. Li, and Y. Zhu, "Spectral modulation interferometry for quantitative phase imaging," Biomedical Optics Express **6**, 473-479 (2015).

[8] T. Slabý, P. Kolman, Z. Dostál, M. Antoš, M. Lošťák, and R. Chmelík, "Off-axis setup taking full advantage of incoherent illumination in coherence-controlled holographic microscope," Optics Express **21**, 14747-14762 (2013).

[9] A. S.G. Singh, A. Anand, R. A. Leitgeb, and B. Javidi, "Lateral shearing digital holographic imaging of small biological specimens," Optics Express **20**, 23617-23622 (2012).

[10] N. T. Shaked, M. T. Rinehart, and A. Wax. "Dual-interference-channel quantitative-phase microscopy of live cell dynamics," Optics Letters **34**, 767-769 (2009).

[11] G. Popescu, T. Ikeda, R. R. Dasari, and M. S. Feld, “Diffraction phase microscopy for quantifying cell structure and dynamics,” Optics Letters, **31**, 775-777 (2006).

[12] Y. Kim, H. Shim, K. Kim, H. Park, J. H. Heo, J. Yoon, and Y. Park, "Common-path diffraction optical tomography for investigation of three-dimensional structures and dynamics of biological cells," Optics Express, **22**, 10398-10407 (2014).

[13] M. A. Choma, A. K. Ellerbee, C. Yang, T. L. Creazzo, and J. A. Izatt, J. A, "Spectral-domain phase microscopy," Optics Letters, **30**, 1162-1164 (2005).

[14] Y. Park, C. A. Best, K. Badizadegan, R. R. Dasari, M. S. Feld, T. Kuriabova, and G. Popescu, "Measurement of red blood cell mechanics during morphological changes," Proceedings of the National Academy of Sciences, **107**, 6731-6736 (2010).

[15] W. J. Eldridge, A. Sheinfeld, M. T. Rinehart, and A. Wax, "Imaging deformation of adherent cells due to shear stress using quantitative phase imaging" Optics letters, **41**, 352-355 (2016).

[16] G. Popescu, T. Ikeda, K. Goda, C. A. Best-Popescu, M. Laposata, S. Manley, and M. S. Feld, "Optical measurement of cell membrane tension," Physical Review Letters, **97**, 218101 (2006).

[17] N. Lue, G. Popescu, T. Ikeda, R. R. Dasari, K. Badizadegan, and M. S. Feld, "Live cell refractometry using microfluidic devices," Optics Letters, **31**, 2759-2761(2006).

[18] N. Lue, J. Bewersdorf, M. D. Lessard, K. Badizadegan, R. R. Dasari, M. S. Feld, and G. Popescu, "Tissue refractometry using Hilbert phase microscopy," Optics Letters, **32**, 3522-3524 (2007).

[19] F. Charrière, A. Marian, F. Montfort, J. Kuehn, T. Colomb, E. Cuche, and C. Depeursinge, "Cell refractive index tomography by digital holographic microscopy," Optics letters, **31**, 178-180 (2006).

[20] Y. Park, M. Diez-Silva, G. Popescu, G. Lykotrafitis, W. Choi, M. S. Feld, and S. Suresh, "Refractive index maps and membrane dynamics of human red blood cells parasitized by Plasmodium falciparum," Proceedings of the National Academy of Sciences, **105**, 13730-13735 (2008).

[21] K. Lee, K. Kim, J. Jung, J. Heo, S. Cho, S. Lee, and Y. Park, "Quantitative phase imaging techniques for the study of cell pathophysiology: from principles to applications," Sensors, **13**, 4170-4191(2013).

[22] M. Rinehart, Y. Zhu, and A. Wax, "Quantitative phase spectroscopy," Biomedical Optics Express, **3**, 958-965 (2012).

[23] Y. Jang, J. Jang, and Y. Park, "Dynamic spectroscopic phase microscopy for quantifying hemoglobin concentration and dynamic membrane fluctuation in red blood cells," Optics Express, **20**, 9673-9681 (2012).

[24] Y. Park, G. Popescu, K. Badizadegan, R. R. Dasari, R. R and M. S. Feld, "Fresnel particle tracing in three dimensions using diffraction phase microscopy," Optics Letters, **32**, 811-813 (2007).

[25] C. Fang-Yen, S. Oh, Y. Park, W. Choi, S. Song, H. S. Seung, and M. S. Feld, "Imaging voltage-dependent cell motions with heterodyne Mach-Zehnder phase microscopy," Optics Letters, **32**, 1572-1574 (2007).

[26] H. Majeed, S. Sridharan, M. Mir, L. Ma, E. Min, W. Jung, and G. Popescu, "Quantitative phase imaging for medical diagnosis" Journal of Biophotonics, **10**, 177-205 (2017).

[27] Y. Kim, H. Shim, K. Kim, H. Park, S. Jang, and Y. Park, "Profiling individual human red blood cells using common-path diffraction optical tomography," Scientific Reports, **4**, 6659 (2014).

[28] B. Bhaduri, C. Edwards, H. Pham, R. Zhou, T. H. Nguyen, L. L. Goddard, and G. Popescu, "Diffraction phase microscopy: principles and applications in materials and life sciences," Advances in Optics and Photonics, **6**, 57-119 (2014).

[29] Y. Zhu, N. T. Shaked, L. L. Satterwhite, and A. Wax, "Spectral-domain differential interference contrast microscopy," Optics letters, **36**, 430-432 (2011).

[30] T. C. Poon, *Optical Scanning Holography with MATLAB*® (Springer Science & Business Media, 2007).

[31] S. Kimura, and T. Wilson, "Confocal scanning optical microscope using single-mode fiber for signal detection," Applied optics **30**, 2143-2150 (1991).

[32] C. Li, and Y. Zhu, “Quantitative polarized light microscopy using spectral multiplexing interferometry,” Optics letters, **40**, 2622-2625 (2015).

[33] C. Li, S. Chen, M. Klemba, and Y. Zhu, “Integrated quantitative phase and birefringence microscopy for imaging malaria-infected red blood cells,” Journal of Biomedical Optics, **21**, 090501-090501(2016).

[34] C. Zuo, Q. Chen, W. Qu, and A. Asundi, “High-speed transport-of-intensity phase microscopy with an electrically tunable lens,” Optics express, **21**, 24060-24075 (2013).

[35] G. Zheng, R. Horstmeyer, and C. Yang, “Wide-field, high-resolution Fourier ptychographic microscopy,” Nature photonics, **7**, 739-745 (2013).

[36] L. Tian and L. Waller, "3D intensity and phase imaging from light field measurements in an LED array microscope," Optica **2**, 104-111 (2015).

[37] T. Kim, R. Zhou, M. Mir, S. D. Babacan, P. S. Carney, L. L. Goddard, and G. Popescu, “White-light diffraction tomography of unlabelled live cells,” Nature Photonics, **8**, 256-263 (2014).

[38] W. Choi, C. Fang-Yen, K. Badizadegan, S. Oh, N. Lue, R. R. Dasari, and M. S. Feld, “Tomographic phase microscopy,” Nature Methods, **4**, 717-719 (2007).

[39] K. Lee, and Y. Park, “Quantitative phase imaging unit,” Optics Letters, **39**, 3630-3633 (2014).

[40] P. Bon, G. Maucort, B. Wattellier, and S. Monneret, “Quadriwave lateral shearing interferometry for quantitative phase microscopy of living cells,” Optics Express, **17**, 13080-13094 (2009).

[41] J. De La Ree, V. Centeno, J. S. Thorp, and A. G. Phadke, "Synchronized phasor measurement applications in power systems," IEEE Transactions on smart grid **1**, 20-27 (2010).

[42] X. Li, C. Mishra, and J. De La Ree, "Frequency Control of Decoupled Synchronous Machine Using Koopman Operator Based Model Predictive," Proceedings of the 2019 IEEE PES General Meeting (2019).

Chapter 2 Background: Full-field Quantitative Phase Imaging

This chapter will review the cutting-edge full-field QPI techniques as a background for wavelength shifting interferometry (WSI). In full-field interferometry based QPI, the optical system requires no mechanical scanning to form a single phase image, which results in better synchronization of pixels, lower mechanical errors, and most importantly, less difficulty to integrate with a commercialized microscope. Besides, high-performance two-dimensional signal acquisition devices (i.e. CCD or CMOS cameras) have become much cheaper and reliable nowadays.

There are two main classes of interferometric geometries, namely off-axis interferometry and on-axis interferometry, for full-field QPIs. The off-axis geometry, where the sample and reference beams are at an angle to generate a spatial carrier frequency, offer fast, single-shot imaging, at the expense of spatial imaging bandwidth of the system and possibly resolution as well. The on-axis geometry operates at baseband and utilize camera bandwidth efficiently but usually require phase shifting schemes for multiple acquisitions, thus increasing system complexity and reducing imaging speed. Next, the representative techniques of both classes will be introduced.

2.1 Off-axis: Holography, Diffraction Phase & Quadriwave Lateral Shearing

In the off-axis geometries, the sample beam is interfered with a tilted reference beam to generate interferogram and phase is then recovered by signal processing algorithms. Here several specific techniques are selected to be discussed, including digital holographic based techniques, diffraction phase microscopy, and quadriwave lateral shearing techniques.

2.1.1 Digital Holography

The historical origin of holography begins with Rayleigh's creation of a Fresnel lens and the generation of an interference pattern by the superposition of a spherical wave with a planar wave. Gabor realized the same process (superposition of a reference wave) can be used to optically record and reconstruct the amplitude and phase of an object wave. An in-line (on-axis) configuration was proposed when he named the technique "holography" [1]. However, off-axis configuration soon became predominant due to its intrinsic spatial separation of the "twin image", which is caused by the undiffracted part of the reconstruction wave [2]. In the early days, numerical recording of the hologram can only be achieved with photographic plate [3]. The term "digital holography" was

not recognized by the optical metrology community until the direct recording of Fourier hologram in the 1990s by Schnars and Jüptner [4], mostly thanks to tremendous developments in charged couple device (CCD) industry. The dramatic growing computation power, on the other hand, also permits hologram reconstruction to be more efficient.

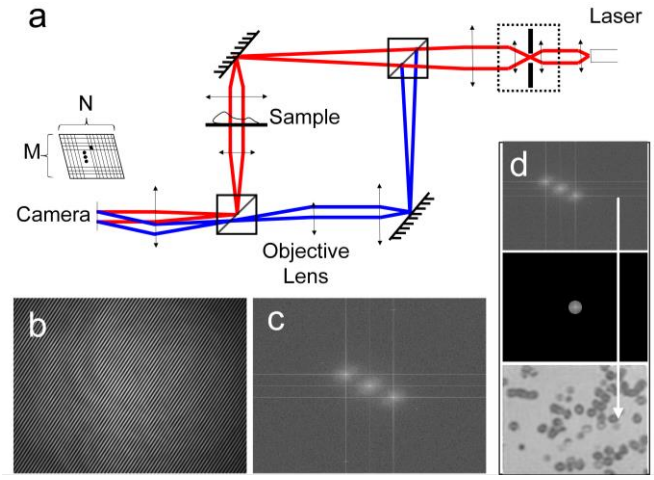

Fig. 2-1 Off-axis DH configuration and the Fourier-transform based signal processing algorithm.

Cuche et al. proposed digital holographic phase microscopy (DHPM) in 1999 as a milestone improvement of the technique and its corresponding reconstruction algorithm [5,6]. With the technique, amplitude and phase-contrast of the specimen can be simultaneously retrieved from a single hologram. In a digital holography setup shown in Fig. 2-1, the collimated light coming out the laser, which is highly coherent, is expanded and then transmitted through a basic Mach-Zehnder interferometer. After the last beam-splitter, the object wave and the reference wave are combined to generate a hologram, whose intensity is expressed as:

$$I_H(x,y) = |\mathbf{O}|^2 + |\mathbf{R}|^2 + \mathbf{R}^*\mathbf{O} + \mathbf{O}^*\mathbf{R}\,. \tag{2-1}$$

This intensity is recorded by the CCD camera. During reconstruction, a simulated digital reference wave, $\mathbf{R}_D(x,y)$, is multiplied to the hologram $I_H(x,y)$ and the phase term is retrieved. In image-plane holography, a Fourier Transform based method is often used and will be described later in Chapter 5.

The holographic based methods have several advantages. Firstly, the optical system is a basic interferometer which is easy to setup. They also do not suffer from traditional optical aberrations

since no image forming lens is involved. Secondly, due to its long coherence length, the recorded hologram contains three-dimensional object wave information. Hence it is easily applied in tomography system. Thirdly, since the object image is calculated at a given focal distance, it enables digital auto-refocusing, which is more flexible than other image-plane techniques where mechanical tuning is required for refocusing. Lastly, as seen in the previous description of the technique, the digital holographic system is simple in configurations, which also brings down its cost.

However, the long coherence length of DHPM will usually introduce coherence artifacts and speckle noise. Coherence artifacts are mainly caused by multiple reflections from the surfaces in the imaging path, which will be discussed in detail in the SS-DHPM technique we proposed in the next chapter. Speckle noise is caused by spatial coherence of the illumination beam and hence a branch of recent digital holographic techniques incorporates low coherence source to overcome this issue [7]. Correspondingly, the image plane is placed closed to the hologram plane because of the short coherence length. These techniques, known as image plane digital holography, have seen successful popularization in diverse application areas such as biological microscopy [8,9] and particle velocimetry [10]. Compared to traditional holography, image plane holography can significantly improve light collection efficiency and save trouble for digital propagation.

2.1.2 Diffraction Phase Microscopy

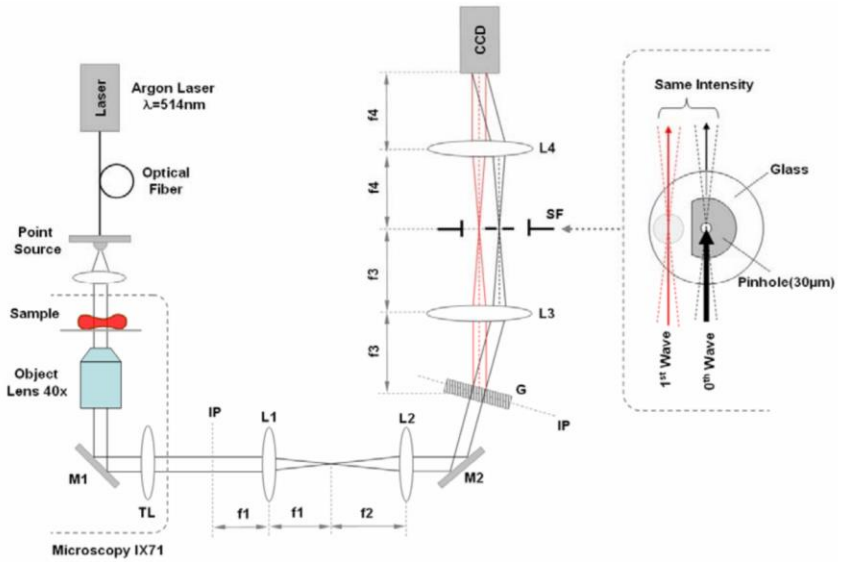

M1,2, mirrors; L1~4 lenses (f1~4, respective focal lengths); G, grating; SF, spatial filter; IP, image plane.

Fig. 2-1 Optical setup of diffraction phase microscopy [12]. Reprinted with permission from Dr. Gabriel Popescu.

In 2006, Popescu et al. proposed a highly sensitive QPI technique termed diffraction phase microscopy (DPM) [11,12]. It combines the features of two previously demonstrated techniques: the single shot feature of Hilbert phase microscopy [13] and the common path geometry of Fourier phase microscopy [14]. The term common path refers to the class of interferometry where the reference beam and sample beams travel along the same path. In its configuration (Fig. 2-2), a diffraction grating is utilized to split the two beams spatially. One of them (0^{th} order) is filtered to serve as the reference field, and the other (1^{st} order) serves as the scattered field and include the phase information of the sample. The signal processing steps employ a classic Fourier transform based method, which will be simply described here. Firstly, Fourier transform is applied to the interferogram with fringes. Only the side lobe on either positive or negative semi-plane is filtered and downshifted to DC. The phase of the inversed Fourier transform is retrieved and undergone 2D phase unwrapping to correct the phase jump ambiguity [15,16].

Since the invention of DPM, it has been recognized as a technique easy to access the microscope and perform multi-modal imaging, such as combining with fluorescence imaging channel [17]. DPM has also derived numerous branches: epi-DPM (The prefix epi stands for epi-illumination because the illumination and detection are on the same side of the sample) [18], white-light DPM [19], spectroscopic DPM [20] etc.

2.1.3 Quadriwave Lateral Shearing Interferometry

Lateral shearing interferometry is a well-established technique for phase gradients measurements. Its setup features a customized 2D diffraction grating named Modified Hartmann Mask is employed to generate four replicas of the incident beam [21]. In the combined intensity signal, gradients along two perpendicular directions are modulated onto spatial carriers as:

$$I(x,y,z) = I_0\left\{1+\left[\cos\left(\frac{2\pi}{p}x+\frac{2\pi}{p}z\frac{\partial L}{\partial x}\right)+\cos\left(\frac{2\pi}{p}y+\frac{2\pi}{p}z\frac{\partial L}{\partial y}\right)\right]\right\} + \frac{1}{2}\left[\cos\left(\frac{2\pi}{p}(x+y)+\frac{2\pi}{p}z\frac{\partial L}{\partial (x+y)}\right)+\cos\left(\frac{2\pi}{p}(x-y)+\frac{2\pi}{p}z\frac{\partial L}{\partial (x-y)}\right)\right]. \quad (2\text{-}2)$$

By filtering out selected components in Fourier domain, the phase gradient can be retrieved and then integrated to form phase image. Two advantages of QWLSI stand out: i) its common path configuration before the camera removes unnecessary environmental noises; ii). no modification is needed to access a commercial microscope or integrate with other imaging techniques such as fluorescence or qualitative techniques, and iii). broadband sources can be the illumination sources. Nevertheless, the downside for QWLSI is a 4 times reduction of the image resolution.

2.2 On-axis: Phase Shifting and Wavelength Shifting

In on-axis geometries, the object and reference fields propagate along the same axis. Therefore, a lower fringe density is expected in the interferogram and its Fourier transform should only show baseband (DC) component. The general expression of the interference signal will have three at least three unknowns: the amplitudes of both interfering fields and the unknown phase difference between them. Therefore, intensity equations under at least three conditions are required. This variation can be achieved by shifting the initial phase terms, which corresponds to phase shifting interferometry, and by shifting the wavelength, which corresponds to wavelength shifting interferometry.

2.2.1 Phase Shifting Interferometry

Phase shifting interferometry is a category of techniques that shifts the initial phase difference between the two interfering fields in a controllable manner when recording the interferograms.

Traditionally, PSI can refer to either phase stepping techniques or bucket integrating techniques. The major distinction is whether the phase shift is continuous or discrete. However, since the latter one only introduce a smaller visibility factor [22] and both share the same signal model, they are treated here indiscriminately. The general expressions of PSI can be written as:

$$\begin{aligned}\overline{I_n} &= \alpha\left[1+V\cos\left(k_0 L+\varphi_n\right)\right] \\ &= \alpha+\beta\cos\left(k_0 L+\varphi_n\right)\end{aligned},\ n=1\sim N, \tag{2-3}$$

By taking different N and φ_n values, there exist a broad spectrum of phase modulation techniques. Creath (1988) proposed a 3-step technique with an equal phase step of θ so that the phase shift set $\mathbf{\Phi}=\{\varphi_n\}=[-\theta,0,\theta]$[23]. θ can take any arbitrary value as long as it is known beforehand. Another well-known 3-step technique was proposed by Wyant et al. [24]. It is different from the previous 3-step technique in that it has a phase step of $\pi/2$ and an extra $\pi/4$ offset, thus making $\mathbf{\Phi}=[\pi/4,3\pi/4,5\pi/4]$.

Probably the most famous technique is the 4-step ($\pi/2$) technique with $\mathbf{\Phi}=[0,\pi/2,\pi,3\pi/2]$. A very successful implementation of the 4-step technique is termed spatial light interference microscopy (SLIM) [25]. SLIM is similar to Fourier phase microscopy [14], both utilizing a liquid crystal spatial light modulator to shift the phase in the time domain. After the light pass through the specimen, it will be divided into unscattered and scattered portions. The unscattered portion (background) will experience the additional phase delays when reflecting off the spatial light modulator and interfere with the scattered field.

Another 4-step modulation technique is known as the Carré method [26]. Carré method does not assume any particular phase step, as long as the phase shifts between successive frames are equal. In this scenario, $\mathbf{\Phi}=[-3\theta/2,-\theta/2,\theta/2,3\theta/2]$, and here the phase step θ can be an arbitrary unknown value. Because of this, the algorithm for Carré method differs completely from the previous 4-step technique. This algorithm inspires the development of the LC-WSI technique we will propose in the next chapter.

When phase steps are more than four, two famous benchmark algorithms are mostly used. The first is a 5-step PSI technique proposed by Hariharan et al [27]. Five measurements of

interferogram are taken with linear phase shift between frames. Similar to the 3-step (θ) case, the preset phase step can vary, but the best value is determined as $\pi/2$ to make it insensitive to phase shift calibration errors. The other multi-frame-technique is the *N*-step synchronous method proposed by Bruning et al [28]. It is a category of techniques with N phase shifts and phase step $\theta = 2\pi/N$.

On-axis PSI can maintain system resolution and field of view (FOV). In addition, the demodulation only requires simple mathematical operations. PSI techniques also have limitations. One of them is the reduced acquisition rate due to its multi-acquisition nature. This constraint, however, can be alleviated to some degree with the continuing development of commercial high-speed cameras. More important restrictions stem from the use of phase shifters. The incorporation of these devices typically requires substantial customization of an otherwise conventional interferometer. For example, different types of phase shifters in distinct configurations are used to convert a conventional microscope for quantitative phase contrast [25], polarized light [29], and differential interference contrast microscopy [30]. Clearly, hardware uniqueness and heterogeneity hinder the integration of various techniques for multi-modality imaging.

2.2.2 Wavelength Shifting Interferometry

A potential solution to avoid hardware uniqueness is WSI, a technique that removes phase shifter and the associated need for interferometer modification. Instead, the phase shift is generated by wavelength change of the light source. Traditional WSI techniques, such as discrete wavelength stepping [31] and bucket integrating [32,33] methods, are based on highly coherent lasers tuned by current or temperature. Their tuning range, speed, and repeatability are restricted and are often associated with severe coherence artifacts, limiting their applications in high-quality imaging of microscopic objects such as biological cells.

2.3 Discussions

In this chapter two major full-field QPI geometries and their principles are introduced. Compared to off-axis geometries, on-axis geometries maximize the space–bandwidth product but compromise on the time–bandwidth product [34]. Thus there is always a tradeoff between the

selection of on-axis and off-axis methods, and the selection criteria will always depend on speed, cost, and type of equipment involved in a specific application.

Through this review of full-field based QPI techniques, it is also clear that some features and capabilities of the systems are not inherent to a specific geometry. For example, techniques from both geometries can have common path implementations for a compact design, or incorporate low coherence source to remove coherence artifacts. These updates in system hardware usually do not affect signal processing methods severely. By reviewing the current state-of-the-art techniques, insights can be gained into system design and optimization for QPI techniques.

References

[1] D. Gabor, "A new microscopic principle," Nature, 161(4098), 777-778 (1948).

[2] E. N. Leith and J. Upatnieks, "Reconstructed Wavefronts and Communication Theory," Journal of the Optical Society of America, **52**(10), 1123-1130 (1962).

[3] J. W. Goodman, and R. W. Lawrence, "Digital image formation from electronically detected holograms," Applied Physics Letters, **11**(3), 77-79 (1967).

[4] U. Schnars, and W. Jüptner, "Direct recording of holograms by a CCD target and numerical reconstruction," Applied Optics, **33**(2), 179-181 (1994).

[5] E. Cuche, F. Bevilacqua, and C. Depeursinge, "Digital holography for quantitative phase-contrast imaging," Optics Letters, **24**(5), 291-293 (1999).

[6] E. Cuche, P. Marquet, and C. Depeursinge, "Simultaneous amplitude-contrast and quantitative phase-contrast microscopy by numerical reconstruction of Fresnel off-axis holograms," Applied Optics, **38**(34), 6994-7001 (1999).

[7] M. K. Kim, "Principles and techniques of digital holographic microscopy," Journal of Photonics for Energy, 018005-018005 (2010).

[8] C. J. Mann, L. Yu, C. M. Lo, and M. K. Kim, "High-resolution quantitative phase-contrast microscopy by digital holography," Optics Express, **13**(22), 8693-8698 (2005).

[9] M. K. Kim, L. Yu, and C. J. Mann, "Interference techniques in digital holography," Journal of Optics A: Pure and Applied Optics, **8**(7), S518 (2006).

[10] M. P. Arroyo, and J. Lobera, "A comparison of temporal, spatial and parallel phase shifting algorithms for digital image plane holography," Measurement Science and Technology, **19**(7), 074006 (2008).

[11] G. Popescu, T. Ikeda, R. R. Dasari, and M. S. Feld, "Diffraction phase microscopy for quantifying cell structure and dynamics," Optics letters, **31**(6), 775-777 (2006).

[12] Y. Park, G. Popescu, T. Ikeda, K. Badizadegan, R. R. Dasari, and M. S. Feld, "Diffraction Phase Microscopy," in *Biomedical Optics,* Technical Digest (CD), paper TuI50 (Optical Society of America, 2006).

[13] T. Ikeda, G. Popescu, R. R. Dasari, and M. S. Feld, "Hilbert phase microscopy for investigating fast dynamics in transparent systems" Optics Letters, **30**(10), 1165-1167 (2005).

[14] G. Popescu, L. P. Deflores, J. C. Vaughan, K. Badizadegan, H. Iwai, R. R. Dasari, and M. S. Feld, "Fourier phase microscopy for investigation of biological structures and dynamics," Optics Letters, **29**(21), 2503-2505 (2004).

[15] H. Pham, H. Ding, N. Sobh, M. Do, S. Patel, and G. Popescu, "Off-axis quantitative phase imaging processing using CUDA: toward real-time applications," Biomedical Optics Express, **2**(7), 1781-1793 (2011).

[16] B. Bhaduri, C. Edwards, H. Pham, R. Zhou, T. H. Nguyen, L. L. Goddard, and G. Popescu, "Diffraction phase microscopy: principles and applications in materials and life sciences," Advances in Optics and Photonics, **6**(1), 57-119 (2014).

[17] Y. Park, G. Popescu, K. Badizadegan, R. R. Dasari, and M. S. Feld, M. S, "Diffraction phase and fluorescence microscopy," Optics Express, **14**(18), 8263-8268 (2006).

[18] C. Edwards, B. Bhaduri, B. G. Griffin, L. L. Goddard, and G. Popescu, "Epi-illumination diffraction phase microscopy with white light," Optics Letters **39**(21), 6162-6165 (2014).

[19] B. Bhaduri, H. Pham, M. Mir, and G. Popescu, “Diffraction phase microscopy with white light,” Optics Letters **37**(6), 1094-1096 (2012).

[20] H. Pham, B. Bhaduri, H. Ding, and G. Popescu, “Spectroscopic diffraction phase microscopy,” Optics Letters **37**(16), 3438-3440 (2012).

[21] P. Bon, G. Maucort, B. Wattellier, and S. Monneret, “Quadriwave lateral shearing interferometry for quantitative phase microscopy of living cells,” Optics Express, **17**(15), 13080-13094 (2009).

[22] C. L. Koliopoulos, “Interferometric optical phase measurement techniques,” A Dissertation Submitted to the Faculty of the Committee on Optical Sciences (Graduate), University of Arizona (1981).

[23] K. Creath, “Phase-measurement interferometry techniques,” Progress in Optics, **26**, 349-393 (1988).

[24] J. C. Wyant, C. L. Koliopoulos, B. Bhushan, and O. E. George, “An optical profilometer for surface characterization of magnetic media,” ASLE Transactions, **27**, 101-113 (1984).

[25] Z. Wang, L. Millet, M. Mir, H. Ding, S. Unarunotai, J. Rogers, M. U. Gillette, and G. Popescu, "Spatial light interference microscopy (SLIM)," Optics Express **19**, 1016-1026 (2011).

[26] P. A. A. M. Junior, P. S. Neto, and C. S. Barcellos, “Generalization of Carré equation,” Optik-International Journal for Light and Electron Optics **122,** 475-489 (2011).

[27] P. Hariharan, B. F. Oreb, and T. Eiju, “Digital phase-shifting interferometry: a simple error-compensating phase calculation algorithm,” Applied Optics **26,** 2504-2506 (1987).

[28] J. H. Bruning, D. R. Herriott, J. E. Gallagher, D. P. Rosenfeld, A. D. White, and D. J. Brangaccio, “Digital Wavefront Measuring Interferometer for Testing Optical Surfaces and Lenses,” Applied Optics **13**, 2693-2703 (1974).

[29] R. Oldenbourg, and G. Mei, “New polarized light microscope with precision universal compensator,” Journal of microscopy, **180**(2), 140-147 (1995).

[30] C. J. Cogswell, N. I. Smith, K. G. Larkin, and P. Hariharan, “Quantitative DIC microscopy using a geometric phase shifter,” in *Three-Dimensional Microscopy: Image Acquisition and Processing IV* (Vol. 2984, pp. 72-82). International Society for Optics and Photonics (1997).

[31] T. Takahashi, Y. Ishii, and R. Onodera, “Phase-shifting interferometric profilometry with a wavelength-tunable diode source,” Optical Review, **21**(3), 410-414 (2014).

[32] K.Tatsuno, and Y. Tsunoda, “Diode laser direct modulation heterodyne interferometer,” Applied Optics, **26**(1), 37-40 (1987).

[33] Y. Ishii, “Laser-diode interferometry,” Progress in Optics, **46**, 243-309 (2004).

[34] A. W. Lohmann, R. G. Dorsch, D. Mendlovic, C. Ferreira, and Z. Zalevsky, “Space–bandwidth product of optical signals and systems,” Journal of the Optical Society of America A, **13**, 470-473 (1996).

Chapter 3 Wavelength Shifting Interferometry

In this chapter two full-field QPI techniques based on wavelength shifting interferometry (WSI) are proposed. WSI utilizes an on-axis geometry and hence no compromise is made in terms of spatial resolution. By shifting the wavelength of illumination while recording the interferograms, the time domain is also the spectral domain. As mentioned in Chapter 2, hardware uniqueness and heterogeneity hinder the integration of various techniques for multi-modality imaging. WSI, compared to its on-axis counterpart phase shifting interferometry (PSI), removes the phase shifter from the interferometer and maintains the integrity of a basic interferometer. The simplicity of the WSI platform provides easy access to reusing the optical path of a commercial microscope. In the meantime, it is advantageous in the integration of other imaging modes because mode switching can be done by adding and removing specialized optical components (i.e. polarizer, diaphragm, prism) in the optical path instantly.

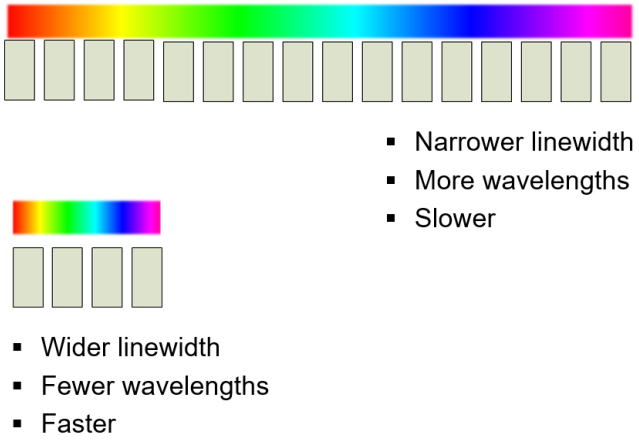

Fig. 3-1 An analogy of many-wavelength-mode and multi-wavelength-mode operations of the swept source. The actual scanning range for our swept source is 802-878nm, in near infrared region.

The light source used in the proposed techniques is an acousto-optic tunable filter (AOTF) based swept laser source. With two different operation modes (an analogy is shown in Fig. 3-1), different functionalities can be achieved. The many-wavelength mode requires dense sampling in wavelength (narrow linewidth for each) and modulates the phase information onto a spectral carrier, termed swept-source digital holographic phase microscopy (SS-DHPM). Although the coherence length is long as in other digital holographic techniques, it can identify and avoid the coherence artifacts in the spectral domain. With the spectral information, SS-DHPM has an

additional benefit of performing spectroscopic measurements. The second mode, compared to the first mode, requires only multi-wavelength acquisitions, largely improving the speed and enables imaging fast dynamics. Meanwhile, for each acquisition of the camera, the AOTF scans a range of wavelength within the exposure time (wider linewidth), providing a temporal low coherence illumination and hence termed low coherence wavelength shifting interferometry (LC-WSI). It is worth mentioning that although these two modes share a similar platform, the corresponding techniques have very different signal processing algorithms, whose details will be shown as follows.

3.1 Many-wavelength-mode: SS-DHPM

3.1.1 System Setup

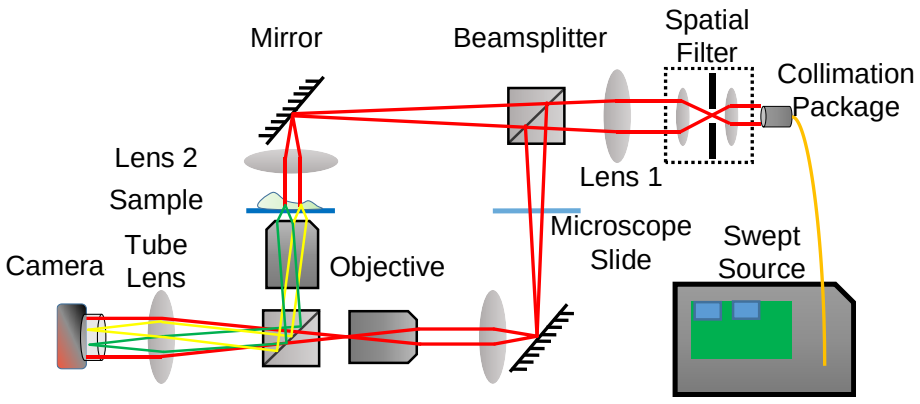

Fig. 3-2 Schematic of the swept source DHPM system.

We demonstrate the technique using an on-axis DHPM setup based on a Mach-Zehnder interferometer (Fig. 1). Light from a swept source (Superlum; BS-840-1, 802-878 nm) is spatially filtered and collimated. It is then split into sample and reference arms with matching optics to eliminate chromatic dispersion. Before entering the objective (Nikon; 40×, NA 0.75), the beam size is reduced to avoid diffraction at the edge of the objective lenses. The sample is sandwiched by a No. 1.5 coverslip at the bottom and a microscope slide on top and is placed at the focal plane of the sample arm objective. In the reference arm, microscope slides are inserted to adjust the optical pathlength (OPL) difference between the two arms. This generates a carrier frequency (CF) for the signal, as explained later. A tube lens then forms images of both sample and reference fields on the camera (Allied Vision; Mako G030, 300 fps), producing an on-axis interferogram. The source sweep is synchronized with the camera such that interferograms are acquired at evenly

sampled wavenumbers throughout the spectral range. The number of acquired interferograms and the total acquisition time can be adjusted by tuning sweep speed. A single sweep thus produces an interference spectrum for each image point, which is further processed to obtain phase or spectroscopic information about the sample. The sweep is repeated for continuous monitoring.

3.1.2 Signal Processing

3.1.2.1 Signals

Denoting the reference field as simply E_R and sample field as $E_S \exp\left[jk(L_0 + L_s)\right]$, where E_s is the amplitude, k is wavenumber, L_0 is the OPL difference between the two arms, and L_s is the sample OPL distribution, the interferogram on the camera can be written as:

$$I(k) = \left|E_S\right|^2 + \left|E_R\right|^2 + 2E_S E_R \cos[k(L_0 + L_s)] \tag{3-1}$$

We note that E_s, L_s and hence $I(k)$ also depends on sample position. Since L_0 is on the order of hundreds of micrometers, the interference in Eq. (1) is a high-frequency signal. This is in contrast to conventional on-axis low coherence holography, which has nearly matched OPL. As a result, by sweeping k, L_0 generates a spectral carrier that modulates sample signal to a high-frequency region, the exact position of which is selected to avoid undesirable interference artifacts.

3.1.2.2 Coherence Artifacts

A common challenge in laser-based DHPM systems is the long coherence length, which generates undesirable artifacts in holograms and affects measurement accuracy and sensitivity. These artifacts are typically due to the interference of diffused scattering along the beam path or non-signal reflections from various optical components, such as the protection coverglass on top of the camera sensor. This is commonly resolved by coverglass removal, which however exposes the sensor to contamination and does not address artifacts from other sources. Low coherence holographic techniques are proposed to minimize these artifacts, but often compromising system simplicity with sophisticated phase front matching schemes or sacrificing axial or lateral field of view (FOV) when using conventional geometries [1-3].

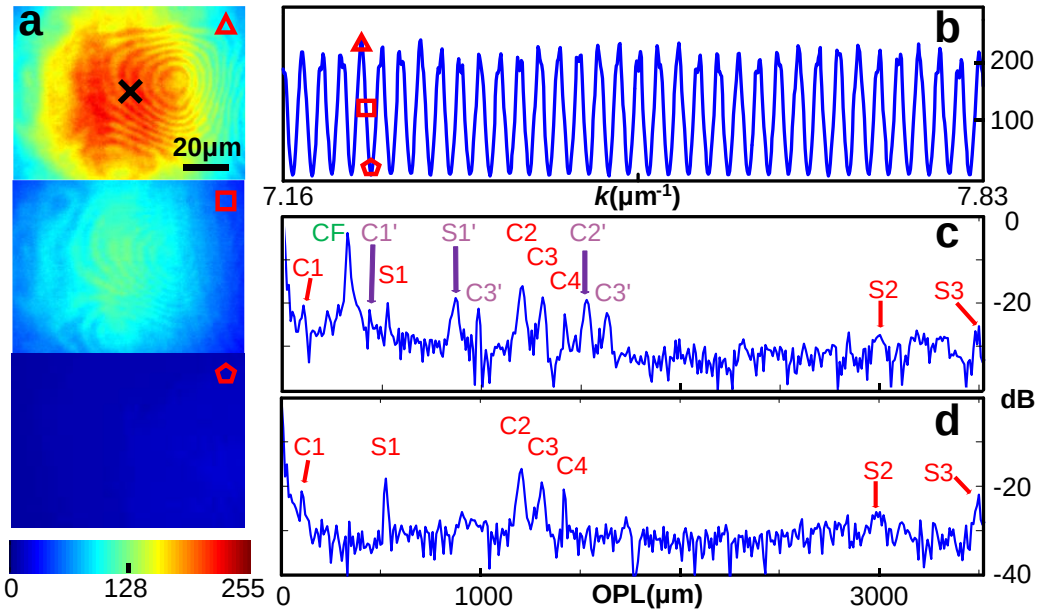

Fig. 3-3 Signals of SS-DHPM. (a) Typical full-field interferograms at wavelengths marked in (b). (b) Full spectrum for position cross-marked in (a). (c) FT of (b) showing sample signal and undesirable interferences. (d) FT of sample-arm-only intensity images. C1-C4, interference peaks from camera; S1-S3, interference peaks from sample chamber; primed symbols, twin peaks of C1-C3 and S1 shifted by sample-reference interference.

To this end, we first examine the causes of various interference artifacts in our system using a water-filled, blank sample chamber. The interferograms at different wavelengths are shown in Fig. 3-3(a), clearly displaying undesirable patterns.

Figures 3-3 (b) and (c) show the full spectrum at the fixed position marked with a cross and its Fourier transform (FT), respectively. In addition to the signal peak at CF, there are also a number of non-signal peaks. They originate from various system components and can be identified by finding their OPL. For example, S1 matches the thickness of the coverslip of the sample chamber and S2 is due to the microscope slide with S3 being the sum of S1 and S2. In the camera, C1 and C2 are from the protection coverglass while C3 is their sum. Peak C4 can be linked to both coverglass and sensor surface reflection. The remaining peaks (primed symbols) are “twin peaks”, which are versions of the original ones shifted by sample-reference interference. This can be verified by acquiring only sample arm signal, as shown in Fig. 3-3(d), where these twin peaks are eliminated.

These artifact peaks can be extracted by bandpass filtering to inspect their individual spatial intensity pattern (Fig. 3-4), which are most likely due to variations in thickness or surface flatness

of the components causing the reflection. Although C1 shows distinct patterns that can be easily identified in the original interferograms [Fig. 3-4(a)], other peaks display only subtle spatial changes that can hardly be observed without examining the full interference spectrum. Significantly, this suggests the apparent "cleanness" of a conventional single-wavelength interferogram does not ensure it is artifact-free. The impact of these artifacts on phase images will be quantified later.

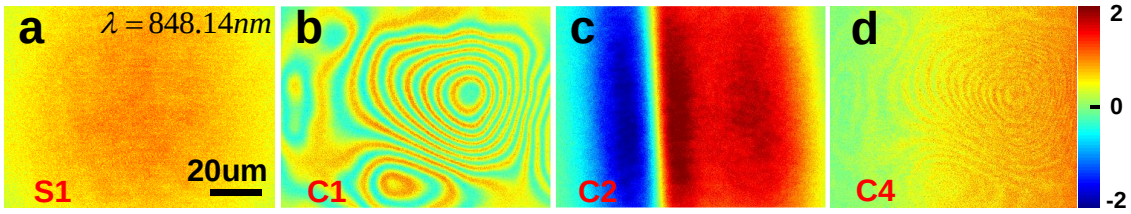

Fig. 3-4 Examples of spatial intensity images of artifacts after bandpass filtering

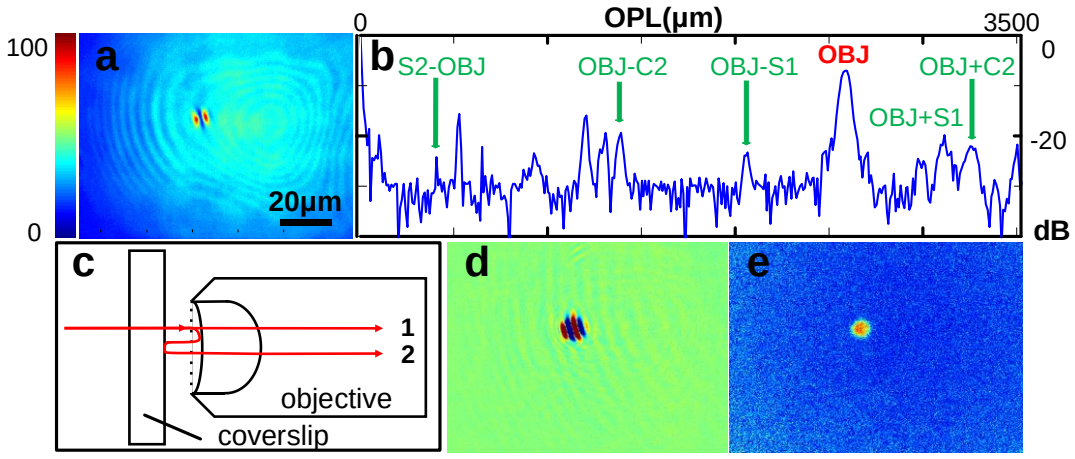

Fig. 3-5 Localized artifact from the objective. (a) Intensity image with the high visibility spot. (b) FT of the spectrum from affected position, where only objective-related peaks are marked. (c) Illustration of the cause. 1, direct field; 2, objective reflection. (d) Bandpass filtered image of peak OBJ. (e) Intensity image of the objective reflection.

In addition to these interferences that affect the entire FOV, we have also observed a highly localized artifact stemming from the sample objective. As shown in Fig. 3-5(a), a bright spot appears near the center usually when optics is well aligned and the camera is centered about the optical axis. In other areas, the image is unaffected and the FT remains the same as in Fig. 3-3(d). On the spot, however, its FT [Fig. 3-5(b)] reveals an additional strong interference (peak OBJ). Its OPL indicates that it is from the reflection of the concave surface of the objective front lens, which focuses the reflection back onto the coverslip [Fig. 3-5(c)]. When imaged onto the camera, it

interferes with the direct field, producing the local interference. Figures 3-5(d) and (e) show its bandpass filtered image and the associated intensity distribution. Since the spot is essentially the image of the focused reflection, it can be moved out of FOV by adjusting the objective or camera position. This is done for experiments of Fig. 3-3 and Fig. 3-4, and all routine sample imaging. We also note that the spot's position and strength may vary with objective geometry, working distance, and sample chamber design.

Above findings show that in a laser-based holographic phase microscopy system, a number of components may cause undesirable artifacts. Removing camera coverglass only eliminates some of them, yet it exposes the sensor to high risk of contamination. Further, monitoring interferogram quality is an unreliable way to ensure artifact removal. With a swept source, however, it is possible to not only identify artifacts sources but avoid them by positioning sample signal in a clean region of frequency.

3.1.2.3 OPL Retrieval

With a series of wavelength-dependent interferograms, there are two methods to calculate the quantitative OPL images. First, the full spectrum at each image pixel enables the calculation of absolute OPL difference at that position [4]. This is particularly useful when a sample exhibits large OPL discontinuities where unwrapping would fail. For biological specimens, abrupt OPL changes are rare and relative OPL can be obtained using the more popular and faster FT-based procedure [5].

In brief, the phase of the CF peak [Fig. 3-3(c)] at each image pixel is extracted, unwrapped and then converted to relative OPL using center wavenumber. In our following experiments, the second method is used to produce our OPL images. We also perform background subtraction by taking a sample-less image.

3.1.3 Results and Discussions

3.1.3.1 Sensitivity Characterization

We first study the impact of artifacts on phase images using a blank sample. Three cases are compared: CF peak overlapping with artifacts C1, C2 or clean background. Each measurement takes one sweep of the source to acquire 228 frames in 0.76 s with an equivalent laser linewidth of 0.1 nm. Their phase images are shown in Fig. 3-6(a)-(c). It is clear that C1 and C2 cause fixed

pattern phase errors of several nanometers, which could hinder precise analysis of phase features of comparable magnitude. It should be noted that these errors are system dependent and could potentially be more severe. In comparison, Fig. 3-6(c) shows a substantially cleaner phase image, which also represents the system's spatial noise distribution. Its standard deviation, or the spatial phase sensitivity, is calculated to be 0.27 nm across the full FOV (120 μm × 90 μm), as shown in Fig. 3-6(d).

The temporal OPL sensitivity is also quantified by repeating the measurement 20 times and calculating the OPL standard deviation at each pixel [Fig. 3-6(e)]. The mean sensitivity over the full FOV is 0.26 nm. The spatial variation is attributed to the Gaussian beam profile, which has reduced signal-to-noise ratio and lower sensitivity toward the edge.

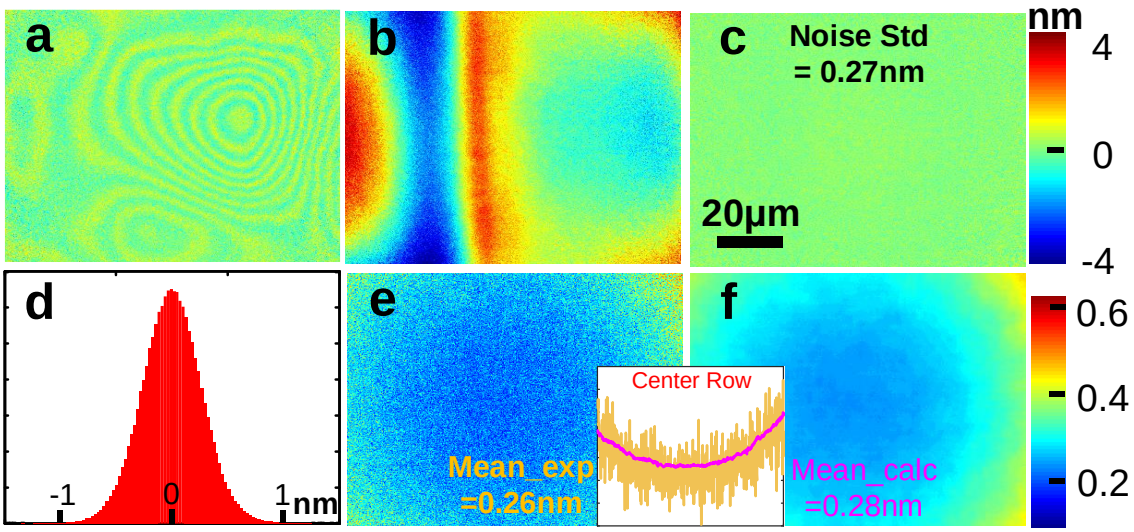

Fig. 3-6 (a)-(c) OPL images when CF is overlapped with artifacts C1, C2 and clean background, respectively. (d) Spatial noise distribution of (c). (e)-(f) Temporal sensitivity distribution and theoretical calculation (inset: center row comparison).

While the OPL sensitivity is excellent, it is important to ask if it has reached shot noise-limited performance and if the swept source contributes to the noise. It is known in optical coherence tomography that swept source-based phase measurement is typically less stable than spectrometer-based approach [5], likely due to repeatability issues associated with high speed sweeping and sampling. To compare our measurement to theory, we have derived the shot noise-limited OPL sensitivity for a given interference spectrum, following a similar Fourier domain procedure described in [6].

The derivation is outlined as follows. The camera readout for the *n*-th wavenumber can be written as $I_n + e_n$ with e_n being the noise. Since shot noise follows Poisson distribution, we have the variance $Var(e_n) = I_n / g$, where *g* is camera gain, i.e. the number of photo-generated electrons per analog-to-digital unit.

Next, we find the complex amplitude (thus the phase) of the signal peak in the discrete FT (DFT) of the spectrum. Both I_n and e_n contribute to this amplitude. Using Eq. (3-1), the former can be written as $(V\sum_{n=1}^{N} I_n)/2$ with $V = 2E_S E_R / (|E_S|^2 + |E_R|^2)$ being fringe visibility. Assuming the peak is located at an integer *m* in the DFT for convenience, the contribution of e_n follows $\sum_{n=1}^{N} e_n \exp[-j2\pi m(n-1)/N]$ from DFT definition. The complex peak amplitude is thus the sum of the two parts. Since e_n is much smaller than I_n, the peak angle can thus be approximated as simply the ratio of the imaginary part of the e_n's contribution to I_n's contribution. The standard deviation of the angle can then be determined using the variance of e_n mentioned above. Converting it to OPL, the shot noise-limited OPL sensitivity for this signal processing algorithm is thus

$$\sigma_t \cong \frac{1}{k_0 V}\sqrt{\frac{2}{g\sum_{n=1}^{N} I_n}} \tag{3-2}$$

where k_0 is the center wavenumber.

Using Eq. (3-2), the theoretical temporal sensitivity for the entire FOV is computed and shown in Fig. 3-6(f). The distribution pattern and values are in excellent agreement with experimental results (error standard deviation of 0.04 nm).

3.1.3.2 Live Cell Imaging

To demonstrate the technique's potential application to live cell imaging, swine sperm cells were imaged. Sperm morphology is one of the most important parameters in semen analysis. It is highly correlated to sperm quality and the outcome of pregnancy during in vitro fertilization [7]. Compared to conventional assessment based on qualitative imaging, DHPM provides a wealth of quantitative information with great potential to improve sperm quality control [8]. Here, swine

semen was collected from a Large White crossbreed boar and was extended in AndroPro Plus extender (MOFA, USA) and stored at 17°C. Before experiments, the sample was diluted with sperm wash medium and cooled to reduce its mobility. As often with other image plane holographic techniques, the measured complex field of the sample is digitally refocused in post processing if needed [9].

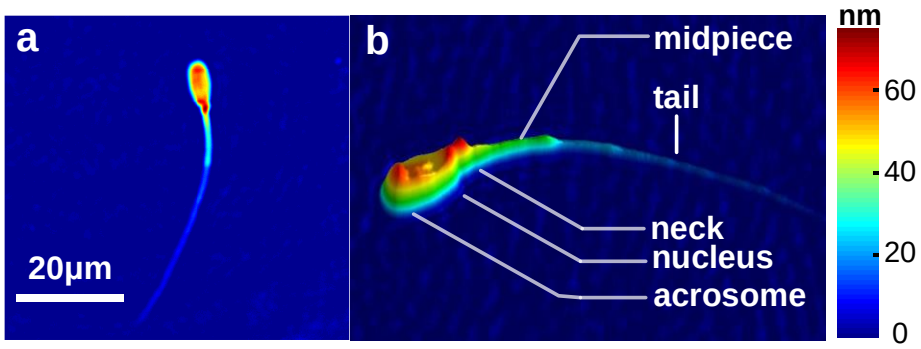

Fig. 3-7 Quantitative OPL images of a swine sperm cell.

Figure 3-7 shows the demodulated OPL images of a sperm cell. Since the CF is positioned in a clean region as in Fig. 3-3(c), the image does not have observable artifacts. In Fig. 3-7(b), distinct morphological features can be clearly identified in a quantitative manner, including acrosome and nucleus in the sperm head, as well as the mitochondria-rich midpiece, all of which lead to locally increased OPL. The largest OPL is recorded in the neck area, although its mechanism is not yet clear. These features are consistent with a previous report of swine sperm phase images [10], but show evident interspecific difference from those of other species such as human [8,11]. Detailed mechanisms of these phase characteristics are under further investigation.

3.1.4 Spectroscopy

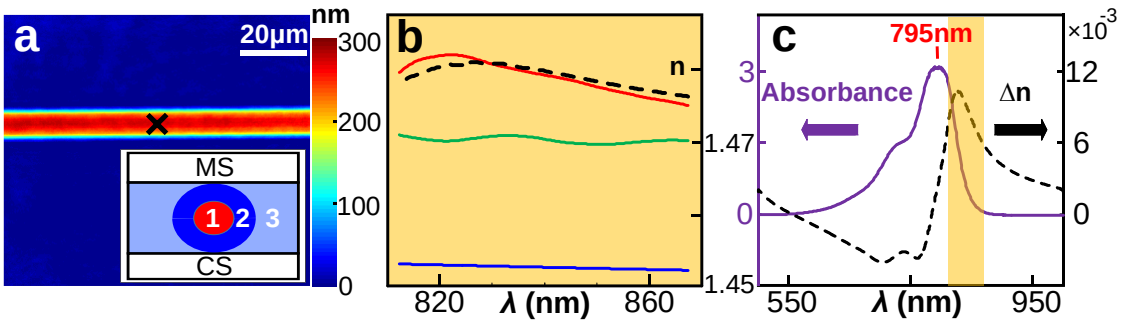

Fig. 3-8 Spectroscopic imaging. (a) OPL image of ICG solution. Inset: cross section of sample chamber. 1, ICG/DMSO-filled capillary core; 2, capillary wall; 3, index matching liquid; MS, microscope slide; CS, coverslip. (b) Refractive indices of ICG/DMSO (red) for position cross-marked in (a), theoretical calculation [dashed line, from the highlighted spectral region in (c)], pure DMSO (green) and fused silica glass (blue). (c) Measured absorbance of ICG/DMSO sample (solid) and the calculated refractive index change curve (dashed). Highlighted area is the full sweep range of our system, as in part (b).

In addition to OPL imaging, the access to full spectrum also permits the retrieval of spectroscopic information [3,12]. To demonstrate this capability, we measure the wavelength-dependent refractive indices (R.I.) of indocyanine green (ICG), which has an absorption peak at 795 nm, resulting in dispersion in our measurement spectral range. Sample is prepared by loading 10 μM solution of ICG in dimethyl sulfoxide (DMSO) into a fused silica capillary tube (Polymicro; ID 10 μm, OD 125 μm). The tube is then placed in sample chamber, immersed in index liquid that matches fused silica [Fig. 3-8(a)].

To extract dispersion, we adopt an algorithm previously designed for spectral modulation interferometry [13]. Briefly, it treats the OPL dispersion in Eq. (3-1) as modulating a wavelength-dependent phase term onto the CF, similar to the technique of phase modulation in analog communication. Therefore, the signal peak in Fig. 3-3(c) contains not just a single OPL quantity, but the dispersion of OPL. The peak is then filtered out and downshifted to DC and its OPL is extracted as a function of wavelength. For example, Fig. 3-8(a) shows the OPL image at 838 nm (corresponding to k_0). By comparing the OPL inside (ICG/DMSO) and outside (fused silica) of the core, the refractive index difference between the two materials can be determined.

Figure 3-8(b) shows the published R.I. of fused silica [14] as a baseline (blue) and the ICG/DMSO R.I. measurement curve (red) for a single pixel on the central axis of the tube. The R.I. of pure DMSO is also measured (green) and is consistent with reported value [15]. To verify the result of ICG/DMSO, we measure its absorbance and calculate the theoretical R.I. curve [Fig.

3-8(c)] from the Kramers-Kronig relations [3], which is in good agreement with the direct measurement in Fig. 3-8(b).

3.2 Multi-wavelength-mode: LC-WSI

3.2.1 System Setup

LC-WSI is a broadband interferometric technique that can minimize coherent artifacts and also improve the imaging speed relative to the previous many-wavelength-mode technique, SS-DHPM. LC-WSI uses a simple Mach-Zehnder interferometer-based system coupled with a swept laser source, identical to the one in the many-wavelength-mode technique, SS-DHPM, except for one fundamental difference: the OPL difference between the two arms (adjusted by placing coverglass of different thickness in the reference arm). Instead of the several hundred micrometers in SS-DHPM, LC-WSI requires L to be much smaller, the reason for which will be explained next with simulation. To acquire one phase image, the source (Superlum; BS-840-1) sweeps linearly in wavenumber from 878 nm to 816 nm and the camera (Allied Vision; Mako G030) is synchronized to capture four interferograms. Due to the continuous sweep and nontrivial exposure time (3 ms), the camera integrates over four broad wavelength bands (~14.5 nm each, centered at 869.65 nm, 853.45 nm, 837.85 nm and 822.80 nm), which are evenly spaced in wavenumber by Δk =0.137 μm^{-1}. Low coherence operation of LC-WSI can minimize various types of coherence noises. The camera operates at a rate of 250 fps, equivalent to an imaging rate of 62.5 Hz.

3.2.2 Signal Processing

Here, we use the special case of four-wavelength-band LC-WSI to introduce its concept, characterize and demonstrate its performance for dynamic live cell imaging.

For the operation of LC-WSI, we consider the interference between two fields E_s and E_r as a function of time delay τ between the two fields [16]:

$$I(\tau) = |E_s|^2 + |E_r|^2 + 2|E_s||E_r|\,\mathrm{Re}\{\Gamma(\tau)\}, \tag{3-3}$$

where $\Gamma(\tau)$ is the temporal correlation function. According to the generalized Wiener-Khintchin theorem, $\Gamma(\tau)$ is also the Fourier transform of the normalized source power spectrum density

$S(\omega)$. Assuming this spectral shape is centered at ω_1 so that we can define a shifted spectrum $S_1(\omega) = S(\omega + \omega_1)$, $\Gamma(\tau)$ can be further given as:

$$\Gamma(\tau) = \int S_1(\omega - \omega_1) e^{j\omega\tau} d\omega = e^{j\omega_1\tau} \int S_1(\omega) e^{j\omega\tau} d\omega = |\gamma_1(\tau)| e^{j[\omega_1\tau + \xi_1(\tau)]}, \tag{3-4}$$

wherein $|\gamma_1(\tau)|$ and $\xi_1(\tau)$ are the magnitude and phase responses of the Fourier transform of $S_1(\omega)$, respectively. We also note that $\omega_1\tau = k_1 L$, in which k_1 is the wavenumber corresponding to ω_1 and L is the optical pathlength (OPL) difference between the two fields. Therefore in LC-WSI, for the n^{th} wavelength band with center wavenumber k_n, the detected intensity can be obtained by combining Eqs. (3-3) and (3-4):

$$\begin{aligned} I_n &= |E_{sn}|^2 + |E_{rn}|^2 + 2|E_{sn}||E_{rn}||\gamma_n|\cos(k_n L + \xi_n) \\ &= |E_{rn}|^2 \left[\frac{|E_{sn}|^2}{|E_{rn}|^2} + 1 + 2\frac{|E_{sn}|}{|E_{rn}|}|\gamma_n|\cos(k_n L + \xi_n) \right], n = 1, ..., N \end{aligned} . \tag{3-5}$$

Equation (3-5) can be further simplified under several conditions: (1) the spectrum of each band is symmetric about its own k_n so that $\xi_n = 0$; (2) all N bands have a common spectral shape, which means $|\gamma_n(\tau)|$ are identical; (3) the intensity ratios $|E_{sn}|/|E_{rn}|$ are the same for all bands; (4) k_n are evenly spaced by Δk. For the case of four-band LC-WSI (N =4), Eq. (3-5) can now be rewritten as:

$$\frac{I_n}{|E_{rn}|^2} = a + b\cos(k_0 L + \phi_n) \ ,$$

$$n = 1 \sim 4 \text{ and } \phi_n = \left\{ -\frac{3}{2}\Delta kL, -\frac{1}{2}\Delta kL, \frac{1}{2}\Delta kL, \frac{3}{2}\Delta kL \right\}, \tag{3-6}$$

where a and b are magnitude constants independent of n, $k_0 = (k_1 + k_4)/2$ is the center wavenumber of the full spectrum, and the additional phase terms ϕ_n, although unknown because of L, are evenly spaced by $\Delta\phi = \Delta kL$. In the following, we simply use I_n to represent the normalized intensity in the left-hand side of Eq. (3-6).

Eq. (3-6) is a special case of LC-WSI, but has the exact mathematical form that can be processed by the Carré algorithm designed for PSI [17]. The OPL can thus be demodulated as:

$$L' = \frac{1}{k_0}\arctan\left\{\frac{\sqrt{\left[3\left(I_2 - I_3\right) - \left(I_1 - I_4\right)\right]\left(I_2 - I_3 + I_1 - I_4\right)}}{\left(I_2 + I_3 - I_1 - I_4\right) \times \mathrm{sgn}\left(I_2 - I_3\right)}\right\}, \tag{3-7}$$

Eq. (3-7) is a modified version of the original Carré equation with the addition of a signum function to resolve the quadrant ambiguity of the arctangent function, as explained later. It produces the OPL image of the sample. When sample OPL is too large and thus wrapped, Eq. (3-7) will be followed by a routine 2D unwrapping process.

Finally, we examine that the above conditions to use Eq. (3-6) are indeed met with our swept source based system and the operation described in previous section : (1) and (2) can be satisfied with our swept source which has a rather even spectrum response across the full sweeping range; (3) is typically true for transparent phase objects and determined only by the splitting ratio of the interferometer; (4) is satisfied by the linear k sweep. Further, the intensity normalization in Eq. (3-6) can be implemented using the reference arm intensity obtained by blocking the sample arm.

3.2.3 Results and Discussions

3.2.3.1 Simulation

To understand the behavior of this system, we first simulate its performance. The same center wavelengths and bandwidths as in actual experiments are used. Signal strength and the associated shot noise are simulated based on the measured electron saturation capacity of the camera (9000 e^-). I_n for a wide range of L are generated and processed respectively by both original Carré equation and our modified version in Eq. (3-7). Before unwrapping, the OPL obtained by original Carré equation has the ambiguous “M” shape [Fig. 3-9(a)], whilst the corrected result has the typical sawtooth shape [Fig. 3-9(b)]. The non-corrected OPL hence cannot be properly unwrapped, leading to a severely limited linear range [blue curve in Fig. 3-9(c)]. In contrast, the unwrapped result from the modified algorithm shows a much extended linear range [Fig. 3-9(d)]. This is critical for correctly quantifying samples with large OPL variation. We note that there are still periodic inflection points but the linear range is sufficiently large for most samples.

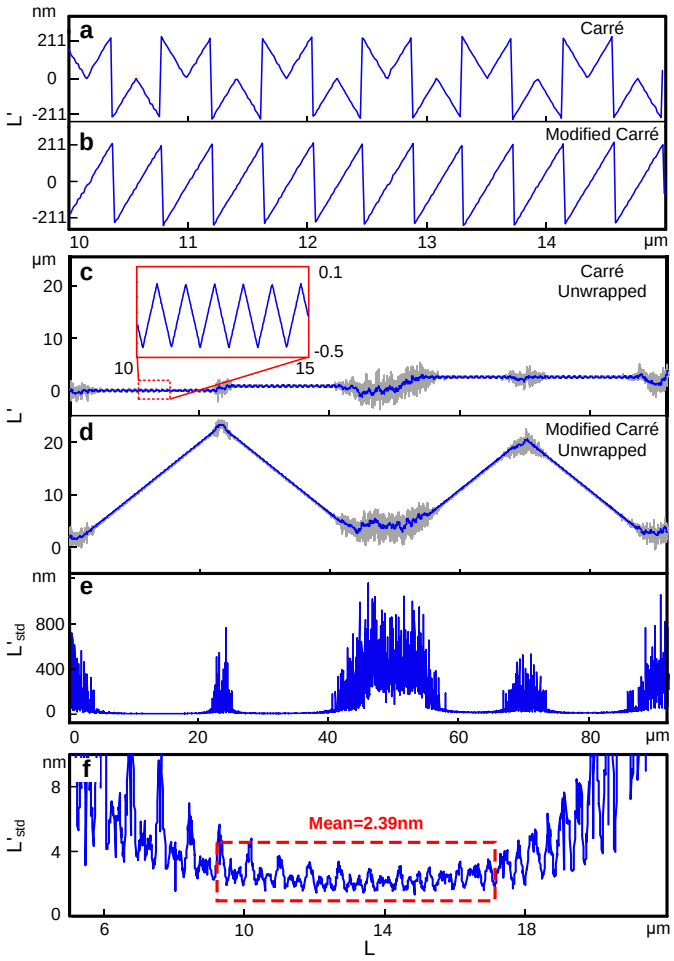

Fig. 3-9 LC-WSI simulation. Before unwrapping, OPL obtained by (a) original Carré equation and (b) our modified equation. Corresponding unwrapped OPL (c) without or (d) with this correction. (e) Dependence of measurement sensitivity on L. (f) Region of L for ideal operation.

Further, to better visualize noise performance of the unwrapped L', we repeat the demodulation 100 times with random noises and plot the results together as the shaded background in Figs. 3-9(c) and 3-9(d). It clearly shows that the demodulation error varies with L. Severe noise (error) is present around the inflection points. Hence it is necessary to determine the optimal range of L to be used in the interferometer. To this end, we calculate the standard deviation (sensitivity) of the 100 groups of demodulated L' [Fig. 3-9(e)]. Indeed, regions around the inflection points are orders of magnitude noisier. Additionally, the sensitivity becomes worse beyond the coherence length of a single band (~33 μm). We hence select the region between 9~17 μm as the optimal range for high-sensitivity OPL detection, with an average sensitivity of 2.39 nm [Fig. 3-9(f)]. We note that the optimal value of L (~14 μm) corresponds to a phase shift of 1.92 rad (ΔkL), which is consistent with previous report of the optimal shift for Carré algorithm in the context of PSI [18]. The

sensitivity performance of our system is limited by the relatively low saturation capacity of the camera, which affects signal-to-noise ratio. Larger saturation capacity would generate stronger signal and thus better sensitivity.

The ambiguity issue shown in Fig. 3-9(a) was due to the quadrant ambiguity of arctangent and was previously addressed by another approach [19,20]. Briefly, the wrapped phase $\phi = k_0 L$ was corrected with the addition or subtraction of π or 2π based on the signs of $\sin\phi$ and $\cos\phi$, which are inferred from the signs of the following intensity combinations:

$$I_2 - I_3 = 2b \sin\phi \cdot \sin\frac{\Delta\phi}{2},$$

$$I_2 + I_3 - (I_1 + I_4) = 2b \cos\phi \cdot \cos\frac{\Delta\phi}{2} \sin^2\frac{\Delta\phi}{2}. \tag{3-8}$$

In comparison, we add a simple $\mathrm{sgn}()$ term in Eq. (3-7) to achieve equivalent results. But Eq. (3-8) offers important insights into the cause of the inflection points in Fig. 3-9(d). When $\Delta\phi/2$ varies across $m\pi/2, m = 1,2,3...$, $\sin(\Delta\phi/2)$ or $\cos(\Delta\phi/2)$ in Eq. (3-8) will experience a change of sign, affecting the sign judgment for $\sin\phi$ and $\cos\phi$. These sign-inverting points correspond to $L = m\pi/\Delta k$, precisely where the inflection points are located in Fig. 3-9(d). Nevertheless, this effect does not affect the signal processing of our approach because our optimal linear range is within the first inflection point.

3.2.3.2 Sensitivity Characterization

We now characterize system sensitivity with a water-filled, blank sample chamber. Temporal measurement sensitivity is quantified by acquiring 100 consecutive OPL images of this sample and calculating the standard deviation for each image pixel. The average sensitivity across the FOV is 2.33 nm, in excellent agreement with the simulated result.

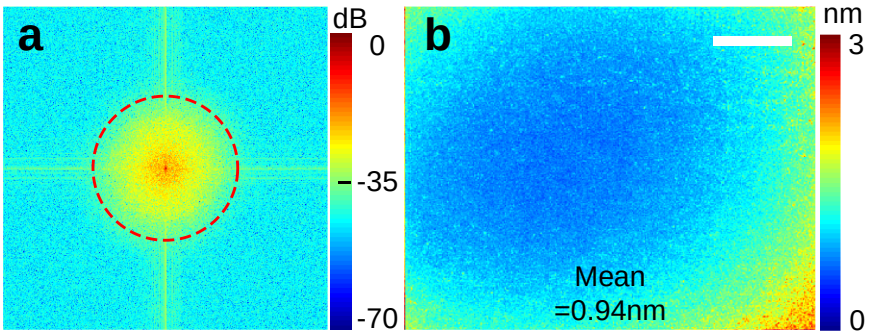

Fig. 3-10 (a) Spatial frequency component of lens tissue sample. Circle specifies the bandwidth of spatial lowpass filter. (b) Improved temporal OPL sensitivity after spatial filtering. Scale bar: 20 μm.

This sensitivity can be further improved by spatial filtering in Fourier domain to remove out-of-band noise since the camera oversamples the image. We determine the spatial-frequency passband by imaging a piece of lens tissue, whose fine structures fill the bandwidth. Fig. 3-10(a) shows the 2D Fourier transform of the image with the red circle indicating spatial filter boundary. After filtering, the mean value of the temporal sensitivity is improved to below 1 nm [Fig. 3-10(b)].

3.2.3.3 RBC Experiments

We demonstrate the feasibility of LC-WSI for quantitative phase imaging using human RBCs. A drop of whole blood is sandwiched by a No. 1.5 coverslip and a microscope slide and placed on the sample stage. As a first step, we need to ensure the OPL difference between the two arms is within the optimal range. This is achieved by taking advantage of the swept source: before the four-band experiments, we slowly sweep the laser and record interferograms at a large number of wavenumber positions and with narrow linewidth, as described in SS-DHPM. As shown in Fig. 3-11(a), the sample-reference interference varies with wavelength as expected. From the positions of the minima, the OPL difference can be determined as $2\pi/\left(k_{2\min}-k_{1\min}\right)$=13.58 μm, well within the optimal range. This verification step is a one-time procedure. Next, we switch the source and camera to four-band acquisition mode to capture LC-WSI interferograms [Figs. 3-11(b1-b4)]. The processed OPL images for RBCs are shown in Figs. 3-11(c) and (d).

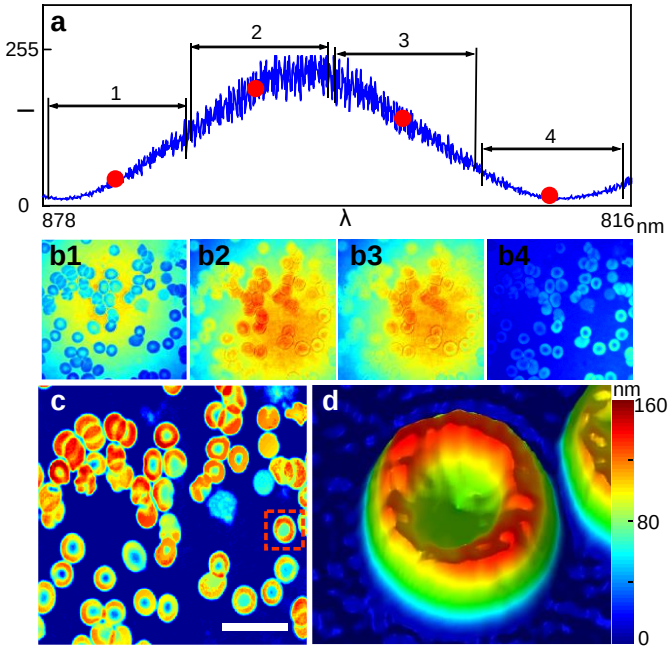

Fig. 3-11 (a) Spectral intensity across the full sweep range when using slow and narrow-linewidth scanning. The four bands and their center wavenumbers are marked. (b) Interferograms of RBCs. (c) OPL image. Scale bar: 20 μm. (d) 3D rendering of the RBC marked in (c).

3.2.3.4 Fast Dynamics: Dry Mass Monitoring

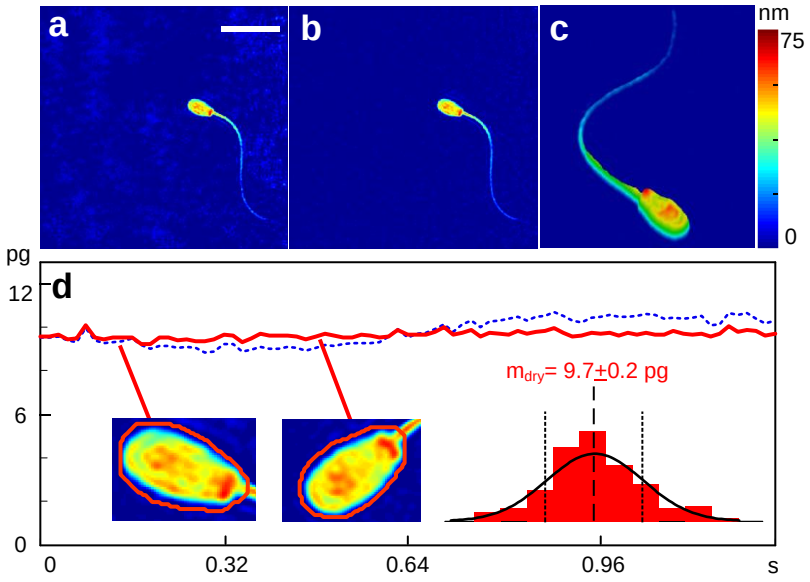

Fig. 3-12 OPL images of a boar sperm cell (a) before and (b) after fixed background pattern removal. Scale bar: 20 μm. (c) 3D representation. (d) Dry mass of the sperm head, before (blue dash) and after (red solid) background subtraction. (insets) contours of the masks on sperm head, and the histogram of the red curve.

With high acquisition rate and high sensitivity, the proposed system is capable of imaging dynamic biological specimens such as sperm cells. It has been reported that sperm morphology is highly correlated to its quality. For example, with intracytoplasmic morphologically selected sperm injection, the pregnancy rates of in vitro fertilization can be improved [21]. For our experiment, boar semen was collected, extended and diluted with sperm wash medium. The OPL image of a live and mobile sperm is shown in Fig. 3-12(a).

An application of OPL images is to calculate cell dry mass and/or volume [22,23]. The conversion between OPL values and the total dry mass of cell within an enclosed area s is:

$$m_{dry} = \oint_s \frac{L}{\chi} dS , \tag{3-9}$$

where $\chi \approx 0.18 cm^3/g$ is a conversion coefficient [24]. Since the sperm cell is in constant motion, the integral accuracy will be affected by the spatial variation of background, which is evident in Fig. 3-12(a). To remove this fixed pattern, temporal averaging of OPL over the entire recording is performed for each pixel, but excluding the moments when the pixel is occupied by the sperm cell. Since each pixel has such sperm-free periods due to the sperm's fast motion, an accurate background can be obtained and removed subsequently. Cleaner OPL image after the background removal is shown in Figs. 3-12(b) and (c).

Real-time dry mass is calculated with an automatic edge-detection based algorithm to generate mask for sperm head [Fig. 3-12(d)]. The dynamic dry mass curve after background correction shows considerably less variation than the uncorrected one. The mean value of 9.7 pg is generally in line with previous reports of boar as well as other species such as bull and ram [25]. Standard deviation of the dry mass curve is 0.2 pg, believed to be mainly due to mask inaccuracy. The $\pm 2\%$ full-scale error is fairly accurate, considering the motion of the cell and its small mass as compared to other cells types, such as HeLa cells that are typically several hundreds of picograms [22].

3.3 Non-evenly Spaced Wavelength Lasers or LEDs

The swept-source based system is more than sufficient for applications without the need for spectroscopy. Since in LC-WSI, the synchronization of the swept laser source and the long camera exposure is only designed to generate wider linewidth for low coherence illumination, an

alternative solution is replacing the source with superluminescent diodes (SLDs) or even multiple light emitting diodes (LEDs). For these low-cost sources, challenges arise since conditions to use Carré algorithm introduced in Section 3.2.2 may not be satisfied. For example, the spectral bands of LEDs may not be evenly spaced, and the spectral response cannot be assumed symmetric. Or simply, we may only have intensities at three wavelengths. Under such circumstances, a numerical solver may be a practical way since the nature of the problem becomes an optimization problem which can be defined as:

$$\{a,b,L\} = \arg\min \sum_{n=1}^{3} \left\{ I_n - a - b\left|\gamma_n\right| \cos\left[k_n L + \xi_n\right) \right\}^2 \tag{3-10}$$

The Fourier transform of the spectral shape, $\left|\gamma_n(L)\right| e^{j\xi_n(L)}$, can be experimentally characterized prior to formal measurements and interpolated to a better solution, as shown in Fig. 3-13. The amplitude and phase response values can be stored in advance for a lookup table method that will speed up the signal processing speed. To solve the nonlinear least square optimization in Eq. (3-10), a trust region reflective algorithm and a multistart searching strategy can be used. More discussions of the nonlinear optimization for a similar but more complicated case for WSI will be detailed in Section 3.4.3.

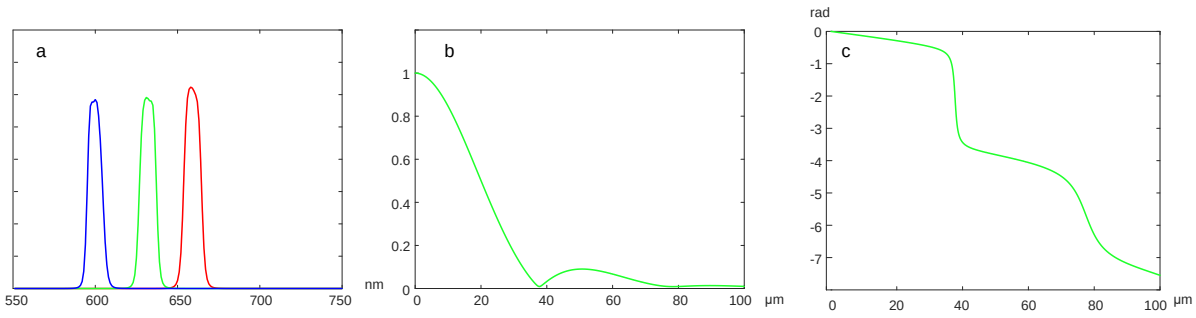

Fig. 3-13 (a) The measured light source spectra (center wavelength at 660/633/600nm), and (b) amplitude and (c) phase of the self-coherence function in terms of OPL for the 633nm spectrum.

3.4 Common Path Configuration

In previous sections, a Mach-Zehnder interferometer is used, in which the sample arm and reference arm are separate. Such a configuration can see the noises from the environment when

they affect the two arms differently. In contrast, a common path configuration wherein the sample and reference field share an almost identical optical path is more preferred in a variety of applications for its capability to reduce the environmental noises [26-29]. Moreover, many existing phase contrast microscope (non-quantitative ones) utilize the common path configuration. Therefore, it will be promising if WSI can be implemented with a common path configuration to fully exploit its strengths in simplicity, low-cost and multimode compatibility. This generates new challenges in signal modeling and demodulation compared to traditional two-arm interference.

3.4.1 System Schematic and Signals

The diagram in Fig. 3-14 shows the optical train of a typical transmission based commercial phase contrast microscope. The goal is by reusing or replacing/adding some components in this platform, we can convert the qualitative phase contrast microscope to a quantitative one with minimum cost. There are two sets of conjugate planes: i) the aperture plane and the exit pupil of the objective; ii) sample plane and image plane. Light from the actual source (not drawn in the figure) is delivered onto the aperture plane and is regulated by the aperture stop (diaphragm). After the light pass through the sample, a portion of the light is scattered and exhibits angular divergence. A matching phase plate is usually placed at the objective exit pupil to generate the optical pathlength delay between the scattered and unscattered fields so that phase contrast is encoded in the interferogram on image plane.

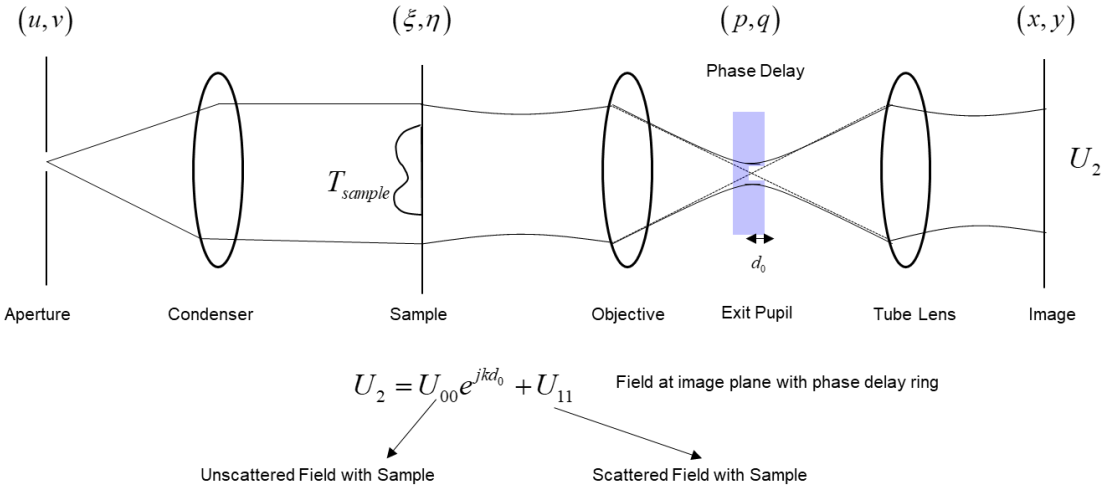

Fig. 3-14 Diagram of common path phase contrast microscope and the pinhole aperture with matched phase ring case.

A pinhole aperture is the simplest geometry selection on the aperture plane. Correspondingly, on the exit pupil (or its conjugate plane) of the objective, a phase delay plate with a center pinhole pit is used. Ideally, the pinhole should have an infinitely small radius such that its amplitude transmittance can be characterized by a delta function. However, even for a finite size pinhole, if the coherence area on the aperture plane is much larger than the pinhole size, then the delta function is still a valid approximation. More importantly, this corresponds to a fully spatial coherent case and thus the system is linear in terms of field instead of intensity [30]. This largely simplifies the signal model and an explicit demodulation formula is available.

The interference intensity on the image plane is given by:

$$I = \left|U_{00}e^{jkd_0} + U_{11}\right|^2 = \left|U_{00}\right|^2 + \left|U_{11}\right|^2 + 2\left|U_{00}\right|\left|U_{11}\right|\cos\left(\angle U_{11} - \angle U_{00} + kd_0\right). \tag{3-11}$$

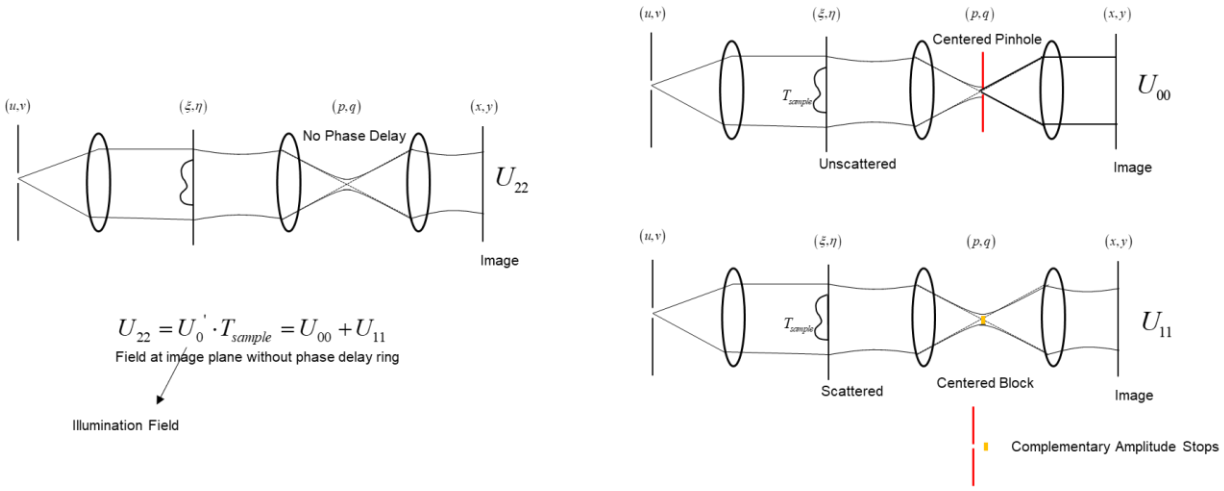

Fig. 3-15 Field decomposition. Without phase delay plate at exit pupil, the total field (left column) is an image of the sample and is a multiplication of the illumination field and the sample's transmittance. It can also be decomposed to a summation of the unscattered and scattered fields (right column) where complementary amplitude stops are used.

Definitions of terms U_{00} and U_{11} require decomposition of the image field without the phase delay plate, which can be seen in Fig. 3-15. Both cases involve the usage of amplitude stops instead of phase delay plate at the objective exit pupil to fully separate unscattered and scattered components. U_{00} is the image field when inserting a amplitude stop with a matching opening as the aperture stop, and U_{11} is the image field when inserting a complementary amplitude stop, i.e., light can pass everywhere through the exit pupil except the matched part with the aperture stop. The summation

of U_{00} and U_{11} corresponds to the case where there is nothing at the exit pupil, and it is slightly different compared to the traditional system where the illumination and the transmittance of the sample are multiplied.

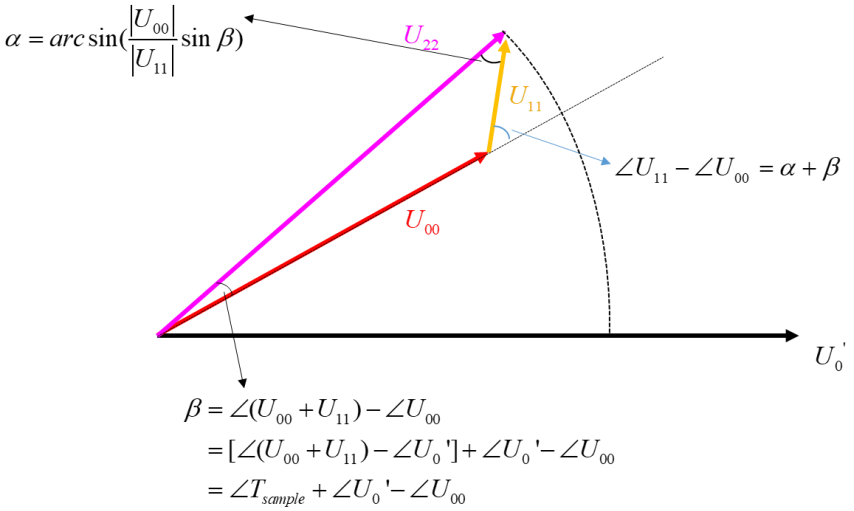

Fig. 3-16 Complex phasors plotted as vector forms.

To better understand the decomposition, we can plot the complex phasor as vectors in Fig. 3-16.

Figure 3-16 also enables Eq. (4-1) to be further derived as:

$$\begin{aligned} I &= |U_{00}|^2 + |U_{11}|^2 + 2|U_{00}||U_{11}|\cos\left(\angle U_{11} - \angle U_{00} + kd_0\right) \\ &= |U_{00}|^2 + |U_{11}|^2 + 2|U_{00}||U_{11}|\cos(\alpha + \beta + kd_0) \\ &= |U_{00}|^2 + |U_{11}|^2 + 2|U_{00}||U_{11}|\cos[\beta + kd_0 + arc\sin(\frac{\sin\beta}{|U_{11}|}|U_{00}|)] \end{aligned} \tag{3-12}$$

with $\beta = kL(x,y) + (\angle U_0' - \angle U_{00})$. The arcsin() term in Eq. (3-12) indicates I vs. β does not strictly follows a sinusoidal relation, but with a slight distortion. It also indicates the usually defined visibility term, $V = |U_{11}|/|U_{00}|$ must satisfy $\left|(\sin\beta)/V\right| \le 1$. Therefore L will affect visibility and in some cases V will be larger than 1. In a pinhole aperture case, it is also straightforward that the phase of illumination field, $\angle U_0'$, is uniform across all pixels. Therefore it can be removed from the definition of β.

It is worth mentioning that in Fourier Phase Microscopy (FPM) [26], $\alpha+\beta=\angle U_{11}-\angle U_{00}$ is firstly solved and then β is calculated. For WSI, however, a signal form explicitly in terms of L (or β) is needed because $\alpha+\beta=\angle U_{11}-\angle U_{00}$ is not a constant for different wavelength, which will be shown later in signal demodulation section.

3.4.2 Numerical Wave Propagation Method

Numerical wave propagation is a powerful tool to simulate an optical system. The purpose here is to validate the previously derived signal model and preparing for simulating artificial samples for demodulation later.

For fully coherent wave, wherein the centered pinhole aperture case lies, the propagation of electromagnetic field is well described in Fourier optics [31]. A system shown in Fig. 3-14 can be treated as three cascading sub-systems. They are: i). sub-system from the aperture plane to the sample plane; ii). sub-system from the sample plane to the exit pupil; iii). sub-system from the exit pupil to the microscope image plane. In each sub-system, a thin lens is assumed and paraxial approximation and Fraunhofer propagation are used. As a result, a scaled version of Fourier Transform can be used to connect the field at back focal plane to the input at the front focal plane:

$$U_f(\xi,\eta)=\sum_u\sum_v U_i(u,v)e^{-j\frac{2\pi}{\lambda f}(u\xi+v\eta)}dudv \tag{3-13}$$

By defining an input field at the pinhole aperture, which is a delta function $\delta(u,v)$, it is straightforward to propagate this field in different sub-system and multiply with the complex transmittance of sample or phase plate when needed. Not only it can simulate the interference fields U_2 but it can also simulates different components U_{00} and U_{11} by supplying amplitude stops at exit pupil plane, providing convenience to examine the contribution from unscattered and scattered fields respectively.

3.4.3 Demodulation

The purpose for wavelength shifting interferometry is to obtain the sample phase/optical pathlength from interferograms taken at different wavelength, whose signals are expressed as:

$$I_n = \left|U_{00,n}\right|^2 + \left|U_{11,n}\right|^2 + 2\left|U_{00,n}\right|\left|U_{11,n}\right|\cos[k_n(L+d_0) - \angle U_{00,n} + arc\sin(\frac{\sin(k_n L - \angle U_{00,n})}{\left|U_{11,n}\right|}\left|U_{00,n}\right|)] \tag{3-14}$$

If $\left|U_{00,n}\right|$, $\left|U_{11,n}\right|$ and $L_{00,n} = \angle U_{00,n}/k_n$ can be assumed to be independent of wavenumber k , then the demodulation will be equivalent to solving a nonlinear optimization problem:

$$\{\left|U_{00}\right|, \left|U_{11}\right|, L - L_{00}\} =$$
$$\arg\min \sum_{n=1}^{3}\left\{ I_n - \left|U_{00}\right|^2 - \left|U_{11}\right|^2 - 2\left|U_{00}\right|\left|U_{11}\right|\cos\left[k_n(L - L_{00} + d_0) + arc\sin(\frac{\sin[k_n(L-L_{00})]}{x_2}) \right] \right\}^2 \tag{3-15}$$

Unlike phase shifting interferometry in which d_{0n} are equally spaced apart by $\pi/2$ so that a simple 4-step method can be employed to demodulate[26], the wavenumber variation and sample OPL are coupled in WSI and is further complicated by the arcsin() operator. At a first glance we can still demodulate $\angle U_{11} - \angle U_{00} = \alpha + \beta$ first and then retrieve the true phase. However, $\alpha + \beta$ will naturally be different for different wavenumber k_n . Therefore, a numerical solution is practical.

In Fig. 3-17 the performance of the least square numerical solver is demonstrated. We firstly generate the intensities at variable L ranging across almost 1.5μm. Shot noise is also simulated for the intensities at each L to mimic the realistic performance. We then solve Eq. (3-15) in MATLAB® with Interior Point trust region algorithm [32]. This is a relatively broad OPL range in QPI and it is sufficient for most of the biological samples. As a consequence, a multistart strategy for picking initial search points is adopted and guaranteed to select the global minimum instead of local minimum. We also apply nonlinear constraint $\left|\sin[k_n(L-L_{00})]\cdot\left|U_{00}\right|/\left|U_{11}\right|\right| \le 1$ so that it can remove unnecessary searches. Due to this constraint, it is not possible to use a regular *lsqnonlin* solver in MATLAB. Instead, a *fmincon* solver is used. To better speed up the convergence and improve accuracy, the gradient formulae for both cost function and nonlinear constraint are also derived and supplied.

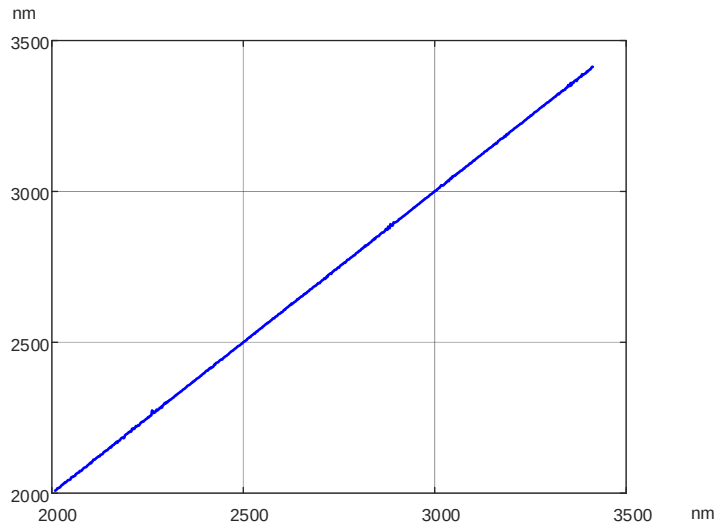

Fig. 3-17 Solving L with nonlinear optimization in a broad range.

The assumption that $\left|U_{00,n}\right|$, $\left|U_{11,n}\right|$ and $L_{00,n}=\angle U_{00,n}/k_n$ can be assumed to be non-dependent on wavenumber k does not always hold. In fact, it is most suitable for sparsely distributed sample, which has many zero OPLs in the field of view. Since we have covered the Fourier transform based wave propagation in the previous section, it is easy to explain this by analyzing what is causing the change for different wavelength. Taking the $U_{00,n}(x,y)$ term for example, it can be expressed as:

$$
\begin{aligned}
U_{00,n} &= \mathbb{F}\left\{\mathbb{F}\left\{T_{sample,n}\right\}\cdot\delta(p,q)\right\} = \mathbb{F}\left\{\mathbb{F}\left\{T_{sample,n}\right\}\Big|_{p=0,q=0}\cdot\delta(p,q)\right\} = \mathbb{F}\left\{\left[\sum_{\xi}\sum_{\eta}T_{sample,n}\right]\cdot\delta(p,q)\right\} \\
&\approx \mathbb{F}\left\{\left[\sum_{\xi}\sum_{\eta}e^{j(k_1+\Delta k_n)L(\xi,\eta)}\right]\cdot\delta(p,q)\right\} = \left[\sum_{\xi}\sum_{\eta}e^{j(k_1+\Delta k_n)L(\xi,\eta)}\right]\mathbb{F}\left\{\delta(p,q)\right\} \\
&= \sum_{\xi}\sum_{\eta}e^{j(k_1+\Delta k_n)L(\xi,\eta)} \equiv r_{n1}\left|U_{00,1}\right|e^{j\angle U_{00,n}} \\
&\rightarrow r_{n1} = \left|\sum_{\xi}\sum_{\eta}e^{j(k_1+\Delta k_n)L(\xi,\eta)}\right| \Big/ \left|U_{00,1}\right|, \angle U_{00,n} = \angle\left\{\sum_{\xi}\sum_{\eta}e^{j(k_1+\Delta k_n)L(\xi,\eta)}\right\}
\end{aligned}
\tag{3-16}
$$

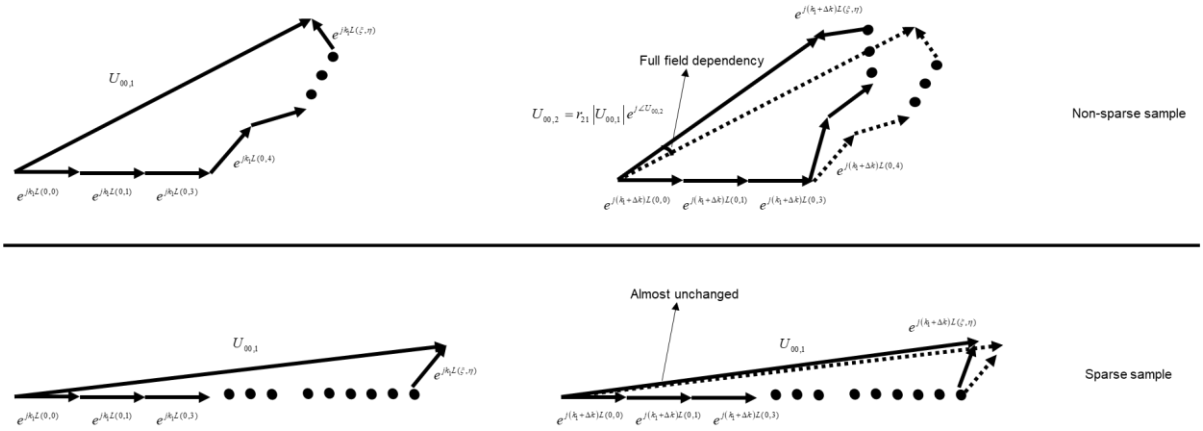

Fig. 3-18 $U_{00,n}$ as a summation of field vectors with amplitude of 1 and non-uniform OPL distribution. At different wavenumber, the phase shift for each term in summation, $\Delta kL(\xi,\eta)$, is different, except for the terms with $L(\xi,\eta)=0$. Hence the total field's phase shift depends on the full field information. Only sparse sample with many zero $L(\xi,\eta)$ will behave largely independent of wavenumber.

The approximation in second line is made for thin sample in QPI that exhibits weak absorbance or scattering. For different wavenumber, the added wavenumber Δk_n will induce an extra phase change for each term in the summation and in turn affect the total field. The vector plot in Fig. 3-18 describes this behavior. For sparsely distributed sample that sees a lot of zero $L(\xi,\eta)$, the effect of wavenumber change is largely minimized (because of a large number of unit vectors pointing towards east). The same analysis can be done on another component:

$$\begin{aligned} &U_{11,n}(x,y)=\mathbb{F}\left\{\mathbb{F}\left\{T_{sample,n}\right\}\cdot[1-\delta(p,q)]\right\}=T_{sample,n}(x,y)-U_{00,n}\\ &=e^{jk_nL(x,y)}-\left|U_{00,1}\right|e^{j\angle U_{00,n}}\equiv\left|U_{11,1}(x,y)\right|s_{n1}e^{j\angle U_{11,n}}\\ &\rightarrow s_{n1}(x,y)=\left|e^{jk_nL(x,y)}-\left|U_{00,1}\right|e^{j\angle U_{00,n}}\right|\Big/\left|U_{11,1}\right|,\angle U_{11,n}(x,y)=\angle\left\{e^{jk_nL(x,y)}-\left|U_{00,1}\right|e^{j\angle U_{00,n}}\right\} \end{aligned} \quad . \text{(3-17)}$$

The last lines of both Eqs. (3-16) and (3-17) show that for a phase sample in QPI, OPL L can be used to estimate the ratio between $\left|U_{00,n}\right|$ and $\left|U_{11,n}\right|$. It is worth noting that this estimation has to rely on the full field information and therefore is implicit in the intensity formula. For non-sparsely distributed sample when we cannot ignore these ratios, we can formulate the problem still as solving three unknowns but we cannot demodulate on a pixel basis. Nevertheless, this will add to a lot of difficulties to the nonlinear optimization. Instead, we can solve the problem using an iterative searching approach based on the following intensity formulae:

$$I_n = \left|U_{00,1}\cdot r_{n1}\right|^2 + \left|U_{11,1}\cdot s_{n1}\right|^2$$
$$+2r_{n1}s_{n1}\left|U_{00,1}\right|\left|U_{11,1}\right|\cos[k_n(L+d_0) - \angle U_{00,n} + arc\sin(\frac{\sin(k_nL - \angle U_{00,n})}{U_{11,1}s_{n1}}U_{00,1}r_{n1})]\cdot \tag{3-18}$$

The specific steps for a full demodulation are described below:

Step 1. Demodulate an approximate L_{ap1} with $r_{n1} = s_{n1} = 1$ (so that $\left|U_{00}\right|$ and $\left|U_{11}\right|$ do not depend on wavelength) and $\angle U_{00,n} = 0$ (In fact, any constant for $\angle U_{00,n} / k_n$ is acceptable, and it is straightforward to prove they are equivalent in terms of obtaining a relative OPL).

Step 2. From L_{ap1}, updates r_{21}, r_{31}, and $\angle U_{00,n}$ from the last line of Eq. (3-16). If necessary, a background subtraction can be done beforehand to make background pixels have zero OPL (it can be easily proved a constant OPL shift for every pixel will not affect the demodulation of L). The reason for updating U_{00} terms first is because most of the energy falls within the pinhole (unscattered). Besides, $\angle U_{00,n}$ is uniform across the field of view, making the approximation easier and robust.

Step 3. Let $s_{21} = 1$, $s_{31} = 1$ and plug in other updated parameters in *Step* 2 in intensity formula and re-demodulate L_{AP2} .

Step 4. Update r_{21}, r_{31}, s_{21}, s_{31} and $\angle U_{00,n}$ with the last lines of Eq. (3-16) and Eq. (3-17). This is a finer estimation taking the U_{11} terms for consideration. Demodulate again to retrieve L_{Final}.

Step 5. Examine $\left|U_{00,1}\right|$ from demodulation in *Step* 4. If it is a constant (or within an acceptable error) for all pixels, stop. Otherwise, repeat *Steps* 2~5 until satisfied.

This iterative searching method closes the gap between the demodulated OPL and the ground truth step by step. The idea behind it is utilizing the full field OPL distribution in the rough estimation stage to perform a finer adjustment. This is in significant contrast to a pixel-by-pixel demodulation in Mach-Zehnder based WSI and is necessary due to the common path nature. Phase sample assumption and the pinhole configuration also largely simplifies the calculation.

Experimentally, we can also measure $\left|U_{00,n}\right|$ and $\left|U_{11,n}\right|$ by fabricating amplitude plate as depicted in Fig. 3-15. Although this will increase the number of shots needed, it can significantly reduce the computational burden on numerical solver because we are only left with one unknown L to solve and one angle term $\angle U_{00}$ to iteratively estimate.

3.4.4 Simulated Samples and Results

In this section, the numerical wave propagation method described in Section 3.4.2 is used to simulate human red blood cells' interferograms I_1 , I_2 , I_3 at three wavelength $\lambda = \{660nm, 633nm, 600nm\}$. The OPL of the RBCs were obtained in experiment with the Mach-Zehnder type WSI in Section 3.2, as shown in Fig. 3-19.

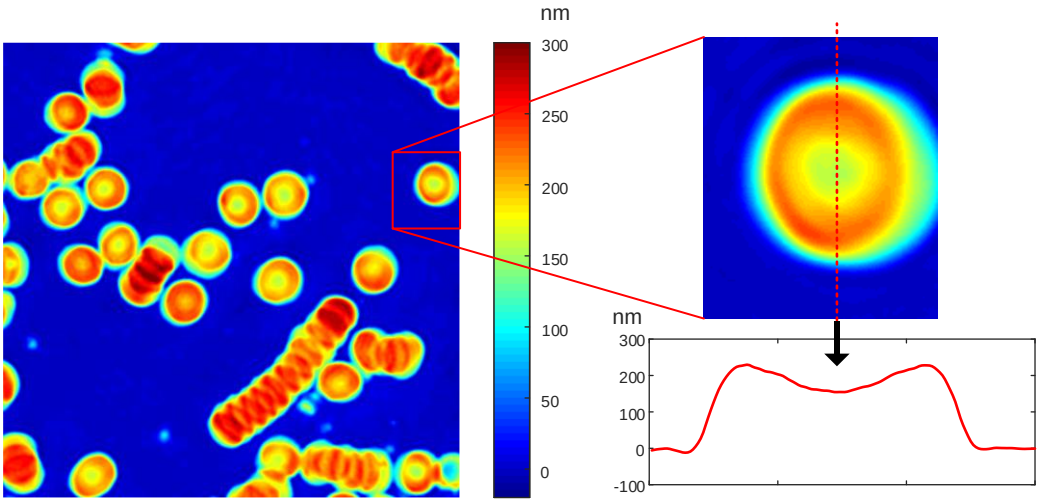

Fig. 3-19 Ground truth OPL of simulated RBCs on sample plane. (inset) zoom-in of a single RBC and its profile along the marked position.

In the context of QPI, the sample is assumed to have unit amplitude response. The intensities are normalized to $[0, 255]$ range, which is typically the readout in an 8-bit camera. The pit at center of the phase plate has $d_0 = 350nm$ OPL difference compared to the neighborhood area. At these three different wavelength, the simulated intensities are shown as below:

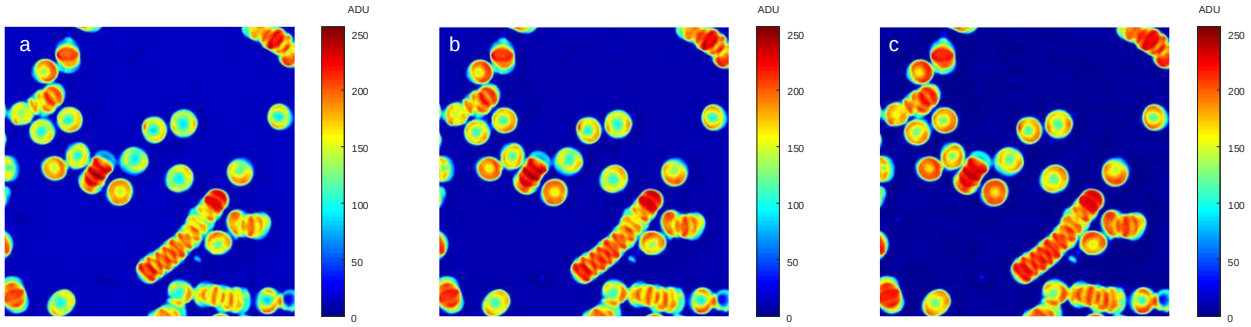

Fig. 3-20 Simulated interferograms at (a) 660nm, (b) 633nm and (c) 600nm.

The normalized magnitudes of unscattered and scattered components, $|U_{00}|$, $|U_{11}|$, as well as their ratio, which is defined as visibility $V = |U_{11}|/|U_{00}|$,are shown as below for different wavelengths:

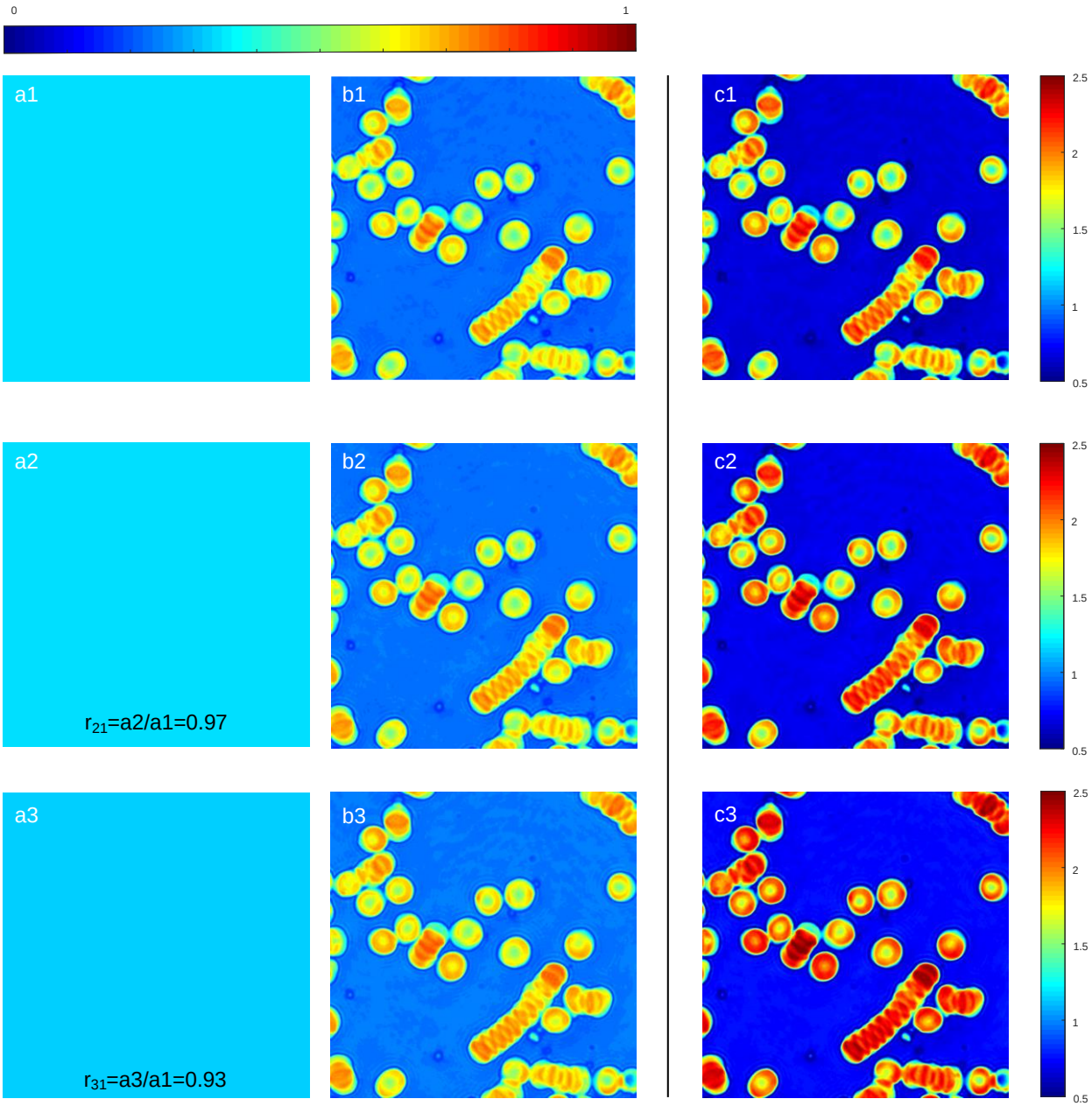

Fig. 3-21 (a)$|U_{00}|$, (b)$|U_{11}|$, and (c) visibility $V=|U_{11}|/|U_{00}|$ for 660nm (1st row), 633nm (2nd row) and 600nm(3rd row). r_{21} and r_{31} are the ratios of $|U_{00}|$ at different wavelength defined in details in section 3.4.3.

For demodulation, the steps in the previous section are followed and a good agreement compared to ground truth is shown:

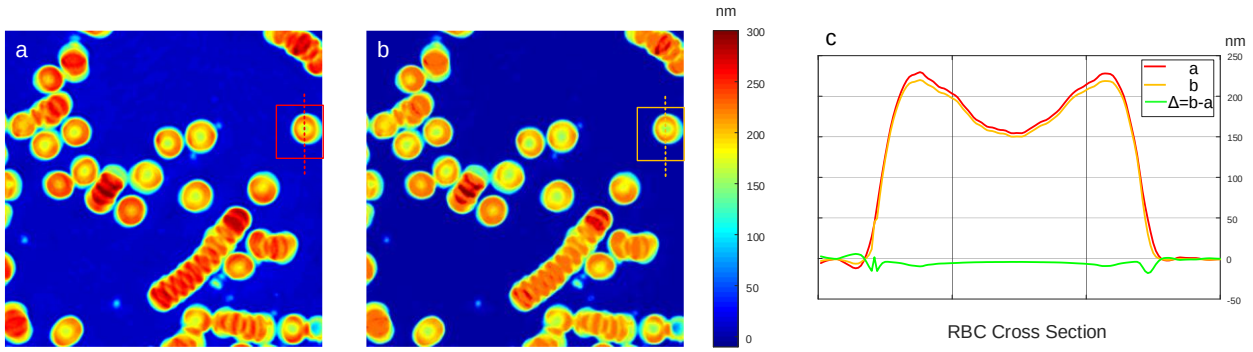

Fig. 3-22 Demodulation results. (a) The ground truth and (b) the demodulated OPL. (c) Line profiles of the marked positions in (a) and (b), and their difference.

References

[1] T. Slabý, P. Kolman, Z. k. Dostál, M. Antos, M. Losták, and R. Chmelík, "Off-axis setup taking full advantage of incoherent illumination in coherence-controlled holographic microscope", Optics Express **21**, 14747 (2013).

[2] S. Tamano, Y. Hayasaki, and N. Nishida, "Phase-shifting digital holography with a low-coherence light source for reconstruction of a digital relief object hidden behind a light-scattering medium", Applied Optics **45**, 953-959 (2006).

[3] M. Rinehart, Y. Zhu, and A. Wax, "Quantitative phase spectroscopy", Biomedical Optics Express **3**, 958 (2012).

[4] F. Shen and A. Wang, "Frequency-estimation-based signal-processing algorithm for white-light optical fiber Fabry–Perot interferometers", Applied Optics **44**, 5206-5214 (2005).

[5] M. A. Choma, A. K. Ellerbee, C. H. Yang, T. L. Creazzo, and J. A. Izatt, "Spectral domain phase microscopy", Optics Letters **30**, 1162 (2005).

[6] C. Li and Y. Zhu, "Quantitative polarized light microscopy using spectral multiplexing interferometry," Opt. Lett. **40**, 2622-2625 (2015).

[7] B. Bartoov, A. Berkovitz, F. Eltes, A. Kogosovsky, A. Yagoda, H. Lederman, and Y. Barak, "Pregnancy rates are higher with intracytoplasmic morphologically selected sperm injection than with conventional intracytoplasmic injection", Fertility and Sterility **80**, 1413-1419 (2003).

[8] G. Di Caprio, M. A. Ferrara, L. Miccio, F. Merola, P. Memmolo, P. Ferraro, and G. Coppola, "Holographic imaging of unlabelled sperm cells for semen analysis: a review," Journal of Biophotonics **8**, 779-789 (2015).

[9] F. Dubois, L. Joannes, and J. Legros, "Improved three-dimensional imaging with a digital holography microscope with a source of partial spatial coherence", Applied Optics **38**, 7085-7094 (1999).

[10] V. Micó, J. Garcia, and Z. Zalevsky, "Quantitative phase imaging by common-path interferometric microscopy: application to super-resolved imaging and nanophotonics", Journal of Nanophotonics **3**, 031780 (2009).

[11] M. Haifler, P. Girshovitz, G. Band, G. Dardikman, I. Madjar, and N. Shaked, "Interferometric phase microscopy for label-free morphological evaluation of sperm cells", Fertility and Sterility **104**, 43-47 (2015).

[12] F. E. Robles, L. L. Satterwhite, and A. Wax, "Nonlinear phase dispersion spectroscopy", Optics Letters **36**, 4665 (2011).

[13] R. Shang, S. Chen, C. Li, and Y. Zhu, "Spectral modulation interferometry for quantitative phase imaging", Biomedical Optics Express **6**, 473-479 (2015).

[14] I. H. Malitson, "Interspecimen Comparison of the Refractive Index of Fused Silica" Journal Optical Society of America **55**, 1205-1209 (1965).

[15] X. Xu, and R. K. Wang, "Synergistic effect of hyperosmotic agents of dimethyl sulfoxide and glycerol on optical clearing of gastric tissue studied with near infrared spectroscopy", Physics in Medicine and Biology **49**, 3 (2004).

[16] E. Wolf, "New theory of partial coherence in the space–frequency domain. Part I: spectra and cross spectra of steady-state sources," Journal of Optical Society of America **72**, 343-351 (1982).

[17] P. A. A. M. Junior, P. S. Neto, and C. S. Barcellos, "Generalization of Carré equation," Optik-International Journal for Light and Electron Optics **122**, 475-489 (2011).

[18] K. Qian, F. Shu and X. Wu, “Determination of the best phase step of the Carré algorithm in phase shifting interferometry,” Measurement Science and Technology **11**, 1220 (2000).

[19] K. Creath, "Phase-shifting speckle interferometry," Applied Optics **24**, 3053-3058 (1985).

[20] K. Creath, “Phase-measurement interferometry techniques,” Progress in Optics, **26**, 349-393 (1988).

[21] B. Bartoov, A. Berkovitz, F. Eltes, A. Kogosovsky, A. Yagoda, H. Lederman, and Y. Barak, “Pregnancy rates are higher with intracytoplasmic morphologically selected sperm injection than with conventional intracytoplasmic injection,” Fertility and Sterility **80**, 1413-1419 (2003).

[22] G. Popescu, Y. Park, N. Lue, C. Best-Popescu, L. Deflores, R. R. Dasari, M. S. Feld, and K. Badizadegan, “Optical imaging of cell mass and growth dynamics,” The American Journal of Physiology-Cell Physiology **295**, C538–C544 (2008).

[23] M. A. Ferrara, G. Di Caprio, S. Managò, A. De Angelis, L. Sirleto, G. Coppola, and A. C. De Luca, “Label-free imaging and biochemical characterization of bovine sperm cells,” Biosensors, **5**, 141-157 (2015).

[24] H. G. Davies, M. H. F. Wilkins, J. Chayen, and L. F. La Cour, “The use of the interference microscope to determine dry mass in living cells and as a quantitative cytochemical method,” Journal of Cell Science **3**, 271-304 (1954).

[25] G. F. Bahr, and E. Zeitler, “Study of bull spermatozoa: quantitative electron microscopy,” Journal of Cell Biology **21**, 175-189 (1964).

[26] G. Popescu, L. P. Deflores, J. C. Vaughan, K. Badizadegan, H. Iwai, R. R. Dasari, and M. S. Feld, "Fourier phase microscopy for investigation of biological structures and dynamics," Optics letters **29**, 2503-2505 (2004).

[27] G. Popescu, T. Ikeda, R. R. Dasari, and M. S. Feld, “Diffraction phase microscopy for quantifying cell structure and dynamics,” Optics Letters, **31**, 775-777 (2006).

[28] C. Joo, T. Akkin, B. Cense, B. H. Park, and J. F. de Boer, "Spectral-domain optical coherence phase microscopy for quantitative phase-contrast imaging," Optics Letters **30**, 2131-2133 (2005).

[29] C. Zheng, R. Zhou, C. Kuang, G. Zhao, Z. Zhang, and X. Liu. "Diffraction phase microscopy realized with an automatic digital pinhole," Optics Communications **404**, 5-10 (2017).

[30] J. W. Goodman, *Statistical optics*, John Wiley & Sons (1984).

[31] J. W. Goodman, *Introduction to Fourier optics*, Roberts and Company Publishers (2005).

[32] R. H. Byrd, J. C. Gilbert, and J. Nocedal, "A trust region method based on interior point techniques for nonlinear programming," Mathematical programming **89**, 149-185 (2000).

Chapter 4 Sensitivity Evaluation

To fulfill the demanding requirement for cell imaging applications, constant efforts have been made to push the limit of optical pathlength (OPL) sensitivity of quantitative phase imaging (QPI) to deep sub-nanometer level [1-4]. These advances can be attributed to the increase in signal to noise ratio (SNR) by means of high well capacity cameras, spatial or temporal filtering, and suppression of instrumental and environmental instabilities [5,6]. Meanwhile, in order to investigate the fundamental sensitivity that can possibly be achieved, Cramér–Rao Bound (CRB) and statistical analysis have been introduced [7-10].

To date, however, an accurate, systematic and practical method for sensitivity evaluation is still lacking. All current CRB analyses are based on uniform Gaussian noise assumption, while modern cameras and detectors almost always operate in shot noise-limited regime. A Gaussian model requires experimental characterization of detection noises that are independent of signal strength. In contrast, shot noise can be determined by signal strength alone. As a result, a practical solution to estimating the theoretical sensitivity directly from measurement data has not yet been reported. Meanwhile, comparing experimental sensitivity directly against CRB overlooks the impact of signal processing algorithms. It is then difficult to determine whether the gap between CRB and experimental sensitivity results from poor hardware operation, or from the choice of algorithm. A clear evaluation methodology is thus needed to evaluate system performance, guide system optimization, and facilitate system comparison.

4.1 Evaluation Framework

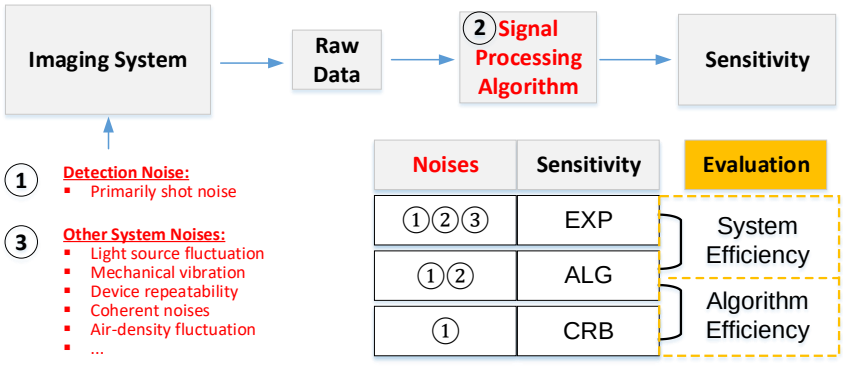

Fig. 4-1 Relations between CRB, ALG and EXP in the framework.

In this chapter, we propose a new framework of sensitivity evaluation for QPI. This framework is organized as a three-level structure which involves the CRB, algorithmic sensitivity (ALG) and experimental sensitivity (EXP). Their relationships are summarized in Fig. 4-1 and explained as follows. In all QPI systems, raw data is collected by the imaging system and then processed by a certain algorithm to retrieve OPL. Repeating this process for a number of times and calculating the standard deviation of OPL, we obtain the sensitivity, whose magnitude can be influenced by three factors: (i) detection noises, which are unavoidable noises of the detector, such as shot noise, dark noise, and read noise. Modern QPI detection is mostly shot noise-limited, rendering this category independent of system hardware; (ii) the signal processing algorithm; and (iii) other extrinsic system noises, which may be avoided or suppressed, including instrumental and environmental instabilities. The case where only (i) exists or dominates in the system corresponds to the case of CRB, which sets a lower limit on the variance of any unbiased OPL estimator. When (i) and (ii) are both considered, the sensitivity is the ALG. When all three factors are present, the sensitivity is the EXP. In terms of their magnitudes, we have $\sigma_{EXP} \geq \sigma_{ALG} \geq \sigma_{CRB}$. As a result, we can inspect the ratio of CRB to ALG as a measure of the efficiency of the algorithm ($\eta_{ALG} = \sigma_{CRB}/\sigma_{ALG}$), and examine the ratio between ALG and EXP to study system hardware efficiency ($\eta_{SYS} = \sigma_{ALG}/\sigma_{EXP}$).

4.2 A Study of Wavelength Shifting Interferometry

To demonstrate the use of this quantitative evaluation framework, we study wavelength shifting interferometry (WSI) as an example in the following discussion. WSI is a category of full-field QPI techniques that generate phase steps by shifting wavelength and retrieving OPL from multiple frames of spectral intensity. Two techniques based on WSI have been proposed in Chapter 3.

4.2.1 Signal Model

As the first step, the general expression of shot noise-limited CRB is derived. The OPL retrieval process in WSI is modeled as a parameter estimation problem. Let $\mathbf{x} = [x_1, ..., x_N]$ be the electrons collected at different wavelengths by a certain pixel of the camera. Each element x_n is a noise-corrupted random variable. For shot noise-limited case, we have $E(x_n) = Var(x_n) = s_n$ with s_n being the average photo-generated electrons for the n-th wavelength. In cameras, the photo-

generated electrons are converted to the digital intensity readout in analog-to-digital unit (ADU) with a conversion gain g being the number of electrons per ADU. We then have $I_n = x_n/g$ and $\overline{I_n} = s_n/g$ to represent the real (noise-corrupted) and average (noise-free) intensity readout in ADU, respectively. For both high- and low-coherence WSI techniques [11-13], the mean interference signals for the n-th wavenumber can be expressed as follows:

$$\overline{I_n} = \alpha + \beta\cos\left(k_n L\right), \quad n = 1 \sim N, \tag{4-1}$$

where α and β are magnitude constants independent of *n*, *L* is the OPL difference between the two arms, k_n is the n-th wavenumber. It is also common to use a ratio $V = \beta/\alpha$ to specify the spectrum visibility. Let $\boldsymbol{\lambda} = [\lambda_1, \lambda_2, \lambda_3] = [\alpha, \beta, L]$ denote the unknown parameters to be estimated from $\mathbf{x}$. For QPI, we focus on the statistical properties of L.

4.2.2 CRB and Algorithm Sensitivity Calculations

To calculate CRB, a general procedure is to find the likelihood function, compute the Fisher information matrix and then take the element of interest in the inverse of the matrix. Since each x_n is a Poisson random variable, the likelihood function of an observed $\mathbf{x}$ is:

$$p\left(\mathbf{x};\boldsymbol{\lambda}\right) = \prod_{n=1}^{N} Po(x_n; s_n) = \prod_{n=1}^{N} \frac{s_n^{\,x_n}}{x_n!} e^{-s_n}. \tag{4-2}$$

Elements in Fisher information matrix are then given as [14]:

$$J_{ij} = -E\left(H_{\lambda_i\lambda_j}\right) = -E\left(\frac{\partial^2}{\partial\lambda_i\partial\lambda_j}\left[\log p\left(\mathbf{x};\boldsymbol{\lambda}\right)\right]\right),\ i, j = 1, 2, 3. \tag{4-3}$$

Substituting Eq. (4-2) into Eq. (4-3), we have:

$$J_{ij} = -E\left(-\sum_{n=1}^{N}\frac{x_n}{s_n^2}\frac{\partial s_n}{\partial\lambda_i}\frac{\partial s_n}{\partial\lambda_j}\right) = \sum_{n=1}^{N}\frac{1}{s_n}\frac{\partial s_n}{\partial\lambda_i}\frac{\partial s_n}{\partial\lambda_j}. \tag{4-4}$$

Using $s_n = g\overline{I_n}$ and Eq. (4-1), the 3-by-3 Fisher information matrix in terms of parameters $\boldsymbol{\lambda} = [\alpha, \beta, L]$ is given as follows:

$$J=\begin{bmatrix} \sum_{n=1}^{N}\frac{g}{\overline{I_n}} & \sum_{n=1}^{N}\frac{g\cos\left(k_nL\right)}{\overline{I_n}} & \sum_{n=1}^{N}\frac{-gk_n\beta\sin\left(k_nL\right)}{\overline{I_n}} \\ \sum_{n=1}^{N}\frac{g\cos\left(k_nL\right)}{\overline{I_n}} & \sum_{n=1}^{N}\frac{g\cos^2\left(k_nL\right)}{\overline{I_n}} & \sum_{n=1}^{N}\frac{-gk_n\beta\sin\left(2k_nL\right)}{2\overline{I_n}} \\ \sum_{n=1}^{N}\frac{-gk_n\beta\sin\left(k_nL\right)}{\overline{I_n}} & \sum_{n=1}^{N}\frac{-gk_n\beta\sin\left(2k_nL\right)}{2\overline{I_n}} & \sum_{n=1}^{N}\frac{gk_n{}^2\beta^2\sin^2\left(k_nL\right)}{\overline{I_n}} \end{bmatrix}. \tag{4-5}$$

From estimation theory, we have $Var\left(L\right)\geq J_{33}^{-1}$, where J_{33}^{-1} is the CRB of the estimator's variance and is the corresponding element of the inverse matrix of J. CRB of the sensitivity of L is then:

$$\sigma_{CRB}=\left(J_{33}^{-1}\right)^{1/2}=\left(\frac{J_{11}J_{22}-J_{12}{}^2}{\det\left(J\right)}\right)^{1/2}, \tag{4-6}$$

where $\det\{\bullet\}$ represents the determinant of the input matrix. Eq. (5-6) specifies the general expression of shot noise-limited CRB for WSI techniques.

CRB is the fundamental limit independent of signal processing algorithms. To consider the constraint that is further imposed by the algorithm, the 4-step Carré algorithm used in the low coherence wavelength shifting interferometry (LC-WSI) technique [11] is selected as an example. We derive its ALG in the following manner. In this special case $N=4$ and the OPL is calculated by:

$$L=\frac{1}{k_0}\arctan\left\{\frac{\sqrt{\left[3\left(I_2-I_3\right)-\left(I_1-I_4\right)\right]\left(I_2-I_3+I_1-I_4\right)}}{\left(I_2+I_3-I_1-I_4\right)}\right\}, \tag{4-7}$$

where $k_0=(k_1+k_4)/2$ is the center wavenumber. Directly accessing the standard deviation of L is difficult due to the square root and the arctangent operators. To approximate the variance of L, we can linearize the expression and take only the first order of the Taylor expansion:

$$Var\left(L\right)=\sum_{n=1}^{4}\left(\frac{\partial L}{\partial I_n}\Big|_{\overline{I_n}}\right)^2\sigma_{I_n}^2. \tag{4-8}$$

We can derive the partial derivatives at each $\overline{I_n}$ and then use the property $Var(I_n) = Var(x_n)/g^2 = \overline{I_n}/g$ to obtain ALG:

$$\sigma_{ALG} = \sqrt{Var(L)} = \frac{\sqrt{BC}A}{k_0(A^2+BC)} \left\{ \begin{array}{l} \left(\frac{1}{A} - \frac{1}{2B} + \frac{1}{2C}\right)^2 \overline{I_1}/g \\ + \left(-\frac{1}{A} + \frac{3}{2B} + \frac{1}{2C}\right)^2 \overline{I_2}/g \\ + \left(-\frac{1}{A} - \frac{3}{2B} - \frac{1}{2C}\right)^2 \overline{I_3}/g \\ + \left(\frac{1}{A} + \frac{1}{2B} - \frac{1}{2C}\right)^2 \overline{I_4}/g \end{array} \right\}^{1/2}, \quad (4\text{-}9)$$

in which $A = \overline{I_2} + \overline{I_3} - \overline{I_1} - \overline{I_4}$, $B = 3\overline{I_2} - 3\overline{I_3} - \overline{I_1} + \overline{I_4}$, $C = \overline{I_2} - \overline{I_3} + \overline{I_1} - \overline{I_4}$. Eq. (4-9) explicitly expresses ALG based solely on the detected intensities, providing a substantially practical approach for ALG estimation. This is an intrinsic advantage for shot noise model since the noise level can be determined by signal strength alone. For Gaussian models, the property to derive Eq. (4-9) does not hold as the noise behaviors need to be characterized separately.

4.2.3 Simulation

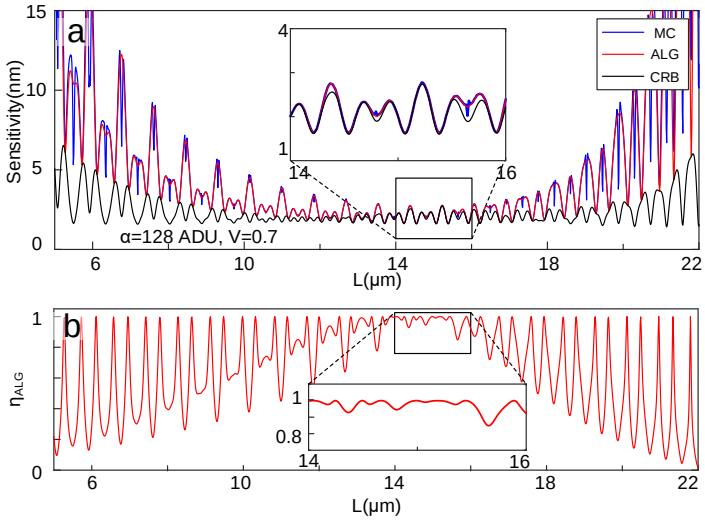

Fig. 4-2 (a) Comparison between CRB (black), ALG (red) and Monte Carlo simulation (blue) results with changing L. (b) algorithm efficiency.

We validate above derivations of CRB and ALG with simulation and compare them with the Monte Carlo results in Fig. 4-2. Intensity signals are generated according to Eq. (4-1) with $N = 4$, $[k_1, ..., k_4] = [7.22, 7.36, 7.50, 7.63]$ rad/μm, and other parameters specified in the figure. CRB and ALG are calculated by Eq. (4-6) and Eq. (4-9), respectively. The camera gain g is set at 34.4 e-/ADU, consistent with a camera used in experiments. Meanwhile, Monte Carlo simulation is carried out by repeatedly (50,000 times) adding Poisson noise to the noise-free intensity signals, processing them with Eq. (4-7) and calculating the standard deviation. To ensure a truthful comparison, no additional signal processing, such as temporal or spatial filtering, is used. Control variable method is used to inspect the effect of different parameters one at a time. In Fig. 4-2(a), α and β are fixed and L is varied. It is clear that the sensitivity performance has a strong dependence on L. Overall, the Monte Carlo results are in good agreement with the ALG curve, validating Eq. (4-9). And as expected, they are bounded from below by the CRB curve. Between 14 μm to 16 μm, ALG is close to CRB. In order to quantitatively inspect the difference between CRB and ALG, we use the concept of estimator efficiency in estimation theory and define $\eta_{ALG} = \sigma_{CRB}/\sigma_{ALG}$ as algorithm efficiency at a particular L. We can now convert the ALG curve in Fig. 4-2(a) to the efficiency curve in Fig. 4-2(b). The efficiency is approaching 1 around 14 μm. Toward smaller or larger L the efficiency becomes worse as a general trend, with an oscillating pattern due to a combined effect of the periodicity in CRB and ALG. By taking the mean value of η_L within the full detection range, we obtain the overall algorithm efficiency:

$$\overline{\eta_{ALG}} = \frac{1}{\Delta L}\int_{L \in Detect\ Range} \eta_{ALG} dL . \tag{4-10}$$

For example, the best detection range specified in [11] is 9~17 μm and hence the algorithm efficiency is 0.85. Depending on actual applications, we may not need such a large OPL detection range and the algorithm efficiency can be increased by excluding more low-efficiency region.

4.2.4 Experiment Sensitivity and System Efficiency Examination

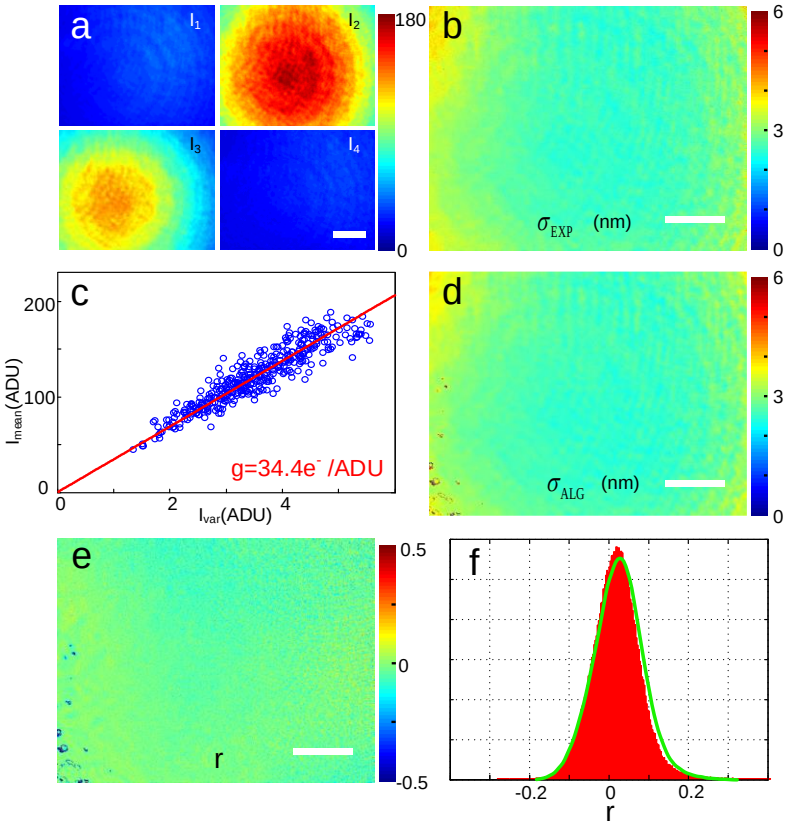

Fig. 4-3 (a) Spectra intensities $I_1 \sim I_4$ acquired at different bands for a single experiment; (b) EXP for 500 experiments; (c) camera g determined by the signal-variance method (blue circle represents a pixel and the red line is linear fitting result); (d) ALG estimated by Eq. (9); (e) the error ratio r; (f) histogram of r in red. By replacing $\overline{I_1} \sim \overline{I_4}$ with $I_1 \sim I_4$, the histogram of r is also plotted as the green curve. Scale bar: 20 μm.

Thus far, we have discussed the theoretical level in our framework that evaluates the algorithm efficiency. However, it remains unclear how the EXP in a real system deteriorates from ALG due to extrinsic noises. Next, we demonstrate the practical level sensitivity evaluation of our framework by experimentally testing a blank sample with the LC-WSI system. The system is based on a Mach-Zehnder interferometer and a swept laser source. The OPL difference between the two arms is carefully adjusted to 14 μm and verified by a slow scan method mentioned in [11]. The camera captures 4 images at shifting wavelength bands between 878 nm and 816 nm, shown in Fig. 4-3(a). This acquisition is repeated for 500 times. The EXP result is shown in Fig. 4-3(b). In the meantime, ALG is calculated based on Eq. (9) with an experimentally determined g. We use a signal-variance method [15,16] by repeatedly recording a static Gaussian beam and represent the mean and variance of each pixel in Fig. 5-3(c). To rule out the possibility of sweep repeatability

of the source, we fixed the wavelength of the swept source at $\lambda = 840\,nm$. Linear fitting is applied to these mean-variance pairs. The slope of the fitted line passing through the origin is the g value, 34.4 e^-/ADU. The good linear dependence between mean and variance also indicates the dominance of shot noise in the camera.

The result of ALG is given in Fig. 4-3(d). The noise-free $\overline{I_1} \sim \overline{I_4}$ are obtained as the mean intensity values of each band. Differences between EXP and ALG are hereby examined. We define a system error ratio as below:

$$r = \left(\sigma_{EXP} - \sigma_{ALG}\right)/\sigma_{ALG} = 1/\eta_{SYS} - 1, \tag{4-11}$$

where $\eta_{SYS} = \sigma_{ALG}/\sigma_{EXP}$ is the system efficiency. Therefore, the larger the error, the smaller the system efficiency; and in a system without any environmental or instrumental instabilities, $\eta_{SYS} = 1$ and $r = 0$. The spatial distribution of r is given in Fig. 4-3(e) along with its histogram shown in Fig. 4-3(f). The peak (statistical mean) position is off by 2.5% and the FWHM of the histogram is 12%. Ideally the error should be a delta function with a positive peak position. However, due to approximation inaccuracy (keeping only the first order statistics) and insufficient sampling, r in practice has broadened distribution, explaining the negative values. Hence the statistical mean value is the key metric to characterize the error. The corresponding system efficiency is $\eta_{SYS} = 97.6\%$. This shows our system hardware produces highly stable measurements. If a QPI system operates with a mean value of *r* less than 10%, i.e. $\eta_{SYS} > 90\%$, it may be considered highly efficient with minimal environmental and instrumental instabilities. High values of r, for example 50%, likely indicate non-ideal hardware conditions. The exact threshold percentiles that may be used to grade hardware performance will need to be systematically studied by evaluating the sensitivity performance of various QPI systems under a wide range of operating conditions.

Although in Eq. (4-9) the noise-free intensities are used, it is also feasible to use only a single set of noisy data for the estimation of ALG in moderate to high SNR scenarios [16]. This will significantly simplify the procedure and still yield highly accurate results. To prove this, we repeat the calculation for ALG using $I_1 \sim I_4$ from a single experiment. The system error ratio histogram is added to Fig. 4-3(f), which shows only a slight difference from the result using the average

spectra intensities. We also note that, in most modern high-sensitivity interferometry techniques such as the LC-WSI, the SNR is sufficient for such a single-set evaluation approach.

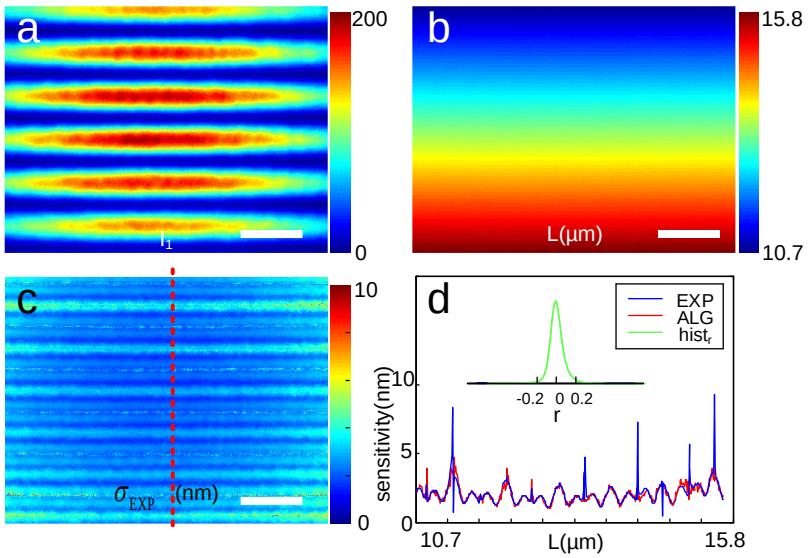

Fig. 4-4 (a). An off-axis interferogram to simulate slope effect; (b) OPL continuously changes in vertical direction whilst remains constant in horizontal direction; (c) experimental sensitivity; (d) vertical line profile(blue) marked in (c) matches well with the ALG (red). (inset) the histogram of error ratio r (green). Scale bar: 20 μm.

In live-cell imaging, the OPL of a sample can be up to several microns. Since the sensitivity performance has a strong dependence on L, examining the error ratio in Eq. (4-11) over a broad range of L is necessary. We shift the reference arm objective slightly off-axis to obtain fringes in the vertical direction shown in Fig. 4-4(a). It is equivalent to have a wedge sample with continuous height variation over several microns. Here the demodulated L ranges from 10.7 μm to 15.8 μm, as plotted in Fig. 4-4(b). The experimental sensitivity is given in Fig. 4-4(c). Along the vertical direction profile [see Fig. 4-4(d)], the oscillating pattern is obvious and matches well with the estimated ALG. The histogram of system error according to Eq. (4-11) shows a mean statistical mean of 0.5%. This again demonstrates that our system works almost ideally with high efficiency in this OPL range. The excellent performance can be attributed to the low coherence nature which ensures the speckle noise and coherence artifacts are avoided.

4.3 Extended Investigations of Other QPI Techniques

The abovementioned framework is generally compatible with any QPI technique. For example, we can easily extend the scope of investigation to phase shifting interferometry (PSI), especially

those most well-known ones introduced in Chapter 2. Compared to WSI, PSI has substantially more variations in implementations. Different number and value of phase steps lead to different modulation techniques. Even for the same modulation, there can exist various demodulation algorithms. Comparisons are thus needed not only vertically to examine algorithm efficiency and system efficiency, but also horizontally to compare different techniques, algorithms, and systems.

Another area of interest is off-axis interferometry which is the fundamental principle for digital holography. The signal model for this category is more complicated and the signal demodulation cannot be made pixel by pixel but based on a Fourier Transform method. Though it is difficult to have an analytical expression for CRB, the algorithm sensitivity will be studied.

4.3.1 PSI techniques

4.3.1.1 Methods

Proper signal modeling is still the key to the sensitivity analysis. In Section 2.2.1, the interference intensity formula has been introduced. The general method of deriving CRB remains largely similar to the WSI case described in Eqs. (4-2)-(4-6), and the ALG calculation will depend on the PSI signal forms. We can still apply the small quantity approximation for noise and use linear approximation to simplify the ALG expression. This procedure in general can be expressed mathematically as

$$\sigma_{ALG} = \sqrt{\sum_{n=1}^{N}\left(\frac{\partial L}{\partial \overline{I_n}}\right)^2 Var\left(I_n\right)}, \tag{4-12}$$

where $Var(I_n)$ is the variance of I_n. For shot noise-limited case, we can take advantage of the properties: $Var\left(I_n\right) = Var\left(x_n\right)/g^2 = \overline{I_n}/g$.

Extra cautions should be taken when comparing sensitivity horizontally between different techniques, algorithms, or systems. It is apparent that higher input energy, for example, due to higher number of frames, will improve the signal to noise ratio and thus sensitivity. Therefore, an impartial comparison should normalize the energy difference. Under the shot noise-limited case, our approach is to multiply the absolute sensitivity values with a normalization factor, $\sqrt{Ng\alpha}$,

thus defining a normalized sensitivity. Combined with the average sensitivity concept we just introduced, we define the normalized average sensitivity as

$$\overline{\sigma_{norm}} = \sqrt{\frac{1}{\Lambda}\int_{\Lambda} \sigma^{2}\left(Ng\alpha\right) dL}\,. \tag{4-13}$$

$Ng\alpha$ represents the total number of incoming photons (sample and reference arms combined, $g\alpha$) that are detected and converted to electrons during the N frames of acquisition. The normalized sensitivity is the one when the energy of a single photon is used for the entire acquisition of all frames. It reflects the energy efficiency of a modulation technique ($\sigma = \sigma_{CRB}$) or algorithm($\sigma = \sigma_{ALG}$), i.e., how efficient it is in utilizing light energy to produce the best sensitivity.

Next, we will discuss each specific type of PSI and analyze their sensitivity performance.

4.3.1.2 3-step (θ)

The 3-step PSI techniques use the least number of acquisitions to fully solve the parameters in the intensity signals. Creath (1988) proposed a 3-step technique with an equal phase step of θ so that $\mathbf{\Phi} = [-\theta, 0, \theta]$[17]. θ can take any arbitrary value as long as it is known beforehand. The FIM of this technique and all other techniques will not be shown to reduce redundancy. Finding the inverse matrix will lead to the CRB in Eq. (4-6). After a lengthy process to simplify it and replacing β with αV, we have

$$\sigma_{CRB,3step(\theta)} = \frac{1}{k_0\sqrt{g\alpha}} \times \sqrt{\frac{4 + 2\cos(\theta) + \left[2 + 3\cos\left(\theta\right) - 2\cos^{2}\left(\theta\right)\right] V\cos(k_0 L)}{-\left[2 + 4\cos\left(\theta\right)\right]\cos(2k_0 L) - \left[2 + \cos\left(\theta\right)\right] V\cos(3k_0 L)}{4V^{2}[\cos(\theta)\ +\ 1][\cos(\theta)\ -\ 1]^{2}}}\,. \tag{4-14}$$

This CRB depends heavily on L, including a $\cos(k_0 L)$ term and its harmonics up to the third order. Certain selections of θ can cancel some of the terms. For example, when $\theta = 2\pi/3$, the CRB formula is

$$\sigma_{CRB,3step(\theta=2\pi/3)} = \frac{1}{k_0\sqrt{g\alpha}}\sqrt{\frac{2-V\cos(3k_0L)}{3V^2}}, \qquad (4\text{-}15)$$

which has a period of $\Lambda = \lambda/3$. Equations (4-14) and (4-15) are inversely proportional to the square root of signal magnitude $\sqrt{g\alpha}$, a rough measure of SNR, which is expected. Besides, a larger visibility V will improve sensitivity.

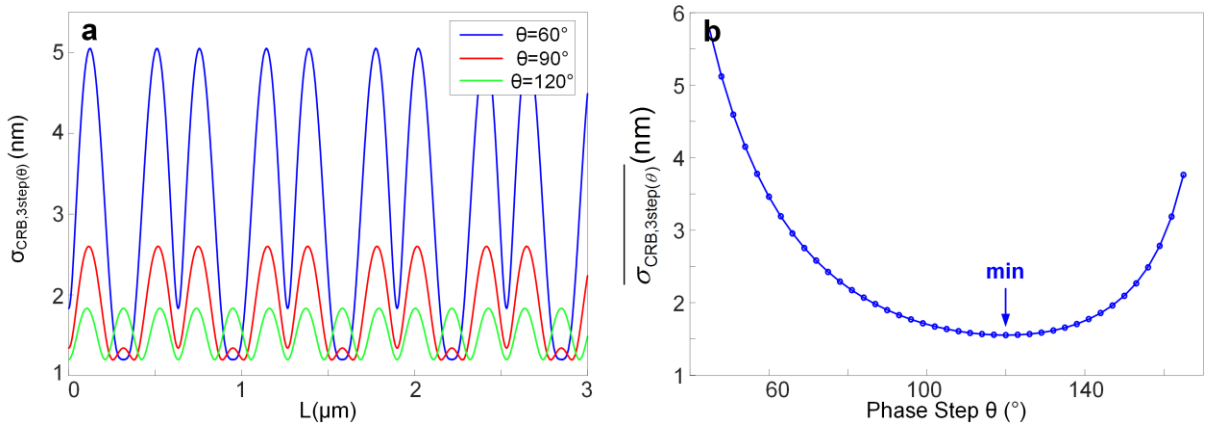

Fig. 4-5. (a) $\theta = 2\pi/3$, σ_{CRB} with changing L. (b) Comparisons of average CRB in a period, $\overline{\sigma_{CRB}}$, between different θ values. In this case, ALG are same as CRB.

We also use numerical simulation to evaluate CRB to support our derivations. The parameters are as follows: $\lambda = 633$ nm, $V = 0.8$, $\alpha = 128$, and $g = 34.4$ e$^-$/ADU. The acquisition mode has a bit length of 8 and a linear saturation well depth of 9,000 e$^-$. These settings are based on a camera (Allied Vision, Mako G-030) in our lab and g is experimentally determined using the mean-variance method mentioned in Fig. 4-3. We generate interference signals according to Eq. (2-3) with varying L and compute the CRB accordingly. As shown in Fig. 4-5(a), for various θ, the CRB varies significantly and periodically, consistent with Eq. (4-14). To compare the performance of different phase step θ, we compute an average $\overline{\sigma_{CRB}}$ for L over a period from 0 to $2\pi/k_0$:

$$\overline{\sigma_{CRB,3step(\theta)}} = \frac{1}{2k_0V[1-\cos(\theta)]}\sqrt{\frac{4+2\cos(\theta)}{[\cos(\theta)\ +\ 1]g\alpha}}. \qquad (4\text{-}16)$$

Its change with respect to θ is shown in Fig. 4-5(b). It is a convex function with the minimum at $\theta = 2\pi/3$, where the optimal CRB is located. This can also be verified theoretically by letting the derivative of Eq. (4-16) equal 0 and solving for θ.

Next, we study the ALG for the 3-step (θ) technique. Unlike CRB, ALG relies on the specific demodulation algorithm. The following formula is typically used:

$$L = \frac{1}{k_0}\arctan\left\{\left[\frac{1-\cos(\theta)}{\sin(\theta)}\right]\frac{I_1 - I_3}{2I_2 - I_1 - I_3}\right\}. \tag{4-17}$$

Following Eq. (4-12), the ALG is calculated and is identical to the CRB in Eq. (4-14). This means that if extrinsic noises can be eliminated, the algorithm in Eq. (4-17) is already capable of reaching the fundamental sensitivity limit. In other words, this algorithm is fully efficient ($\eta_{ALG} = 1$), and this modulation technique achieves the best sensitivity at $\theta = 2\pi/3$.

4.3.1.3 3-step ($\pi/2$)

Another well-known 3-step technique was proposed by Wyant et al. [18]. It is different from the previous 3-step technique in that it has a phase step of $\pi/2$ and an extra $\pi/4$ offset, thus making the phase shift set $\mathbf{\Phi} = [\pi/4, 3\pi/4, 5\pi/4]$. For this case, the CRB can be obtained as

$$\sigma_{CRB(ALG),3step(\pi/2)} = \frac{1}{k_0 V\sqrt{2g\alpha}} \times \sqrt{2 - V\sin(k_0 L + \frac{\pi}{4}) - \sin\left(2k_0 L\right) + V\sin\left(3k_0 L - \frac{\pi}{4}\right)}, \tag{4-18}$$

and the corresponding average CRB is

$$\overline{\sigma_{CRB,3step(\pi/2)}} = \frac{1}{k_0 V\sqrt{g\alpha}}. \tag{4-19}$$

For ALG computation, the algorithm to demodulate the interferograms is

$$L = \frac{1}{k_0}\arctan\left\{\frac{I_3 - I_2}{I_1 - I_2}\right\}. \tag{4-20}$$

Similar to the 3-step (θ) techniques, the ALG is exactly the same as the CRB in Eq. (4-18).

It is worth noting that fully efficient algorithms are currently available only for 3-step techniques. For other techniques in the following, there is a gap between CRB and ALG.

4.3.1.4 4-step ($\pi/2$)

In the 4-step ($\pi/2$) technique, $\mathbf{\Phi}=[0,\pi/2,\pi,3\pi/2]$. Under this case, CRB is

$$\sigma_{CRB,4step(\pi/2)}=\frac{1}{k_0}\sqrt{\frac{4-V^2+V^2\cos(4k_0L)}{8g\alpha V^2}}, \tag{4-21}$$

with a period of $\pi/2k_0$, a maximum value of $\left(2g\alpha k_0^{\,2}V^2\right)^{-1/2}$ when the cosine term equals to 1, and a minimum value of $\left[\left(2-V^2\right)\big/4g\alpha k_0^{\,2}V^2\right]^{1/2}$ when cosine term equals to -1. From this expression, we can also easily obtain

$$\overline{\sigma_{CRB,4step(\pi/2)}}=\frac{1}{k_0}\sqrt{\left(4-V^2\right)\big/8g\alpha V^2}\,. \tag{4-22}$$

The most well-known 4-step algorithm is

$$L=\frac{1}{k_0}\arctan\left\{\frac{I_2-I_4}{I_3-I_1}\right\}. \tag{4-23}$$

Accordingly, the ALG for this algorithm is

$$\sigma_{ALG,4step(\pi/2)}=\frac{1}{k_0V\sqrt{2g\alpha}}\,. \tag{4-24}$$

Therefore the ALG is a constant independent of L, as compared to the periodic CRB in Eq. (4-21). Moreover, the ALG is equal to the CRB at isolated locations determined by $4k_0L=2\pi m\Rightarrow L=\pi m/2k_0, m\in Z$.

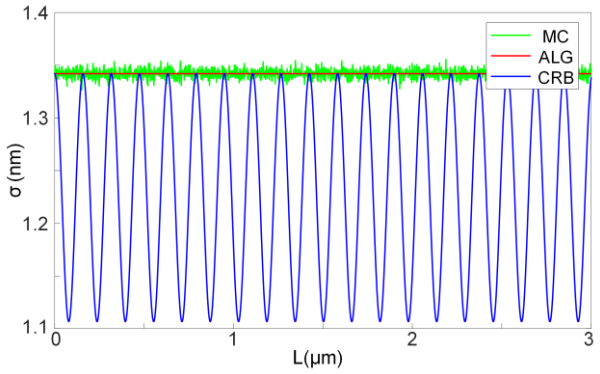

Fig. 4-6. CRB (blue) of 4-step ($\pi/2$) and corresponding ALG (red). Monte Carlo (MC) results are also shown here (green) to verify the correctness of ALG.

We then conduct a numerical simulation to validate the derivation. As shown in Fig. 4-6, the ALG is bounded from below by CRB, and is equal to the maxima of CRB. To verify that ALG is accurately estimated by Eq. (4-12), we also perform Monte Carlo simulation by adding simulated shot noise to 50,000 groups of signals and calculate the OPL standard deviation. The result agrees well with the ALG curve. Therefore, in shot noise-limited case, the gap between CRB and ALG indeed exists. This is fundamentally different from the uniform Gaussian noise model, wherein the 4-step algorithm is shown to be fully efficient [8].

4.3.1.5 4-step ($\pi/2$, Carré)

Another 4-step modulation technique is known as the Carré method [19]. Carré method does not assume any particular phase step, as long as the phase shifts between successive frames are equal. In this scenario, $\mathbf{\Phi} = [-3\theta/2, -\theta/2, \theta/2, 3\theta/2]$. Unlike the case of 3-step (θ), the phase step here can be unknown and solved for. For arbitrary θ, the CRB can be obtained as

$$\sigma_{CRB,Carre'(\theta)} = \sqrt{\frac{16 - V^2 + 3V^2\cos(\theta) + 2V^2\sin(\theta) + 5V^2\cos(2\theta) + V^2\cos(3\theta) + \left[32\cos\left(\frac{\theta}{2}\right) + 8\right]V\cos(\theta)\cos(k_0 L)}{+8V^2\left[\cos^2\left(\frac{\theta}{2}\right) - \sin^2\left(\frac{\theta}{2}\right)\sin^2(\theta)\right]\cos(2k_0 L) - 8V\cos(\theta)\cos(3k_0 L) - 2V^2\left[\sin(\theta) + \sin^2(\theta)\right]\cos(4k_0 L)}}{32g\alpha V^2[1 + V\cos\left(\frac{\theta}{2}\right)\cos(\theta)\cos(k_0 L)]}. \quad (4\text{-}25)$$

The most common selection of θ is $\pi/2$. The CRB expression is

$$\sigma_{CRB,Carre'(\pi/2)} = \frac{1}{k_0}\sqrt{\frac{4-V^2-V^2\cos(4k_0L)}{8g\alpha V^2}}. \tag{4-26}$$

which is similar to Eq. (4-21) but with an opposite sign for the cosine term, caused by the phase offset in φ_n. The $\overline{\sigma_{CRB}}$, however, is the same as in Eq. (4-22) because the cosine term is eliminated in integration.

The algorithm for Carré method differs completely from the previous 4-step technique:

$$L = \frac{1}{k_0}\arctan\left\{\frac{\sqrt{[3(I_2-I_3)-(I_1-I_4)][(I_1-I_4)+(I_2-I_3)]}}{I_2+I_3-I_1-I_4}\right\}. \tag{4-27}$$

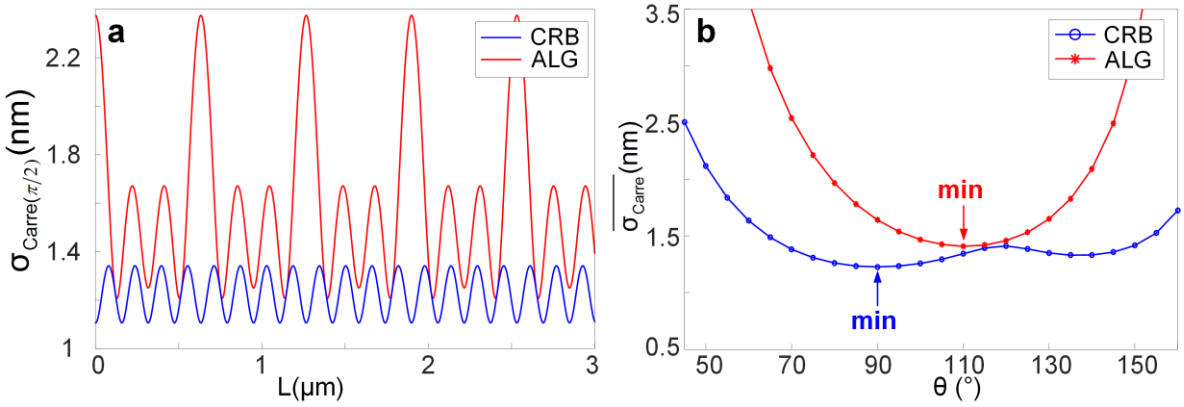

Fig. 4-7 (a) σ_{CRB} and σ_{ALG} for 4-step ($\theta=\pi/2$, Carré). (b) $\overline{\sigma_{CRB}}$ and $\overline{\sigma_{ALG}}$ for different phase step θ, showing different minima locations.

The associated ALG is given as

$$\sigma_{ALG,Carre'} = \frac{\sqrt{BC}A}{k_0\left(A^2+BC\right)}\times\sqrt{\begin{aligned}&\left(\frac{1}{A}-\frac{1}{2B}+\frac{1}{2C}\right)^2\overline{I_1}/g+\left(-\frac{1}{A}+\frac{3}{2B}+\frac{1}{2C}\right)^2\overline{I_2}/g\\&+\left(-\frac{1}{A}-\frac{3}{2B}-\frac{1}{2C}\right)^2\overline{I_3}/g+\left(\frac{1}{A}+\frac{1}{2B}-\frac{1}{2C}\right)^2\overline{I_4}/g\end{aligned}}, \tag{4-28}$$

in which $A=\overline{I_2}+\overline{I_3}-\overline{I_1}-\overline{I_4}$, $B=3\overline{I_2}-3\overline{I_3}-\overline{I_1}+\overline{I_4}$, $C=\overline{I_2}-\overline{I_3}+\overline{I_1}-\overline{I_4}$. For these complicated analytical solutions, numerical simulation is a better way to visualize the difference between ALG and CRB. In Fig. 4-7(a), CRB and ALG for $\theta=\pi/2$ are shown. Although the ALG seems to reach CRB at a few locations of L, its overall efficiency suffers severe degradation. Fig. 4-7(b) shows the average CRB and ALG respectively for different phase step θ. At $\theta=\pi/2$, the average CRB is optimal, whilst for ALG, $\theta=11\pi/18$ appears to be the best, roughly in line with the uniform Gaussian noise case [20]. We recall that CRB is modulation technique-related, and the ALG is algorithm-related. Although the current algorithm works the best at $\theta=11\pi/18$, the best sensitivity potential is located at $\theta=\pi/2$, if certain algorithms exist to achieve it.

4.3.1.6 5-step ($\pi/2$)

When phase steps are more than four, two famous benchmark algorithms are mostly used. The first is a 5-step PSI technique proposed by Hariharan et al [21]. Five measurements of interferogram are taken with linear phase shift between frames. Similar to the 3-step (θ) case, the preset phase step can vary, but the best value is determined as $\pi/2$ to make it insensitive to phase shift calibration errors. The CRB for this case is

$$\sigma_{CRB}=\frac{1}{k_0}\sqrt{\frac{12-3V^2+V\cos(k_0L)+2\cos(2k_0L)+V\cos(3k_0L)+3V^2\cos(4k_0L)}{4g\alpha V^2\left[7+V\cos(k_0L)\right]}} \quad . \quad (4\text{-}29)$$

When the phase step is $\pi/2$, the algorithm to obtain L is straightforward:

$$L=\frac{1}{k_0}\arctan\left\{\frac{2(I_2-I_4)}{2I_3-I_5-I_1}\right\} . \quad (4\text{-}30)$$

Correspondingly, the ALG is given as

$$\sigma_{ALG,5step(\pi/2)}=\frac{1}{4k_0}\times\sqrt{\frac{14+V\cos(k_0L)+2\cos(2k_0L)-V\cos\left(3k_0L\right)}{2g\alpha V^2}} \quad . \quad (4\text{-}31)$$

4.3.1.7 N-step ($2\pi/N$, synchronous detection)

The other multi-frame-technique is the *N*-step synchronous method proposed by Bruning et al [22]. It is a category of techniques with N phase shifts and phase step $\theta = 2\pi/N$. Therefore, $\varphi_n = 2\pi(n-1)/N, n = 1 \sim N$. Analytical CRB is difficult to be simplified.

The algorithm to calculate OPL for synchronous detection is

$$L = \frac{1}{k_0}\arctan\left[\frac{-\sum_{n=1}^{N} I_n \sin(\theta_n)}{\sum_{n=1}^{N} I_n \cos(\theta_n)}\right] . \tag{4-32}$$

The corresponding ALG is then

$$\sigma_{ALG,Nstep} = \frac{1}{k_0}\frac{1}{(\sum_{j=1}^{N}\overline{I_j}\cos\varphi_j)^2 + (\sum_{j=1}^{N}\overline{I_j}\sin\varphi_j)^2} \times\sqrt{\sum_{n=1}^{N}\left[\sin\varphi_n(\sum_{j=1}^{N}\overline{I_n}\cos\varphi_j) + \cos\varphi_n(\sum_{j=1}^{N}\overline{I_n}\sin\varphi_j)\right]^2\frac{\overline{I_n}}{g}} . \tag{4-33}$$

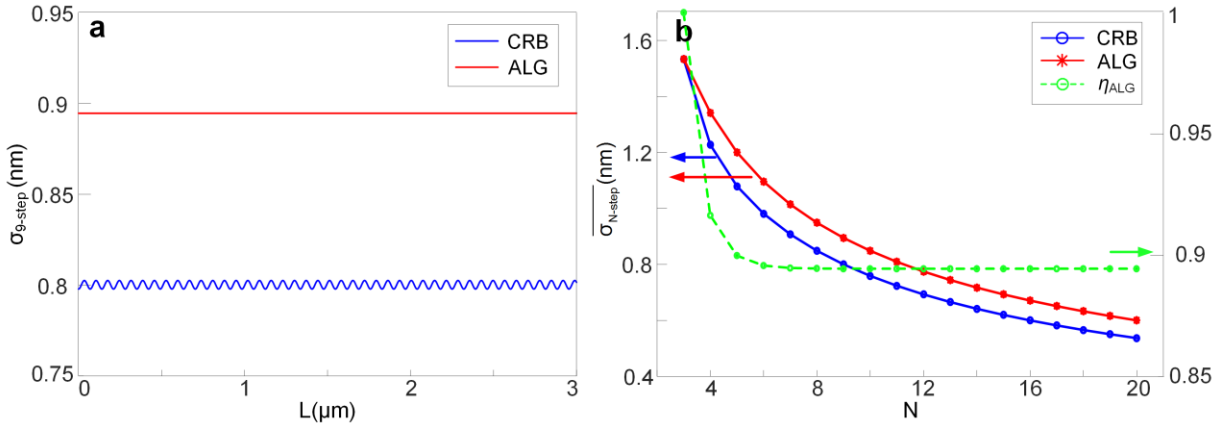

Fig. 4-8. (a) CRB and ALG for $N = 9$ in N-step synchronous detection. (b) Average CRB, ALG and algorithm efficiency for different N values.

Numerical simulation of CRB and ALG sensitivity for case $N = 9$ is shown in Fig. 4-8(a). The average algorithm efficiency is 89%, indicating room for potential improvement but nonetheless already high. The changes of the two sensitivities vs. *N* are shown in Fig. 4-8(b). There is a

decreasing trend for both curves. Since we have the analytical expression for ALG, its behavior can be inferred through the asymptotic expression if we assume N is large so that

$$\begin{aligned}\sum_{j=1}^{N}\overline{I_j}\cos\varphi_j &\approx \frac{\alpha NV}{2}\cos(k_0L)\\ \sum_{j=1}^{N}\overline{I_j}\sin\varphi_j &= \frac{-\beta N}{2}\cos(k_0L)\end{aligned}. \tag{4-34}$$

Substituting Eq. (4-34) into Eq. (4-33), we have

$$\lim_{N\to\infty}\sigma_{ALG,Nstep} = \frac{1}{k_0V}\sqrt{\frac{2}{gN\alpha}}. \tag{4-35}$$

In this expression, ALG is inversely proportional to $\sqrt{N\alpha}$, which explains the decreasing trend as shown in the simulation. In Fig. 4-8(b) we also give the algorithm efficiency curve. It remains nearly constant when N increases further.

4.3.1.8 Energy Normalization and Comparisons of PSI techniques

Comparisons of average CRB and ALG are made between the aforementioned techniques in Table 1 for $V = 0.8$. However, as we mentioned before, a fair comparison requires a certain energy normalization scheme. This is because these techniques involve different number of frames (N) and inherently different SNR. For example, in the N-step case, a greater N implies higher total signal energy and therefore higher sensitivity, as shown in Eq. (4-35). In addition, all the CRB and ALG expressions are inversely proportional to $\sqrt{g\alpha}$. Therefore, we multiply a normalization factor, $\sqrt{Ng\alpha}$, and define a normalized average sensitivity as in Eq. (4-13).

The normalized average CRB values are also given in Table 4-1. A smaller $\overline{\sigma_{CRB,norm}}$ indicates better sensitivity achieved by the same system energy input. The N-step synchronous technique is still the smallest, and is closely followed by the two 4-step techniques. The 3-step ($\pi/2$) technique has the highest CRB. Here, both the normal 4-step and Carré method use $\pi/2$ phase step can achieve the same results as we discussed earlier.

Table 4-1 Comparisons of for different techniques with $V = 0.8$.

Techniques	$\overline{\sigma_{CRB}}$ (nm)	$\overline{\sigma_{CRB,norm}}$	$\overline{\sigma_{ALG}}$ (nm)	$\overline{\sigma_{ALG,norm}}$	η_{ALG}
3-step (θ,2π/3)	1.55	178.0	1.55	178.0	100%
3-step(π/2)	1.90	217.9	1.90	217.9	100%
4-step(π/2)	1.23	163.2	1.34	178.1	92%
4-step, Carré(π/2)	1.23	163.2	1.64	218.2	75%
5-step	1.14	169.2	1.26	186.3	90%
N-step (N=9)	0.80	159.3	0.89	178.1	89%

The same normalization factor can be applied to normalize the ALG, also shown in Table 4-1. They reflect the energy efficiency of an algorithm, which differs from the CRB. 3-step ($2\pi/3$) has the best ALG, which is also fully efficient. The 4-step ($\pi/2$) algorithm works much more efficient than the 4-step Carré algorithm, hence obtaining better ALG sensitivity. The ALG of 3-step ($2\pi/3$) and 4-step ($\pi/2$) algorithms are identical (albeit slight numerical computation discrepancy exists), and the *N*-step algorithm will also converge to the same values if Eq. (4-35) is used.

Table 4-2 A normalized algorithm sensitivity lookup table for common algorithms at different V .

V	0.1	0.2	0.3	0.4	0.5	0.6	0.7	0.8	0.9	1
3-step (θ,2π/3)	1425	712	475	356	285	237	204	178	158	142
3-step (π/2)	1744	872	581	436	349	291	249	218	194	174
4-step (π/2)	1425	712	475	356	285	237	204	178	158	142
4-step, Carré(π/2)	1745	872	582	436	349	291	249	218	194	174
5-step	1490	745	497	373	298	248	213	186	166	149
N-step (N=9)	1425	712	475	356	285	237	204	178	158	142

The shot noise-limited, normalized CRB and ALG are independent of system hardware and power. For a specific system, its sensitivity can be conveniently calculated by dividing these values with $\sqrt{Ng\alpha}$. Here we calculate the normalized average ALG values under different visibility settings in Table 4-2. Readers can conveniently find the closest visibility and convert the value to the ALG of their own specific system by dividing $\sqrt{Ng\alpha}$. If the experimental sensitivity is clearly worse than the converted ALG, the system is likely instable in its instrument and/or environment.

4.3.2 Off-axis digital holography

4.3.2.1 System and Signals

As an example, we examine a Mach-Zehnder off-axis interferometer, as shown in Fig. 2-1(a). We note that the following derivation is more general and fully applicable to other types of off-axis interferometry. The hologram on the camera can be expressed as

$$I_{mn} = \alpha_{mn} + \beta_{mn} e^{j\left[\varphi^{s}_{mn} - k_M m - k_N n\right]} + c.c. + z_{mn} \quad , \tag{4-36}$$

where φ^{s}_{mn} is sample phase, z_{mn} is the real intensity noise, k_M and k_N are normalized spatial frequencies, *c.c.* is the complex conjugate, $m \in [0, M-1]$ and $n \in [0, N-1]$ are discrete camera pixel indices along x and y directions. In general, α_{mn} and β_{mn} are functions of *m* and *n* due to spatial variations in illumination, sample transmittance and interference efficiency. A typical hologram is shown in Fig. 2-1(b), with its 2D discrete Fourier transform (DFT), $\tilde{I}_{pq}$, $p \in [0, M-1]$, $q \in [0, N-1]$, shown in Fig. 2-1(c). The reconstruction of the measured sample phase φ^{Meas}_{mn} with the Fourier transform algorithm consists of three major steps [23]: (i) sideband centering by downshifting (or upshifting), (ii) low-pass (LP) filtering, and (iii) inverse DFT and phase extraction [Fig. 2-1(d)].

Centering is performed by multiplying I_{mn} with a carrier frequency $exp\left[\, j\left(k^{e}_{M} m + k^{e}_{N} n\right)\right]$, where k^{e}_{M} and k^{e}_{N} are the estimated values of k_M and k_N. Usually, the small estimation error may lead to a fixed background slope in the demodulated phase image. It will not, however, affect the variance of phase. We hence assume the centering is perfect, i.e. $k^{e}_{M} = k_M$ and $k^{e}_{N} = k_N$. As a result, the DFT of the sideband signal is located at DC. It is then LP-filtered with an aperture function H_{pq}, which is typically unity within the passband and zero outside. Following an inverse 2D DFT, the phase of the signal is then extracted. Mathematically, this signal processing procedure can be expressed as

$$\begin{aligned}\varphi_{mn}^{Meas} &= \angle LP\left[I_{mn} e^{j(k_M m + k_N n)} \right] \\ &= \angle\left\{ \beta_{mn} e^{j\varphi_{mn}^{s}} + LP\left[z_{mn} e^{j(k_M m + k_N n)} \right] \right\}, \\ &= \angle\left\{ \beta_{mn} e^{j\varphi_{mn}^{s}} + z_{mn}^{LP} \right\}\end{aligned} \tag{4-37}$$

where out-of-band signals are removed and z_{mn}^{LP} is a complex variable, representing the carrier-shifted, LP-filtered version of z_{mn}.

4.3.2.2 Algorithm Sensitivity

To obtain the angle in Eq. (5-37), we use the following conversion:

$$\begin{aligned}\beta_{mn} e^{j\varphi_{mn}^{s}} + z_{mn}^{LP} &= \beta_{mn} e^{j\varphi_{mn}^{s}} \left(1 + \frac{z_{mn}^{LP} e^{-j\varphi_{mn}^{s}}}{\beta^{mn}} \right) \\ &\simeq \beta_{mn} e^{j\varphi_{mn}^{s}} e^{j\frac{\mathrm{Im}\left(z_{mn}^{LP}\right)\cos\varphi_{mn}^{s} - \mathrm{Re}\left(z_{mn}^{LP}\right)\sin\varphi_{mn}^{s}}{\beta_{mn}}},\end{aligned} \tag{4-38}$$

where $\mathrm{Re}(\cdot)$ and $\mathrm{Im}(\cdot)$ are the real and imaginary parts and the approximation follows from z_{mn}^{LP} being a small quantity. To further process Eq. (4-38), an explicit expression is developed for $z_{mn}^{LP} = LP\left[z_{mn} e^{j(k_M m + k_N n)} \right]$:

$$z_{mn}^{LP} = \left[z_{mn} e^{j(k_M m + k_N n)} \right] \otimes h_{mn}. \tag{4-39}$$

where h_{mn} denotes the inverse DFT of H_{pq}, and $\otimes$ represents circular convolution. Note that as a filter aperture, H_{pq} is real and even, and so is h_{mn}. We then arrive at the imaginary part of z_{mn}^{LP},

$$\mathrm{Im}\left(z_{mn}^{LP} \right) = \left[z_{mn} \sin\left(k_M m + k_N n \right) \right] \otimes h_{mn}. \tag{4-40}$$

Similarly,

$$\mathrm{Re}\left(z_{mn}^{LP} \right) = \left[z_{mn} \cos\left(k_M m + k_N n \right) \right] \otimes h_{mn}. \tag{4-41}$$

Substituting Eqs. (5-40) and (4-41) into Eq. (4-38):

$$\beta_{mn}e^{j\varphi_{mn}^{s}}+z_{mn}^{LP}\simeq\beta_{mn}e^{j\varphi_{mn}^{s}}e^{j\frac{\left[z_{mn}\sin\left(k_{M}m+k_{N}n-\varphi_{mn}^{s}\right)\right]\otimes h_{mn}}{\beta_{mn}}}. \tag{4-42}$$

The phase sensitivity is typically calculated as the square root of the variance of φ_{mn}^{Meas}. Combining Eqs. (4-37) and (4-42), we have

$$\begin{aligned}\sigma_{mn}^{\varphi}&=\sqrt{Var\left(\varphi_{mn}^{Meas}\right)}\\&=\frac{1}{\beta_{mn}}\sqrt{\left[Var\left(z_{mn}\right)\sin^{2}\left(k_{M}m+k_{N}n-\varphi_{mn}^{s}\right)\right]\otimes h_{mn}^{2}}\end{aligned}. \tag{4-43}$$

Equation (4-43) provides a general formula to quantify phase sensitivity, where intensity noise, carrier frequency and filter properties are involved.

To further develop Eq. (4-43), we consider two different classes of z_{mn}, shot-noise-limited and uniform noise. For the former, the noise variance is non-uniform across the image and is determined by the hologram intensity at each pixel. For uniform noise, all image pixels have the same noise variance. In modern imaging, most scientific cameras are capable of shot-noise-limited operation, where detector noises are negligible as compared to photon noise.

From the Poisson statistics of shot noise, we have [16]

$$\begin{aligned}Var\left(z_{mn}\right)&=\frac{Mean\left(I_{mn}\right)}{g}\\&=\frac{1}{g}\left[\alpha_{mn}+2\beta_{mn}\cos\left(\varphi_{mn}^{s}-k_{M}m-k_{N}n\right)\right]\end{aligned}, \tag{4-44}$$

where g is the conversion gain of the camera, i.e. the number of photoelectrons per analog-to-digital unit (ADU). This well-known mean-variance relation also offers a convenient way to test the validity of shot-noise-limited model and to estimate the value of g [15].

Next we examine the effect of h_{mn} in Eq. (4-43). Typically, its Fourier transform, H_{pq}, is unity within its passband and zero elsewhere. The contour of the passband can be flexible (circle and ellipse are the most common). Without loss of generality, we define r as the maximum distance from the origin to the contour, or the bandwidth of H_{pq}. Clearly, h_{mn}^{2}, i.e. $H_{pq}\otimes H_{pq}$ in Fourier

domain, is also an LP filter with a bandwidth of $2r$. Considering Eq. (4-43) with $Var(z_{mn})$ replaced with Eq. (4-44), all the terms to the left of the convolution operator located outside this bandwidth will be eliminated by h_{mn}^2. For example, $\alpha_{mn}\sin^2\left(k_M m + k_N n - \varphi_{mn}^s\right)/g$ is the sum of $\alpha_{mn}/2g$ and $\alpha_{mn}\cos\left(2k_M m + 2k_N n - 2\varphi_{mn}^s\right)/2g$. The latter is a high frequency term well beyond filter bandwidth, because the carrier frequency $\left[k_M, k_N\right]$ is typically set sufficiently large to ensure adequate separation between DC and sideband components. After eliminating these out-of-band terms, the shot-noise-limited phase sensitivity (ALG) becomes:

$$\sigma_{mn,SN1}^{\varphi} = \sqrt{\frac{\alpha_{mn} \otimes h_{mn}^2}{2g\beta_{mn}^2}} \quad . \tag{4-45}$$

Since α_{mn}, β_{mn}, g and h_{mn} are known or can be extracted from the hologram, the phase sensitivity can thus be determined. To further simplify Eq. (4-45), we note that h_{mn}^2 represents a spatial point-spread function that can be well approximated as a Kronecker delta function δ_{mn}, the amplitude of which is the spatial sum of h_{mn}^2. Using the Parseval's theorem on h_{mn}, $\sum_{m,n} h_{mn}^2 = \sum_{p,q}\left|H_{pq}\right|^2 / MN = S/MN$, where S is the aperture area of H_{pq}, or the total number of pixels within the filter passband. This term is the ratio of S to the whole Fourier area MN. Therefore,

$$\alpha_{mn} \otimes h_{mn}^2 \simeq \alpha_{mn} \otimes (\frac{S}{MN}\delta_{mn}) = \frac{S\alpha_{mn}}{MN} \quad . \tag{4-46}$$

Substituting Eq. (4-46) into Eq. (4-45), the phase sensitivity under shot-noise-limited case is approximated as

$$\sigma_{mn,SN2}^{\varphi} = \sqrt{\frac{S\alpha_{mn}}{2gMN\beta_{mn}^2}} = \sqrt{\frac{2S}{gMN\alpha_{mn}V_{mn}^2}} \quad , \tag{4-47}$$

in which $V_{mn} = 2\beta_{mn}/\alpha_{mn}$ is the fringe visibility. Equation (4-47) provides some intuitive insights into the off-axis phase sensitivity. Since both α_{mn} and β_{mn} are pixel dependent, the formula

accounts for spatial variations in illumination and sample transmittance, which was not considered previously [24,25]. Unsurprisingly, the ratio of S/MN is consistent with the proportional reduction of noise energy. While a smaller filter improves sensitivity, its size is bounded from below by the bandwidth of the image, or loss of information and resolution would occur.

For the case of uniform noise, we assume all camera pixels have identical noise statistics, $Var\left(z_{mn}\right)=\sigma_a^2$. Following a similar approach to the shot noise case, Eq. (4-43) turns into

$$\sigma_{mn,UN}^{\varphi}=\sqrt{\frac{\sigma_a^2\otimes h_{mn}^2}{2\beta_{mn}^2}}\simeq\sqrt{\frac{\sigma_a^2 S}{2MN\beta_{mn}^2}}\,. \tag{4-48}$$

4.3.2.3 Simulation Validation

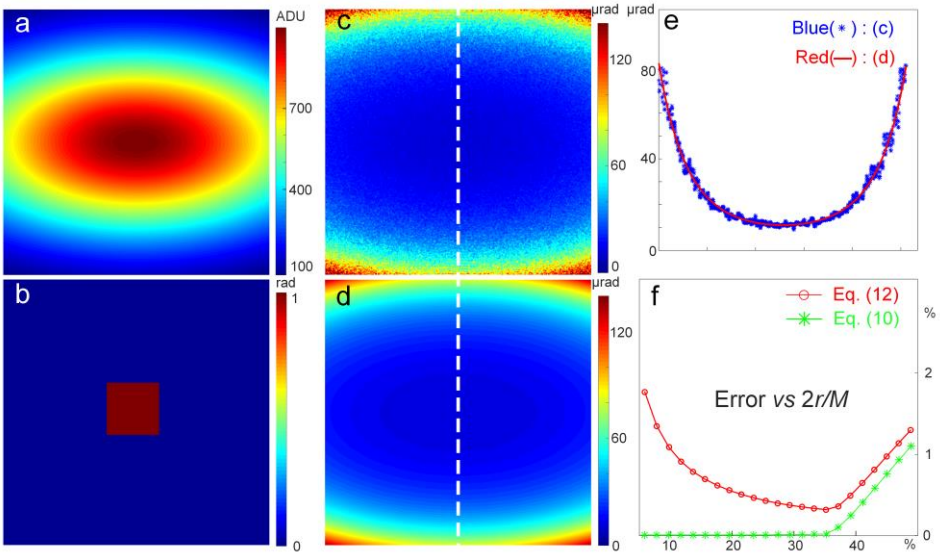

Fig. 4-9 Simulation results for the shot-noise-limited case. (a) The same elliptical Gaussian amplitude for both arms; (b) sample phase profile with a 1 rad square at center (M, N=1024); (c) phase sensitivity obtained from simulations wherein a circular LP filter of bandwidth r=90 is used; (d) phase sensitivity calculated from Eq. (4-45); (e) comparison between (c) and (d) on the marked center column; (f) error (%) between simulation and Eq. (4-47) (red), simulation and Eq. (4-45) (green), with different LP filter sizes.

The derivations above can be verified by numerical simulations. For example, we assume for both arms a Gaussian intensity distribution across the field of view as in Fig. 4-9(a) and their phase difference as shown in Fig. 4-9(b). The noise-free off-axis hologram can be generated with a certain carrier frequency ($k_M=k_N=256$). For the shot-noise-limited case, Poisson noise is added to the hologram and the temporal standard deviation of reconstructed phase at each pixel is

calculated from a series of phase images [Fig. 4-9(c)]. This simulated result is compared with the theoretical ALG formula Eq. (10) [Fig. 4-9(d)] and they match almost perfectly [Fig. 4-9(e)]. In the simulation we used different filter shapes (elliptical, rectangular) in addition to the circular filter and all of them validate Eq. (4-45).

We also evaluate the percentage error between simulation and our calculation by both Eqs. (4-45) and (4-47). The mean error percentage across the image is plotted in Fig. 4-9(f) for different values of $2r/M$, which is used as a measure of filter size. The error between Eq. (4-47) and simulation (red) firstly decreases with increasing filter bandwidth since the delta function approximation in Eq. (4-46) becomes more accurate. Meanwhile, the error for Eq. (4-45) (green) remains essentially zero, confirming its accuracy. As the filter size $2r/M$ exceeds ~35%, the errors start to increase for both Eqs. (4-45) and (4-47). This is because h^2 gradually loses its effectiveness as an LP filter for eliminating high frequency components, which is an assumption for deriving Eq. (4-45). However, for off-axis interferometry applications, such a large filter size is rarely if ever used because of the need to separate DC and sidebands. Therefore, we conclude that Eq. (4-45) provides an accurate calculation of phase sensitivity while the further approximated version, Eq. (5-47), can maintain a small error of <2%. The same approach, except for replacing the shot noise with uniformly distributed random noise, can be used to verify Eq. (4-48).

We then use these formulae experimentally to evaluate system phase sensitivity as well as system efficiency, which is defined as the ratio of ALG to EXP, as previously discussed for PSI and WSI [26,27]. We used the system in Fig. 2-1. The laser wavelength is $\lambda = 840\,nm$ (linewidth: 0.06 *nm*) and the camera (Allied Vision; Mako G030) gain g has been previously measured as 34.4 e^-/ADU using Eq. (4-44) [27]. First we captured 800 holograms of a blank glass slide sample at 250 fps and calculated its EXP [Fig. 4-10(a)]. Next, we estimated the ALG with the shot-noise-limited phase sensitivity formula in Eq. (4-47). Unlike the simulations where we had prior knowledge of α_{mn} and β_{mn}, these values are experimentally obtained from the acquired holograms as the intensities of the filtered DC component (α_{mn}) and the filtered sideband signal (β_{mn}). The values for ALG is subsequently calculated [Fig. 4-10(b)], which agrees well with the experimental data with an average system efficiency of 97.5% within the field of view [Fig. 4-10(c) shows the center column comparison]. It should be pointed out that the ALG represents the best temporal

phase sensitivity that can be achieved with the Fourier transform algorithm. Clearly, this high system efficiency indicates the effects of system instabilities, such as source fluctuation, mechanical vibration, air turbulence, etc., are minimal in this system. Otherwise, a low efficiency would be strong evidence that the system hardware requires improvement.

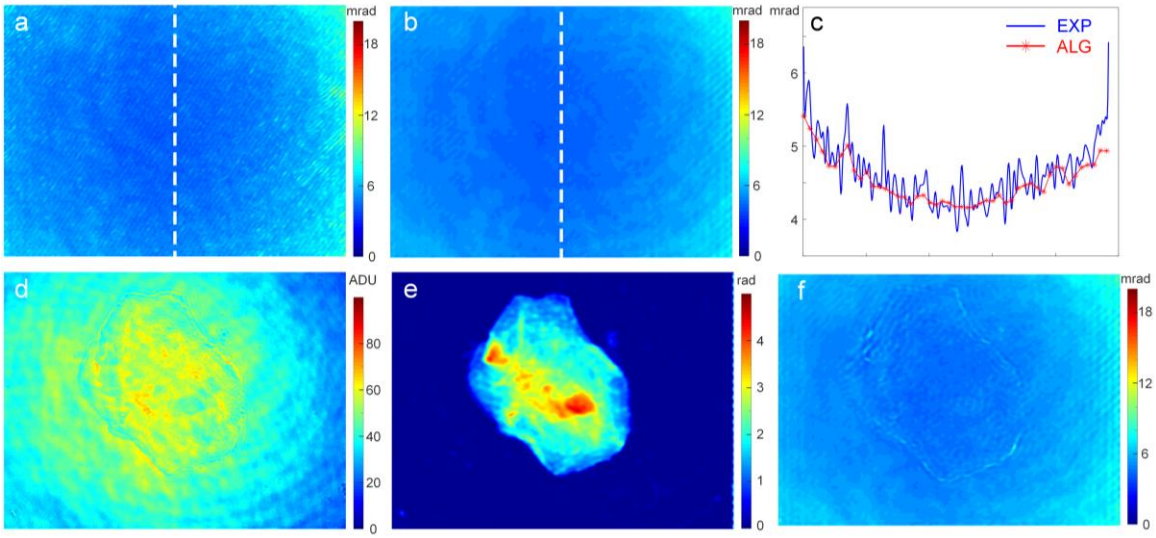

Fig. 4-10 Estimation of the phase sensitivity in experiment. (a) standard deviation distribution (M=644, N=484) of phase sensitivity (EXP) of 800 consecutive reconstructed phase images of a glass slide sample; (b) ALG estimated from a single hologram by Eq. (4-47), with a mean system efficiency of 97.5%; (c) single column comparison between (a) and (b); (d,e) intensity and phase image of a human cheek cell; (f) ALG estimated from cheek cell hologram.

The above phase sensitivity formulae indicate that intensity changes in α_{mn} and β_{mn} can lead to varying phase sensitivities if the sample causes strong intensity variation. For weakly absorbing and scattering biological samples typical for most QPI applications, the intensity changes are small [see Figs. 4-10(d,e) for a human cheek cell example] so that the difference between phase sensitivity [Fig. 4-10(f)] and the same region of Fig. 4-10(b) is small. Nonetheless, the spatial dependence can be seen at the edge of the cell, where diffraction is usually the strongest to alter sample intensity.

4.4 Conclusions

We present a quantitative framework for sensitivity assessment in QPI. The three-level structure provides comprehensive evaluations on both the algorithm efficiency as compared to CRB as well

as the system sensitivity degradation due to system hardware noises. In the WSI example, analytical expressions of CRB and ALG are obtained. It is shown that ALG and its efficiency depends closely on OPL. The proposed framework is used to identify the optimal OPL range and to calculate overall algorithm efficiency. In addition, efficiency of system hardware quantifies the overall experimental performance, and can also be used to guide system optimization. Our evaluation method produces an objective evaluation of the algorithmic and experimental sensitivity over the full detection range. Finally, we note that WSI is simply an example to demonstrate this framework. The method can be extended to sensitivity evaluation for other QPI techniques, and provide insights into algorithm selection and system optimization. We introduce the method to evaluate the sensitivity of PSI and study the shot noise-limited performance for several common PSI techniques. The behaviour of each phase modulation technique and the performance of each current algorithm are theoretically and numerically investigated. Off-axis interferometry, on the other hand, due to the complexity for an analytical form of CRB, algorithmic sensitivity has been mainly investigated.

References

[1] Z. Wang, L. Millet, M. Mir, H. Ding, S. Unarunotai, J. Rogers, M.U. Gillette, and G. Popescu, "Spatial light interference microscopy (SLIM)," Optics Express **19**, 1016-1026 (2011).

[2] R. Shang, S. Chen, C. Li, and Y. Zhu, "Spectral modulation interferometry for quantitative phase imaging," Biomedical Optics Express **6**, 473-479 (2015).

[3] T. Slabý, P. Kolman, Z. Dostál, M. Antoš, M. Lošťák, and R. Chmelík, "Off-axis setup taking full advantage of incoherent illumination in coherence-controlled holographic microscope," Optics Express **21**, 14747-14762 (2013).

[4] A. S. G. Singh, A. Anand, R. A. Leitgeb, and B. Javidi, "Lateral shearing digital holographic imaging of small biological specimens," Optics Express **20**, 23617-23622 (2012).

[5] P. Hosseini, R. Zhou, Y. Kim, C. Peres, A. Diaspro, C. Kuang, Z. Yaqoob, and P. T. C. So, "Pushing phase and amplitude sensitivity limits in interferometric microscopy," Optics Letters **41**, 1656-1659 (2016).

[6] B. Bhaduri, H. Pham, M. Mir, and G. Popescu, “Diffraction phase microscopy with white light,” Optics Letters **37**, 1094-1096 (2012).

[7] A. Patil, R. Langoju, P. Rastogi, and S. Ramani, “Statistical study and experimental verification of high-resolution methods in phase-shifting interferometry,” Journal of Optical Society of America A **24**, 794-813 (2007).

[8] E. W. Rogala and H. H. Barrett, “Phase-shifting interferometry and maximum-likelihood estimation theory,” Applied Optics **36**, 8871-8876 (1997).

[9] C. Rathjen, “Statistical properties of phase-shift algorithms,” Journal of Optical Society of America A **12**, 1997-2008 (1995).

[10] E. Hack, and J. Burke, “Measurement uncertainty of linear phase-stepping algorithms,” Review of Scientific Instruments **82**, 061101 (2011).

[11] S. Chen, C. Li, and Y. Zhu, “Low-coherence wavelength shifting interferometry for high-speed quantitative phase imaging,” Optics Letters **41**, 3431-3434 (2016).

[12] T. Takahashi, Y. Ishii, and R. Onodera, “Phase-shifting interferometric profilometry with a wavelength-tunable diode source,” Optical Review **21**, 410-414 (2014).

[13] M. Suematsu and M. Takeda, “Wavelength-shift interferometry for distance measurements using the Fourier transform technique for fringe analysis,” Applied Optics **30**, 4046-4055 (1991).

[14] D. C. Rife and R. R. Boorstyn, “Single tone parameter estimation from discrete-time observations,” IEEE Transactions on Information Theory **20**, 591-598 (1974).

[15] L. Mortara and A. Fowler, “Evaluations Of Charge-Coupled Device (CCD) Performance For Astronomical Use,” Proceedings of SPIE **0290**, 28-33 (1981).

[16] C. Li and Y. Zhu, "Cramer–Rao Bound for Frequency Estimation of Spectral Interference and Its Shot Noise-Limited Behavior," IEEE Journal of Selected Topics in Quantum Electronics **23**, 2, 1-7 (2017).

[17] K. Creath, "Phase-measurement interferometry techniques, " Progress in Optics **26**, 349-393 (1988).

[18] J. C. Wyant, C. L. Koliopoulos, B. Bhushan, and O. E. George, "An optical profilometer for surface characterization of magnetic media, " ASLE Transactions **27**, 101-113 (1984).

[19] P. A. A. M. Junior, P. S. Neto, and C. S. Barcellos, "Generalization of Carré equation, " Optik-International Journal for Light and Electron Optics **122**, 475-489 (2011).

[20] K. Qian, F. Shu, and X. Wu, "Determination of the best phase step of the Carré algorithm in phase shifting interferometry, " Measurement Science and Technology **11**, 1220-1223 (2000).

[21] P. Hariharan, B. F. Oreb, and T. Eiju, "Digital phase-shifting interferometry: a simple error-compensating phase calculation algorithm," Applied Optics **26**, 2504-2506 (1987).

[22] J. H. Bruning, D. R. Herriott, J. E. Gallagher, D. P. Rosenfeld, A. D. White, and D. J. Brangaccio, "Digital Wavefront Measuring Interferometer for Testing Optical Surfaces and Lenses, " Applied Optics **13**, 2693-2703 (1974).

[23] E. Cuche, F. Bevilacqua, and C. Depeursinge, "Digital holography for quantitative phase-contrast imaging," Optics Letters **24**, 291-293 (1999).

[24] F. Röder, A. Lubk, D. Wolf, and T. Niermann, "Noise estimation for off-axis electron holography, " Ultramicroscopy **144**, 32-42 (2014).

[25] S. L. Chang, C. Dwyer, J. Barthel, C. B. Boothroyd, and R. E. Dunin-Borkowski, "Performance of a direct detection camera for off-axis electron holography," Ultramicroscopy **161**, 90-97 (2016).

[26] S. Chen, and Y. Zhu, "Phase sensitivity evaluation and its application to phase shifting interferometry," Methods, **136**, 50-59 (2018).

[27] S. Chen, C. Li, and Y. Zhu, "Sensitivity evaluation of quantitative phase imaging: a study of wavelength shifting interferometry," Optics Letters **42**, 1088-1091 (2017).

Chapter 5 Summary

In this work, a category of highly sensitive full-field imaging techniques that has the potential to easily access the commercialized microscope is proposed. Their sensitivity performance is also discussed under a complete framework. SS-DHPM combines swept source-based low coherence interferometry with on-axis, image-plane digital holography for QPI. It benefits from adjusting the CF to a frequency range free of interference artifacts, and from the excellent sweep repeatability of the source. The latter may be a benefit of the relatively slow yet perhaps better-controlled sweep that fits the full-field operation. This is in contrast to the more popular OCT swept source that offers high repetition rates in a point-scanning scheme. Additionally, access to spectral content allows for spectroscopic measurement by treating the signal as an information-modulated carrier wave. R.I. dispersion of ICG solution has been quantitatively measured. LC-WSI, on the other hand, adopts a different operation mode of a nearly identical system hardware. It requires fewer acquisitions, with each spans a relatively broader linewidth to achieve low coherence illumination. For the particular case of four-band imaging, we show that the phase can be extracted with a modified Carré algorithm. We describe signal demodulation in detail and discuss its implication on system implementation. Real-time imaging of live sperm cells at 62.5 Hz can be achieved and dynamic dry mass of sperm head is measured with a full-scale error of ± 2%, validating the technique's capability for high-sensitivity, high-speed quantitative phase imaging. The demodulation scheme for alternative sources, such as low cost SLDs and LEDs have been discussed, along with the adjustment in demodulation method. Furthermore, we investigate the possibility of implementing WSI with a common path configuration using numerical wave propagation method and rigorous signal modeling, in an attempt to convert existing qualitative phase contrast microscope to quantitative versions with minimal modification.

In the part of sensitivity evaluation, we propose a three-level, including Cramér-Rao bound (CRB), algorithmic sensitivity and experimental sensitivity. Comparing the first two determines the theoretical efficiency of an algorithm, whilst inspecting the gap between the latter two reveals system efficiency. As a supplemental but critical study, we apply this framework to WSI techniques we proposed. In shot noise-limited regime, CRB is derived and the performance of 4-step Carré algorithm is studied in simulations and experiments. Importantly, the proposed procedure allows the algorithmic sensitivity to be conveniently estimated from a single set of

measurement data, which serves as a basis for system efficiency evaluation. The approaches we used to evaluate sensitivity are also suitable to analyze other QPI techniques, including PSI and off-axis interferometry.